



TECHNISCHE UNIVERSITÄT MÜNCHEN  
Munich School of Engineering

Dissertation

Modeling the Ferroelectric and Pyroelectric  
Characteristics in Polycrystalline Doped Hafnium Dioxides

Christopher Benjamin Künneth





## Modeling the Ferroelectric and Pyroelectric Characteristics in Polycrystalline Doped Hafnium Dioxides

**Christopher Benjamin Künneth**

Vollständiger Abdruck der von der promotionsführenden Einrichtung Munich School of Engineering der Technischen Universität München zur Erlangung des akademischen Grades eines

**Doktors der Naturwissenschaften (Dr. rer. nat.)**

genehmigten Dissertation.

**Vorsitzender:**

Prof. Dr. Thomas Hamacher

**Prüfende der Dissertation:**

1. Prof. Dr. Karsten Reuter
2. Prof. Dr. Alfred Kersch,  
Hochschule München
3. Prof. Dr. Andreas Rüdiger,  
INRS-EMT, Université du Québec

Die Dissertation wurde am 07.06.2018 bei der Technischen Universität München eingereicht und durch die prom. Einr. Munich School of Engineering am 14.08.2018 angenommen.



# Abstract

The recent discovery of *ferroelectricity* in the materials system  $\text{Hf}_{1-x}\text{Zr}_x\text{O}_2$  renewed the interest in a material, which was believed to be well-understood. Ferroelectricity is an exciting and extraordinary materials characteristic, in which an intrinsic and remanent polarization can be reversed with an external electric field. If a material exhibits ferroelectricity, it is *pyro-* and *piezoelectric* at the same time. The industry has particular interest in such materials, as their applications range from sensors to energy harvesters and non-volatile memories. The late discovery of ferroelectricity in  $\text{Hf}_{1-x}\text{Zr}_x\text{O}_2$  can be traced to the fact that ferroelectricity only appears in  $\text{Hf}_{1-x}\text{Zr}_x\text{O}_2$  under certain circumstances. Ferroelectricity was first found in Si-doped  $\text{HfO}_2$  thin films of 10 nm thickness. Later, other dopants and the material system  $\text{Hf}_{1-x}\text{Zr}_x\text{O}_2$  were experimentally examined with the result that various combinations exhibit pyro- and ferroelectricity, but only under thin film conditions. The objectives of this publication-based dissertation were to investigate and elucidate these experimental findings and conditions with the help of computational methods. Furthermore, is it possible to manipulate and optimize the pyro- and ferroelectricity in  $\text{Hf}_{1-x}\text{Zr}_x\text{O}_2$ , and what are the optimization approaches? The crystal phases, which are involved in or suspected to be responsible for the pyro- and ferroelectricity, were predominantly investigated with density functional theory (DFT) computations. Afterward, the raw DFT data was contextualized and interpreted in classical models. In the first publication of this dissertation, a Gibbs energy model based on DFT and experimental results were developed. The model showed that interface energies influence the crystallographic phase formation significantly and can explain the experimental findings for the materials system  $\text{Hf}_{1-x}\text{Zr}_x\text{O}_2$ . In two following publications, the energetic and geometric influence of dopants in  $\text{HfO}_2$  were investigated to provide insights into the phase formation under doping and to disclose a possible optimization mechanism. In a fourth and cooperative publication, experimental measurements of the pyroelectric effect of silicon doped thin films were correlated with their grain radius distributions. It turned out that the silicon concentration and the grain radius distribution entail a great potential of optimization. *Summa summarum*, a Gibbs energy model using interface energies of the various crystal phases was proposed as an explanation of the pyro- and ferroelectricity in  $\text{Hf}_{1-x}\text{Zr}_x\text{O}_2$ . Moreover, the doping concentration and grain radius distribution were examined and suggested as potentials of optimization. Additionally, implications of industrial applications, like sensors, energy harvesters or non-volatile memories, were pointed out.



# Autorenreferat

*Ferroelektrizität* ist eine eminente phänomenologische Eigenschaft von Festkörpern bei der eine intrinsische Polarisierung eines Kristalles durch das Anlegen eines äußeren elektrischen Feldes zwischen remanenten Zuständen geschaltet werden kann. Ein Material welches ferroelektrisch ist, ist zugleich *pyro-* und *piezoelektrisch*. Bei experimentellen Messungen an dünnen  $\text{Hf}_{1-x}\text{Zr}_x\text{O}_2$  Schichten, die lange und intensiv wegen ihrer exzellenten linear dielektrischen Eigenschaften mit einer dielektrischen Konstante von etwa 20 bis 40 studiert wurden, wurde unerwartet ferroelektrisches Verhalten beobachtet. Dieser bedeutende Fund ermöglicht es der Industrie das für seine gute Complementary Metal Oxide Semiconductor (CMOS) Kompatibilität und auch bei geringen Dicken guten dielektrischen Eigenschaften bekannte Material als Ferro-, Pyro- oder Piezoelektrikum einzusetzen. Das nur in dünnen Schichten (einige 10 nm) ferroelektrische  $\text{Hf}_{1-x}\text{Zr}_x\text{O}_2$  stellt außerdem ein Komplement zum viel studierten Perowskiten dar, der nur in dickeren Filmen ferroelektrisch ist. Die späte Entdeckung des ferroelektrischen Verhaltens von  $\text{Hf}_{1-x}\text{Zr}_x\text{O}_2$  ist vor allem darauf zurückzuführen, dass dünne  $\text{Hf}_{1-x}\text{Zr}_x\text{O}_2$  Schichten nur unter speziellen Prozessbedingungen und teilweise nur durch Dotierung ferroelektrisch und pyroelektrisch werden. Die Fragestellungen dieser publikationsbasierenden (kumulativen) Dissertation leiten sich unmittelbar aus dem letzten Satz ab und lauten: Warum ist  $\text{Hf}_{1-x}\text{Zr}_x\text{O}_2$  nur in dünnen Schichten pyro- und ferroelektrisch? Wie kann das pyro- und ferroelektrische Verhalten manipuliert bzw. optimiert werden und welche Optimierungsansätze gibt es? Außerdem, welche Rolle spielen Dotanden und physikalische Einflussfaktoren? Als geeignete Methoden für die Untersuchungen von  $\text{Hf}_{1-x}\text{Zr}_x\text{O}_2$  mit und ohne Dotanden sowie unter verschiedenen Randbedingungen wie z.B. Materialdehnungen oder elektrischem Feld wurde in dieser Dissertation überwiegend die Dichtefunktionaltheorie (DFT) verwendet. Die Auswertungen und Kontextualisierungen der DFT Ergebnissen wurden anschließend in klassischen Modellen durchgeführt. In dieser Dissertation konnte gezeigt werden, dass durch die Grenzflächenenergien der Kristallphasen der gekörnten und kolumnar wachsenden  $\text{Hf}_{1-x}\text{Zr}_x\text{O}_2$  Schichten die Pyro- und Ferroelektrizität bzw. die dafür notwendige Stabilisierung der *p-o* Phase erklärt werden kann. Weiter wurde der energetische Einfluss von Dotierstoffen auf die Kristallphasenformierung, und die Bildungsenthalpien und der Einbau der Dotierstoffe in  $\text{Hf}_{1-x}\text{Zr}_x\text{O}_2$  untersucht. Es wurde außerdem gefunden, dass sich Silizium und Cer positiv auf die Ferroelektrizität auswirken. In einer kooperativen Arbeit mit Experimenten zur Pyroelektrizität in Silizium dotiertem  $\text{HfO}_2$  wurde zudem eine Korrelation zwischen Kornradienverteilung und pyroelektrischem Koeffizienten mit hohem Opti-

## *Autorenreferat*

mierungspotential gefunden. *Summa summarum* wurde als Erklärung der Pyro- und Ferroelektrizität in dünnen  $\text{Hf}_{1-x}\text{Zr}_x\text{O}_2$  Schichten mit und ohne Dotierung die Grenzflächenenergie vorgeschlagen. Überdies wurden Optimierungspotentiale aufgezeigt und Vorschläge unterbreitet wie die Pyro- und Ferroelektrizität verbessert und optimiert werden kann. Außerdem wurden stets Implikationen der industriellen Anwendung, wie der nichtflüchtige ferroelektrische Speicher, pyroelektrische Sensor oder Energieernter diskutiert.



# Contents

<b>Abstract</b>	<b>iii</b>
<b>Autorenreferat</b>	<b>v</b>
<b>Contents</b>	<b>vii</b>
<b>List of Figures</b>	<b>ix</b>
<b>List of Tables</b>	<b>xi</b>
<b>Acronyms</b>	<b>xiii</b>
<b>1 Introduction</b>	<b>1</b>
<b>2 Hf<sub>1-x</sub>Zr<sub>x</sub>O<sub>2</sub> thin films</b>	<b>3</b>
2.1 Crystal Phases . . . . .	5
2.2 Ferroelectricity & Pyroelectricity . . . . .	6
2.3 Surface & Interfaces . . . . .	9
2.4 Doping . . . . .	10
<b>3 Density Functional Theory</b>	<b>13</b>
3.1 Approach . . . . .	13
3.2 Limitations . . . . .	16
3.3 Thermodynamics . . . . .	17
<b>4 Publications</b>	<b>21</b>
4.1 Modeling Ferroelectric Film Properties and Size Effects from Tetrago- nal Interlayer . . . . .	21
4.1.1 Summary . . . . .	22
4.1.2 Contribution . . . . .	22
4.2 The impact of charge compensated and uncompensated strontium defects	24
4.2.1 Summary . . . . .	25
4.2.2 Contribution . . . . .	25
4.3 Impact of Four-Valent Doping on the Crystallographic Phase Formation	26
4.3.1 Summary . . . . .	27
4.3.2 Contribution . . . . .	28

*Contents*

4.4	Ferroelectric Phase Transitions in Nanoscale HfO <sub>2</sub> Films . . . . .	29
4.4.1	Summary . . . . .	30
4.4.2	Contribution . . . . .	30
<b>5</b>	<b>Summary &amp; Conclusion</b>	<b>31</b>
<b>6</b>	<b>Outlook</b>	<b>35</b>
	<b>Acknowledgments</b>	<b>37</b>
	<b>Bibliography</b>	<b>39</b>
	<b>Appendices</b>	<b>49</b>

# List of Figures

2.1	The experimental (Exp.) and computational (DFT) equilibrium phase diagram of $\text{HfO}_2$ . The density functional theory (DFT) data is from reference 21 and the experimental data from reference 27. . . . .	3
2.2	The conventional cell of the six important crystal phases of the $\text{Hf}_{1-x}\text{Zr}_x\text{O}_2$ materials system in energetic ascending order. The metal atoms (Hf or Zr) are shown in cyan and the O atoms are shown in red. The notation used as shorthand for the various phases is indicated, along with the corresponding space group and number. . . . .	6
2.3	Phenomenological groups in crystals along with the number of point groups. . . . .	7
2.4	The OLSEN cycle <sup>55</sup> is incorporated into a $\mathbf{P}(\mathbf{E})$ diagram for energy harvesting from the pyroelectric effect. For high temperatures (e.g. 5.6 f.u. % silicon doped $\text{HfO}_2$ at $\sim 300$ K), the material is ferroelectric, and for low temperatures (e.g. 5.6 f.u. % silicon doped $\text{HfO}_2 \sim 120$ K), the material is linear dielectric. The HED of the OLSEN cycle is highlighted in the color magenta (framed by $1 \rightarrow 2 \rightarrow 3 \rightarrow 4 \rightarrow 1 \dots$ ). . . . .	8
2.5	Minimum energy path of the polarization ( $\mathbf{P}$ ) switching in $\text{Hf}_{1-x}\text{Zr}_x\text{O}_2$ compounds. The metal atoms (Hf or Zr) are shown in cyan and the O atoms are shown in red. The major polarization change ( $\Delta\mathbf{P}$ ) during the polarization switching is induced by the dark red atoms, while the bright red atoms hardly change their positions. . . . .	10
2.6	Schematic representation of the polycrystalline thin film. The grains have different radii and are grown columnar. . . . .	11
3.1	Schematic representation of the solution process of the electronic structure (Kohn-Sham (K.S.) equations) and of the ionic structure in DFT. . . . .	15

*List of Figures*

- 3.2 (a) Comparison of the total energy differences with respect to the  $m$ -phase from the local-density approximation (LDA) and generalized gradient approximation (GGA) exchange-correlation (XC) functionals, (b) correlation of the total energy differences with the volumes and (c) comparison of the total energy differences with and without the vibrational entropy contribution at 300 K. The calculations were consistently performed using the DFT code Abinit<sup>78,79</sup> with the PAW pseudo-potentials from the GBRV<sup>86</sup> library for HfO<sub>2</sub>. The vibrational entropy contribution of the  $c$ -phase is set to zero since it is a naturally unstable phase<sup>100</sup>. 18

# List of Tables

2.1	The crystal system, international (HERMANN-MAUGUIN) symbol, international space group number and a shorthand version of the crystal phases used in the text in the materials system $\text{Hf}_{1-x}\text{Zr}_x\text{O}_2$ . The phases are ordered in ascending order of the total energies from DFT. . . . .	4
-----	--	---



# Acronyms

ALD	atomic layer deposition
CMOS	complementary metal-oxide-semiconductor
CSD	chemical solution deposition
DFPT	density functional perturbation theory
DFT	density functional theory
FeRam	ferroelectric random access memory
GGA	generalized gradient approximation
GTO	GAUSSIAN-type orbital
HAADF-STEM	high-angle annular dark-field scanning transmission electron microscopy
HED	harvestable energy density
K.S.	KOHN-SHAM
LDA	local-density approximation
MD	molecular dynamic
MEP	minimum energy path
PBC	periodic boundary condition
PLD	pulsed laser deposition
SEM	scanning electron microscopy
XC	exchange-correlation
XRD	X-ray diffraction





# 1 Introduction

In 2011, Böske et al.<sup>11</sup> unveiled that experimental observations of silicon doped HfO<sub>2</sub> thin films of 10 nm thickness are *ferroelectric*. Shortly after, Müller et al.<sup>12</sup> published electrically measured  $\mathbf{P}(\mathbf{E})$  curves of thin Hf<sub>1-x</sub>Zr<sub>x</sub>O<sub>2</sub> films in the concentration range of  $0 \leq x \leq 1$  with the result that pure HfO<sub>2</sub> is linear dielectric, Hf<sub>0.5</sub>Zr<sub>0.5</sub>O<sub>2</sub> is ferroelectric and the hysteresis of pure ZrO<sub>2</sub> is antiferroelectric-like shaped. This led to many following experimental studies that investigated diverse dopants in the materials system Hf<sub>1-x</sub>Zr<sub>x</sub>O<sub>2</sub> and found that some dopants promote and some diminish the ability of Hf<sub>1-x</sub>Zr<sub>x</sub>O<sub>2</sub> to exhibit ferroelectricity<sup>4,13,14</sup>. Ferroelectricity means that a material has a spontaneous, intrinsic polarization, which can be reversed with an external electric field<sup>15</sup>. Although the materials system Hf<sub>1-x</sub>Zr<sub>x</sub>O<sub>2</sub> was studied for years for use in the semiconductor industry as a linear dielectric material with a high dielectric constant (high-k) of around 30 to 40<sup>16-18</sup>, the ferroelectric characteristics was first discovered in 2011. Interestingly, ferroelectric materials are *pyroelectric* and *piezoelectric* at the same time<sup>15</sup>, which thus opens a variety of fields of application for the material ranging from the use as a non-volatile memory to sensor and energy harvesting applications. From the crystallographic perspective, pyroelectricity can only emerge in crystals with a polar space-group symmetry (polar phase), i.e. the symmetry allows the existence of a permanent dipole<sup>19</sup>. If the dipole can be reversed by an electric field, the crystal phase is additionally called ferroelectric. In the materials system Hf<sub>1-x</sub>Zr<sub>x</sub>O<sub>2</sub>, experimental and computational observations indicate the *p-o*-phase (polar orthorhombic phase) to be responsible for the ferroelectricity<sup>3,20,21</sup>.

The crystal phase stability of bulk Hf<sub>1-x</sub>Zr<sub>x</sub>O<sub>2</sub> is extensively studied experimentally under several ambient conditions without identifying polar phases with the ability to exhibit ferroelectricity and pyroelectricity<sup>22-25</sup>. In addition, these experimentally observed bulk phases are computationally confirmed with density functional theory (DFT) computations (c.f. with the pressure against volume  $P(V)$  diagram in figure 2.1 for HfO<sub>2</sub>). However, experimental measurements of different thicknesses of Hf<sub>1-x</sub>Zr<sub>x</sub>O<sub>2</sub> thin films evidence a ferroelectric hysteresis. Furthermore, the measurements indicate that the ferroelectricity is thickness dependent and disappears in thicker films. This observation is called the *size effect* and is complementary to the heavily explored ferroelectric perovskites, which are ferroelectric in thicker films but often lose their electric characteristics under thin film conditions (usual dimension of thin films in the growth directions are in the order of magnitude of 10 nm). Moreover, the size effect in Hf<sub>1-x</sub>Zr<sub>x</sub>O<sub>2</sub> strongly indicates that the film thickness is an important factor for the appearance and stabilization of the *p-o*-phase and thus the ferroelectricity in

## 1 Introduction

$\text{Hf}_{1-x}\text{Zr}_x\text{O}_2$ . Another observation relating to the size effect is that  $\text{Hf}_{1-x}\text{Zr}_x\text{O}_2$  thin films are columnar grown and polycrystalline with grain radii in the range of 5 nm to 40 nm, which vary with the film thickness. A physical concept, which may explain such a size effect and depends on the surface area, is the *surface* or *interface energy*.

Apart from the interface energy, other factors have been conjectured to be responsible for the emergence of the *p-o*-phase. Ferroelectric  $\text{Hf}_{1-x}\text{Zr}_x\text{O}_2$  thin films are normally grown on substrates with different lattice constants, which may expose high strains on the  $\text{Hf}_{1-x}\text{Zr}_x\text{O}_2$  films. Starting in the order of 1 %, this strain influences the phase stability in the  $\text{Hf}_{1-x}\text{Zr}_x\text{O}_2$  thin films, which may stabilize the *p-o*-phase<sup>10,26</sup>. However, such high strains could not be experimentally confirmed so far. In addition, for the flip of the remanent polarization, the  $\text{Hf}_{1-x}\text{Zr}_x\text{O}_2$  thin films are exposed to high electric fields in the order of  $1 \text{ MVcm}^{-1}$ , which are close to the breakthrough electric field. In principle, such high applied electric fields favor the *p-o*-phase but do not explain why ferroelectricity is also observed in the absence of the electric field.

The crystal symmetry and the atomic species (also referred to as the basis) are causal for the ferro- and pyroelectricity (and piezoelectricity) in crystals. Therefore, the pyroelectricity is strongly correlated with the ferroelectricity and a concerted investigation is recommended. The main objective in this dissertation was to investigate the ferroelectricity and pyroelectricity in  $\text{Hf}_{1-x}\text{Zr}_x\text{O}_2$  with computational methods. The aim was to understand the formation of the crystal phases and especially the *p-o*-phase relating to the possible physical and chemical factors for an optimization of both materials characteristics and an adaption to possible devices. The physical factors are briefly mentioned in the previous two paragraphs and detailed in [sections 2.3](#) and [3.3](#). Aside from these physical factors, doping provides an important factor and a potential of optimization in  $\text{Hf}_{1-x}\text{Zr}_x\text{O}_2$ , which is discussed in [section 2.4](#). Most of the results in this dissertation were generated on the atomistic level by using DFT and transferred to thermodynamics in classical models, such as a Gibbs energy model.

This dissertation is based on four publications (references 1–4). In the first publication, a Gibbs energy model, which includes interface energies and entropies of the dissimilar crystal phases, was explored and exploited for the materials system  $\text{Hf}_{1-x}\text{Zr}_x\text{O}_2$  with the result that one set of interface energies for the phases suffices to explain the appearance of the ferroelectric *p-o*-phase in  $\text{Hf}_{1-x}\text{Zr}_x\text{O}_2$ <sup>1</sup>. After investigating and elucidating a possible main cause of the ferroelectricity in  $\text{Hf}_{1-x}\text{Zr}_x\text{O}_2$ , the influence of the incorporation of dopants on the phase stability was delved to explore its potential of optimization. At first, the charge compensation mechanism with a significant influence on the energies was studied for the example of Sr in  $\text{HfO}_2$ <sup>2</sup>. Subsequently, the incorporation of seven other dopants (Si, Ge, Ti, Zr, Sn, Zr and Ce) in  $\text{HfO}_2$  is extensively investigated, including the influence on the crystal phase formation, the formation energies and the geometrical incorporation of the dopant in  $\text{HfO}_2$ <sup>3</sup>. In a fourth publication, the pyroelectricity of silicon doped  $\text{HfO}_2$  is addressed with experimental measurements and a detailed theoretical interpretation<sup>4</sup>.

## 2 $\text{Hf}_{1-x}\text{Zr}_x\text{O}_2$ thin films

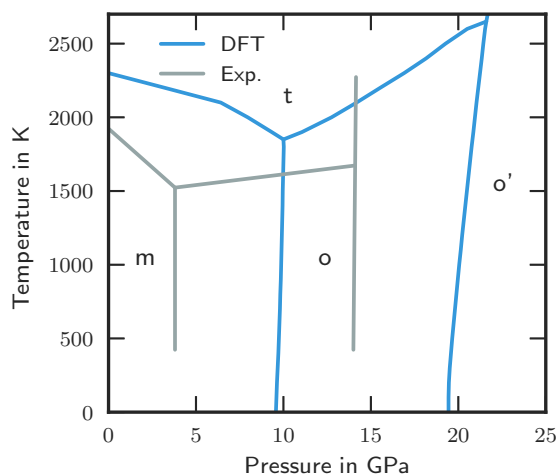


**Figure 2.1:** The experimental (Exp.) and computational (DFT) equilibrium phase diagram of  $\text{HfO}_2$ . The DFT data is from reference 21 and the experimental data from reference 27.

The elements hafnium (Hf) and zirconium (Zr) are both transition metals and have 72 and 40 electrons, respectively. Their oxides, hafnium dioxide ( $\text{HfO}_2$ ) and zirconium dioxide ( $\text{ZrO}_2$ ), share the same crystallographic phases and are experimentally completely miscible (solid solution) in the materials system  $\text{Hf}_{1-x}\text{Zr}_x\text{O}_2$  ( $0 \leq x \leq 1$ )<sup>28</sup>. Moreover, the formation energy for the exchange of one Hf in  $\text{HfO}_2$  with Zr is less than 0.5 eV and *vice versa*, which is small in comparison to other dopants<sup>3</sup>. Pure  $\text{HfO}_2$  and  $\text{ZrO}_2$  thin films are well-known for their full complementary metal-oxide-semiconductor (CMOS) integrability and are attractive for the semiconductor industry because of their high dielectric constants (high-k dielectric materials) between 20 and 40 (depending on the crystal phase)<sup>18</sup>.

In 2011, experimental measurements of Börscke et al.<sup>11</sup> revealed that atomic layer deposition (ALD) manufactured silicon doped  $\text{HfO}_2$  thin films with a thickness of 10 nm are *ferroelectric*. This observation was unexpected and opened a new research area for a material which was extensively studied for years and believed to be well examined. Only a little later, Müller et al.<sup>12</sup> investigated thin  $\text{Hf}_{1-x}\text{Zr}_x\text{O}_2$  films experimentally

Crystal system	International symbol (point group)	International space group no.	Abbreviation
Monoclinic	$P2_1/c$ ( $2/m$ )	14	<i>m</i> -phase
Orthorhombic	$Pbca$ ( $mmm$ )	61	<i>o</i> -phase
Orthorhombic (polar)	$Pca2_1$ ( $mm2$ )	29	<i>p-o</i> -phase
Orthorhombic (polar)	$Pmn2_1$ ( $mm2$ )	31	<i>p-o'</i> -phase
Tetragonal	$P4_2/nmc$ ( $4/mmm$ )	137	<i>t</i> -phase
Orthorhombic	$Pnma$ ( $mmm$ )	62	<i>o'</i> -phase
Cubic	$Fm\bar{3}m$ ( $m\bar{3}m$ )	225	<i>c</i> -phase

**Table 2.1:** The crystal system, international (HERMANN-MAUGUIN) symbol, international space group number and a shorthand version of the crystal phases used in the text in the materials system  $\text{Hf}_{1-x}\text{Zr}_x\text{O}_2$ . The phases are ordered in ascending order of the total energies from DFT.

with the result that pure  $\text{HfO}_2$  is linear dielectric,  $\text{Hf}_{0.5}\text{Zr}_{0.5}\text{O}_2$  is ferroelectric and the hysteresis of pure  $\text{ZrO}_2$  is anti-ferroelectric shaped. Later, many other experimental studies from diverse groups were carried out and found ferroelectricity in  $\text{Hf}_{1-x}\text{Zr}_x\text{O}_2$  or doped  $\text{Hf}_{1-x}\text{Zr}_x\text{O}_2$  thin films manufactured with different deposition techniques as ALD<sup>29,30</sup>, chemical solution deposition (CSD)<sup>14,31–33</sup>, sputtering<sup>34</sup> or pulsed laser deposition (PLD)<sup>35,36</sup>.

Figure 2.1 compares the bulk equilibrium phase diagram between experimental measurements<sup>27</sup> and DFT computations<sup>21</sup>. The temperatures and pressures when the phase transformation appears in figure 2.1 agree well qualitatively, but disagree in the exact value. The reasons for this quantitatively disagreement are diverse and may be caused by the chosen pseudopotentials or the exchange-correlation (XC) functional used in the DFT calculations (see section 3.1). However, this overall good agreement between the computed and measured phase diagram of temperature and pressure can be seen as a legitimation of the use of DFT calculations to investigate phase stability of  $\text{HfO}_2$ .

According to figure 2.1, only non-polar crystal phases can be stabilized in the *bulk* phase diagram for different applied temperatures and pressures. However, ferroelectric and pyroelectric characteristics require a polar crystal phase present in the material. As a consequence, the influence of temperature, pressure, or their combination does not induce the stabilization of a polar crystal phase like the *p-o*-phase (see below) in  $\text{HfO}_2$ . On the other hand, this means that other effects, such as strain, electric field, interface energy or their combinations, must be present to explain the ferroelectricity and pyroelectricity in  $\text{HfO}_2$ . The same arguments and discussion apply, *mutatis mutandis*, to  $\text{ZrO}_2$ . A general formulation and discussion of the Gibbs energy for the materials system  $\text{Hf}_{1-x}\text{Zr}_x\text{O}_2$  with all the contributions can be found in section 3.3.

## 2.1 Crystal Phases

The necessary condition for a material to show ferroelectricity is that the symmetry of crystallographic phase is polar. The crystallographic phase that is experimentally believed to be responsible for the ferroelectricity in  $\text{Hf}_{1-x}\text{Zr}_x\text{O}_2$ <sup>11,20</sup> and is energetically the lowest polar phase (*p-o*-phase)<sup>1,10,21</sup> has the international (HERMANN-MAUGUIN) symbol  $Pca2_1$  with the space group no. 29. Aside from the *p-o*-phase, several other crystal phases were proposed based on group theoretic reduction and computations<sup>21,37</sup> or are experimentally identified with X-ray diffraction (XRD) and high-angle annular dark-field scanning transmission electron microscopy (HAADF-STEM)<sup>20</sup>. The ground state of the binary oxide  $\text{HfO}_2$  under ambient conditions ( $\sim 298$  K and 0.1 GPa) is a monoclinic phase (*m*-phase) with the space group no. 14 and the international symbol  $P2_1/c$ . At a pressure of  $\sim 4$  GPa, the *m*-phase transforms into an orthorhombic phase (*o*-phase) with the number 61 and the symbol  $Pbca$ . By reaching  $\sim 15$  GPa, the *o*-phase transforms to a second orthorhombic phase (*o'*-phase) with the number 62 and symbol  $Pnma$ . By increasing the temperature, at  $\sim 2000$  K, the *m*-phase transforms to a tetragonal phase (*t*-phase) with the number 137 and the symbol  $P4_2/nmc$ . Increasing the temperature further, at  $\sim 2800$  K, the *t*-phase transforms into a cubic phase (*c*-phase) with the number 225 and the symbol  $Fm\bar{3}m$ . A further interesting phase is the polar, orthorhombic phase (*p-o'*-phase) with the symbol  $Pmn2_1$  and the number 31, which is energetically engought close to the *m*-phase to be considered. The temperature and pressure transformation values are for pure  $\text{HfO}_2$  and taken from reference<sup>27</sup>. In  $\text{ZrO}_2$ , the temperature and pressure transformation values are slightly shifted to lower values<sup>28,38</sup>. The phases are illustrated in figure 2.2 and tabulated in table 2.1, along with their shorthands used throughout this dissertation and space groups.

It is experimentally found that  $\text{Hf}_{1-x}\text{Zr}_x\text{O}_2$  films are polycrystalline with grains of dissimilar radius. The grain radii are in the range of about 5 nm to 40 nm and can be captured in a grain radius distribution<sup>4,39,40</sup>. Moreover, experimental investigations indicate that the grains are columnar grown from the bottom to the top electrode (thin film thickness  $\approx$  grain height) and that different phases can coexist in one grain with a possible pinned *t*-phase interlayer towards the electrodes<sup>41-44</sup>. It is experimentally and computationally conjectured that the grains (or more generally the grain radius distribution) of the films modify the ferroelectric or pyroelectric characteristics of the thin films significantly and can be used to optimize the figure of merits<sup>39,41</sup>. Another observation from the experiment is that the grain radii scale with the film thickness and that this scaling or change of the grain radii depends on the used deposition technique. Park et al.<sup>45</sup> found that the grain radii increase with increasing Zr content in  $\text{Hf}_{1-x}\text{Zr}_x\text{O}_2$ .

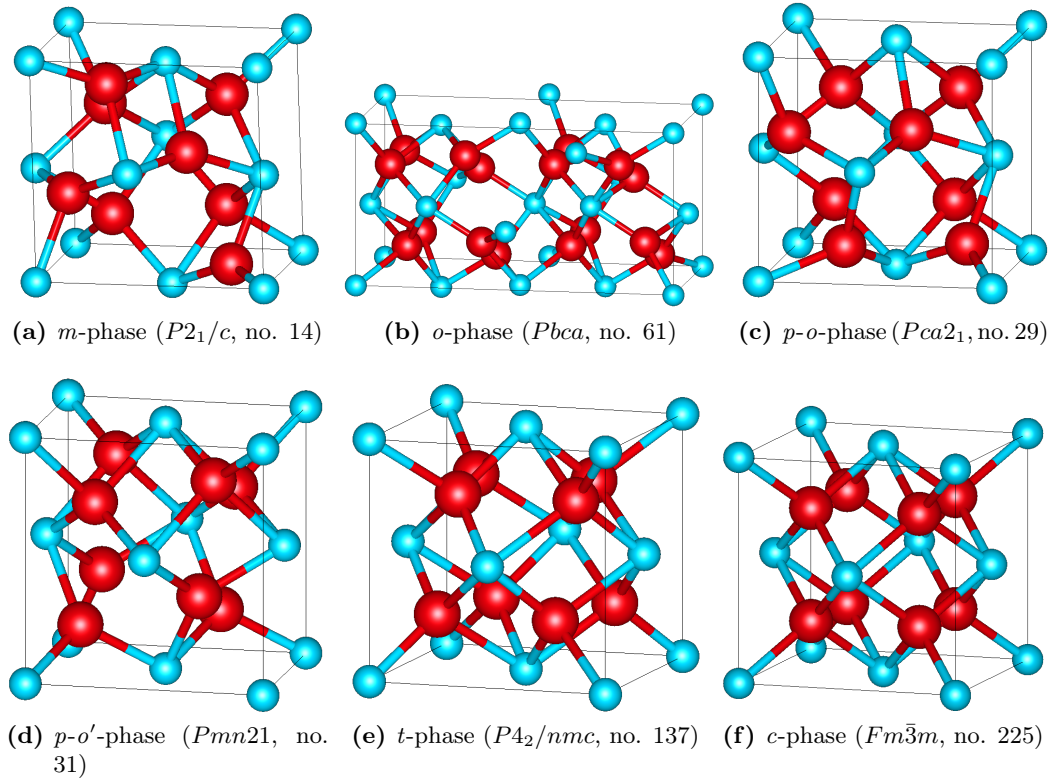


**Figure 2.2:** The conventional cell of the six important crystal phases of the  $\text{Hf}_{1-x}\text{Zr}_x\text{O}_2$  materials system in energetic ascending order. The metal atoms (Hf or Zr) are shown in cyan and the O atoms are shown in red. The notation used as shorthand for the various phases is indicated, along with the corresponding space group and number.

## 2.2 Ferroelectricity & Pyroelectricity

Ferroelectricity is a very intricate characteristics of a material since it brings pyroelectricity and piezoelectricity at the same time (c.f. figure 2.3). Pyroelectricity means that a material changes its polarization ( $\mathbf{P}$ ) with its temperature ( $d\mathbf{P}/dT \neq 0$ ) and piezoelectricity that a material changes its polarization when strain ( $\epsilon$ ) is applied ( $d\mathbf{P}/d\epsilon \neq 0$ ). Both phenomenological characteristics of a material have an inverse effect, which operates *vice versa*. A material can only show ferroelectricity and pyroelectricity if its crystallographic phase is polar, i.e. the summation of all dipoles in the material (polarization) is unequal to zero, even in the absence of an electric field. While for pyroelectricity the condition of a polar crystal phase is sufficient, a material is additionally ferroelectric if the remanent (or retentive) polarization ( $\mathbf{P}_r$ ) can be reversed with an external electric field. The intrinsic reason of the change in the polarization may be a displacive phase transition between two equilibrium positions, which alters dipoles in the crystal and thus moves the centers of charge. If

the ferroelectric material is sandwiched between electrodes (e.g. in a capacitor), the change in the intrinsic polarization by an external electric field can be compensated by charges (electrons or holes) at the electrodes. This compensation at the electrodes generates an electric current  $I$ , which is usually measured jointly with the applied electric field  $\mathbf{E}$ . Finally, the measurements of a ferroelectric material displays a  $\mathbf{P}(\mathbf{E})$  hysteresis curve as exemplified in figure 2.4. The polarization states “up” and “down” of the two stable equilibrium positions can be utilized to store binary information (“0” and “1”) in the polarization of the ferroelectric material, which is used in the semiconductor industry for non-volatile memory components, e.g. as ferroelectric random access memories (FeRAMs)<sup>5,6,46</sup>. Figure 2.5 exemplifies the minimum energy path (MEP) of the polarization switching in the materials system  $\text{Hf}_{1-x}\text{Zr}_x\text{O}_2$ <sup>8,21,47</sup>.

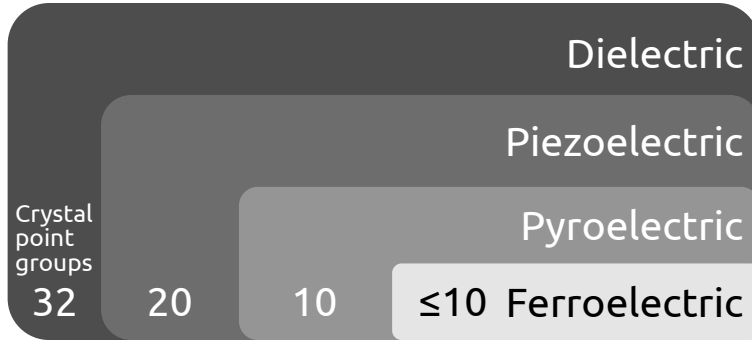


**Figure 2.3:** Phenomenological groups in crystals along with the number of point groups.

A material with a non-centrosymmetric crystal phase can show *piezoelectricity*, and with a polar and non-centrosymmetric crystal phase *piezoelectricity* and *pyroelectricity*. In addition, if the polarization can be reversed between two states by an external electric field, the material is *ferroelectric*. A more abstract definition is that all ferroelectric crystals are pyroelectric, and pyroelectricity is a subset of piezoelectricity. This definition is based on NEUMANN’s symmetry principle (c.f. figure 2.3), which links the symmetry with the physical characteristics of a crystal.

In the materials system  $\text{Hf}_{1-x}\text{Zr}_x\text{O}_2$ , two crystallographic phases are theoretically identified with the ability to show ferroelectricity and pyroelectricity: (i) the orthorhombic  $Pca2_1$  ( $p$ - $o$ -phase) and (ii) the orthorhombic  $Pmn2_1$  ( $p$ - $o'$ -phase)<sup>10,21</sup>. In several experimental studies for  $\text{Hf}_{1-x}\text{Zr}_x\text{O}_2$ , the  $p$ - $o$ -phase was strongly conjectured as the source of the ferroelectricity<sup>11,13,20,48</sup>. From DFT computations, the  $p$ - $o$ -phase is closer to the minimum energy  $m$ -phase than the  $p$ - $o'$ -phase, which makes the  $p$ - $o$ -phase more likely to be responsible for the ferroelectricity<sup>3,10,21</sup>. It should be noted that doping and physical effects in  $\text{Hf}_{1-x}\text{Zr}_x\text{O}_2$  significantly influences the energy of the various phases and may change the aforementioned energy order of the polar, orthorhombic phases.

Ferroelectricity is usually measured by applying an electric field in sawtooth cycles to the material and recording the response electric current using electrodes<sup>49,50</sup>. Two important metrics to classify the emerging hysteresis loops from a ferroelectric

material are the remanent polarization ( $\mathbf{P}_r$ ) and the coercive electric field ( $\mathbf{E}_c$ ). The remanent polarization is the polarization at zero electric field, and by reaching the coercive field, the polarization is reversed. For the quantification of the pyroelectricity, the pyroelectric coefficient ( $\mathbf{p} = d\mathbf{P}/dT$ ) may be used as a figure of merit. The pyroelectric coefficient can be measured for (i) the dynamic case, in which the pyroelectric coefficient is calculated from the change of the remanent polarization with the temperature while cycling with the electric field, and (ii) the static case, in which the change of the remanent polarization with temperature is measured without applying an electric field. In both cases, the pyroelectric coefficients in  $\text{Hf}_{1-x}\text{Zr}_x\text{O}_2$  were found to be large in comparison to other pyroelectric materials<sup>4,13,51–54</sup>.

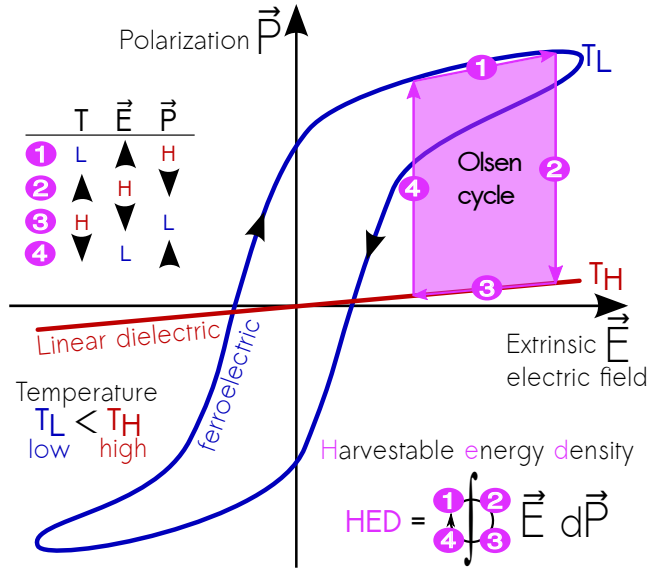


**Figure 2.4:** The OLSEN cycle<sup>55</sup> is incorporated into a  $\mathbf{P}(\mathbf{E})$  diagram for energy harvesting from the pyroelectric effect. For high temperatures (e.g. 5.6 f.u. % silicon doped  $\text{HfO}_2$  at  $\sim 300$  K), the material is ferroelectric, and for low temperatures (e.g. 5.6 f.u. % silicon doped  $\text{HfO}_2$   $\sim 120$  K), the material is linear dielectric. The HED of the OLSEN cycle is highlighted in the color magenta (framed by 1  $\rightarrow$  2  $\rightarrow$  3  $\rightarrow$  4  $\rightarrow$  1...).

Figure 2.4 schematically shows a  $\mathbf{P}(\mathbf{E})$  hysteresis curve from the measurement of a ferroelectric crystal (blue) and a linear dielectric behavior of a non-ferroelectric crystal (red). The ferroelectric characteristics of a material can be changed from ferroelectric to linear dielectric by increasing the temperature. The temperature when the ferroelectric characteristic completely disappears is named the CURIE temperature ( $T_c$ ). The curves of figure 2.4 are superimposed with the schematic representation of the OLSEN cycle<sup>55</sup>, which is a thermodynamic cycle for using the pyroelectric effect for energy conversion from heat to electric energy. It should be noted that the ferroelectricity slowly transforms into linear dielectricity while increasing the temperature, and the OLSEN cycle can also go through the intermediate states. The materials systems



$\text{Hf}_{1-x}\text{Zr}_x\text{O}_2$ , Si-doped  $\text{HfO}_2$ <sup>4</sup> and  $\text{Hf}_{0.2}\text{Zr}_{0.8}\text{O}_2$ <sup>52,53</sup> are found to exhibit a very high harvestable energy density (HED), which is the figure of merit for energy harvesting. The conversion effect of electric to heat energy is named electrocaloric effect (inverse pyroelectric effect) and was also investigated for  $\text{Hf}_{1-x}\text{Zr}_x\text{O}_2$ <sup>4,53,56</sup>.

## 2.3 Surface & Interfaces

One of the research objectives of this dissertation was to investigate the influences and effects of the surfaces and interfaces, which are natively present in polycrystalline  $\text{Hf}_{1-x}\text{Zr}_x\text{O}_2$  thin films<sup>5,39</sup>. The typical dimensions of a thin film are  $D \times W \times T$  ( $D$  the depth,  $W$  the width and  $T$  the thickness) with  $T \ll W, D$ . It is experimentally found that the ferroelectricity varies with the film thickness and disappears for a certain thickness, whereas the upper bound of thickness depends on the Zr concentration  $x$  in  $\text{Hf}_{1-x}\text{Zr}_x\text{O}_2$ , doping species and the manufacturing process of the film<sup>1,7,41,57–60</sup>. Aside from the confinement of the crystal in one direction (out-plane, towards  $T$ ) by the film thickness, the other two directions (in-plane, towards  $D, W$ ) are confined by the grain boundaries with measured grain radii in the range of 5 nm to 40 nm<sup>4,45</sup>. A schematic illustration for such a grained thin film is shown in [figure 2.6](#).

The aforementioned geometrical confinement of the spatial extensions inevitably leads to the presence of surfaces and interfaces in thin  $\text{Hf}_{1-x}\text{Zr}_x\text{O}_2$  films. The creation or destruction of surfaces or interfaces with the area  $\mathcal{A}$  in a material requires or returns an energy  $dU$ . If the area is created between a material and vacuum (usually including air), the energy is called surface energy. On the other hand, the energy necessary to create an interface between two solid materials or different crystal phases of one material is called interface or interphase energy, respectively. It is expected that the coherence of the interface of adjacent phases (domain wall) is high and the value of the interphase energy low. Contrary, grain boundaries are expected to have a worse coherence of the interface with a higher interface energy. In general, the surface and interface energy can be defined as  $\gamma = dU/d\mathcal{A}$ . A typical order of magnitude for the surface energy (between a material and vacuum) is  $1 \text{ J m}^{-2}$  and for the interface energy (between two crystal phases or grain boundaries) is  $10^{-1} \text{ J m}^{-2}$  to  $10^{-2} \text{ J m}^{-2}$  in  $\text{Hf}_{1-x}\text{Zr}_x\text{O}_2$ <sup>1,10,61,62</sup>. The exact values differ for the various crystal phases of  $\text{Hf}_{1-x}\text{Zr}_x\text{O}_2$  and depend additionally on the orientation of the crystal surface<sup>61,63–65</sup>.

The calculation of surface energies with DFT is a non-trivial undertaking. A typical DFT computation of the surface energy uses a supercell approach, in which vacuum is introduced in one direction of a multiple of a unit cell. The vacuum area artificially breaks the periodicity of the supercell in one direction and creates two surfaces (surface slab). Depending on the symmetry of the crystal, various surfaces ( $(100)$ ,  $(110)$ ,  $(210)$ ,  $\dots$ ) must be considered and computed. Since we want to calculate the surface energy, the bulk energy needs to be subtracted after we computed the total energy of the slabs. This requires the surfaces of the slabs to be stoichiometric and symmetric. In the case of  $\text{Hf}_{1-x}\text{Zr}_x\text{O}_2$ , only surface slabs of the  $c$ - and  $t$ -phase can be built that comply with both requirements. The calculation of interface energies between two

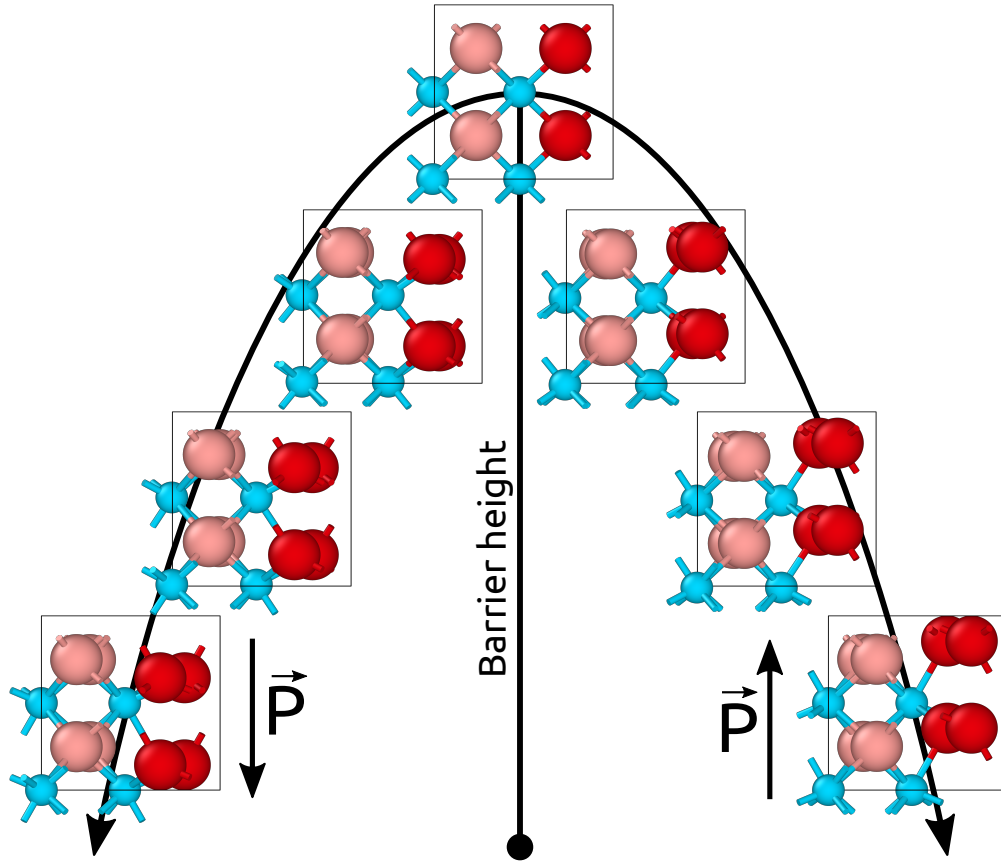


**Figure 2.5:** Minimum energy path of the polarization ( $\mathbf{P}$ ) switching in  $\text{Hf}_{1-x}\text{Zr}_x\text{O}_2$  compounds. The metal atoms (Hf or Zr) are shown in cyan and the O atoms are shown in red. The major polarization change ( $\Delta\mathbf{P}$ ) during the polarization switching is induced by the dark red atoms, while the bright red atoms hardly change their positions.

crystal phases of  $\text{Hf}_{1-x}\text{Zr}_x\text{O}_2$  is an even more tricky task since first, the same issues appear as for the surface energies and second, the supercells contain two different crystal phases which are connected with an interface. Experimentally, surface or interface energies are difficult to measure and results are only rarely available with partly significantly different values. In this dissertation, the values for the interface energies are fit parameters from a Gibbs energy model, which is described in reference 1.

## 2.4 Doping

As ferroelectricity was first measured in Si-doped  $\text{HfO}_2$  by Börske et al.<sup>11</sup>, in many following studies, the influence of various other dopants on the ferroelectricity and pyroelectricity in  $\text{Hf}_{1-x}\text{Zr}_x\text{O}_2$  was investigated experimentally<sup>4,13,14,29,31,66–70</sup> and com-

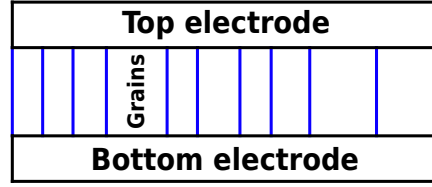


**Figure 2.6:** Schematic representation of the polycrystalline thin film. The grains have different radii and are grown columnar.

putationally<sup>2,3,9,71,72</sup>. Although several dopants were found to influence the phase stability in  $\text{Hf}_{1-x}\text{Zr}_x\text{O}_2$ , silicon is still one of the high-impact dopants relating to the energetic influence on the crystal phases and their associated materials characteristic. Especially in pure  $\text{HfO}_2$  thin films, the *p-o*- and, even more, the *t*-phase are preferred with increasing silicon doping concentration. Silicon doped  $\text{HfO}_2$  thin films with a concentration of 3.1 f.u. % have a ferroelectric behavior, while a doping concentration of 5.6 f.u. % is already sufficient to stabilize the *t*-phase over the other phases and thus makes  $\text{HfO}_2$  linear dielectric.

Similar impacts on the energy of the phases can be observed for other dopants, but with a different phase preference at different concentration values. For instance, for Sr-doped  $\text{HfO}_2$ , the observed ferroelectric window ranges from 3.4 f.u. % to 7.9 f.u. %<sup>29</sup>. In the broadest sense, Zr can also be considered as a dopant but with a possible dopant concentration up to 100 % (pure  $\text{ZrO}_2$ ). Zr doping changes the electric properties of  $\text{HfO}_2$  thin films with increasing dopant concentration from linear dielectric for pure  $\text{HfO}_2$  over ferroelectric for  $\text{Hf}_{0.5}\text{Zr}_{0.5}\text{O}_2$  to anti-ferroelectric shaped for pure  $\text{ZrO}_2$ . In addition to single-species doping, mixed-species doping in  $\text{HfO}_2$  was experimentally investigated. Lomenzo et al.<sup>66</sup> found evidence that the ferroelectric characteristics for mixed doping of  $\text{HfO}_2$  with Al and Si depend on the deposition order of the atoms in the ALD process. Furthermore, they showed that the deposited Al or Si do not distribute uniformly in the growth direction of the film but rather create a thin film with layers of dopants (laminates).

Depending on the valence and species of a dopant, the incorporation of a dopant in the host  $\text{Hf}_{1-x}\text{Zr}_x\text{O}_2$  crystal requires a charge compensation mechanism. If the dopant is isovalent to  $\text{HfO}_2$  or  $\text{ZrO}_2$  (i.e. Si, Ge, Ti, etc.), no excess charge (electron or hole) which is localized at the dopant is formally created by the incorporation and no compensation is necessary. For all aliovalent dopants (i.e. Al, Mg, Y, etc.), the incorporation creates excess charges, which must be compensated. Typically, two mechanisms to compensate charges are possible in insulators: (i) the charge is compensated *ionically*, i.e. by oxygen vacancies, or (ii) the charge is compensated *electronically* by electrons or holes, which are located at the surfaces. In addition, for trivalent dopants in  $\text{Hf}_{1-x}\text{Zr}_x\text{O}_2$ , a *mixed* charge compensation mechanism based on (i) and (ii) is possible. The ionic charge compensation with oxygen vacancies, including the interaction with the electrodes, is experimentally conjectured to influence

## 2 $\text{Hf}_{1-x}\text{Zr}_x\text{O}_2$ thin films

the ferroelectricity in  $\text{Hf}_{1-x}\text{Zr}_x\text{O}_2$  and cause the “wake-up” , i.e. the change of the hysteresis shape in the first thousands of electric field cycles, of such materials<sup>73–77</sup>.

The computation of materials characteristics of doped crystals is usually performed in supercells to obtain the desired doping concentration. Supercells are multiples of the unit cell, and to achieve a doping concentration of e.g. 6.25 f.u. % (formula unit, f.u. =  $n/3$  with  $n$  the number of atoms), a possible supercell has 48 atoms (1 dopant, 15 Hf, and 32 O). Depending on the compensation mechanism of the dopant (see above), oxygen vacancies may be incorporated additionally in a specific concentration. Accordingly, computations of doped structures of  $\text{Hf}_{1-x}\text{Zr}_x\text{O}_2$  often involve 48 or 96 atoms, which make the calculations time-consuming.

# 3 Density Functional Theory

Density functional theory (DFT) has its origin in the 1960's and has since evolved as the preferred tool for the first-principles computational investigation of crystals and molecules on the atomistic length scale. The main reason for this is the smart decomposition of the many-body (many-electron) problem into many single-body problems and the use of the HOHENBERG-KOHN theorem, in which the energies and potentials of the system are postulated to be electron density functionals. In this dissertation, DFT was used to investigate the materials characteristics of the different  $\text{Hf}_{1-x}\text{Zr}_x\text{O}_2$  crystal phases. The total energies and the vibrational entropies were computed and compared to study the stability of the crystal phases in  $\text{Hf}_{1-x}\text{Zr}_x\text{O}_2$  compounds. Furthermore, the temperature, electric field and strain dependence of the total energies and volumes from DFT are used as input parameters for a classical Gibbs energy model, which is detailed in [section 3.3](#). Mainly the DFT programs, Abinit<sup>78,79</sup> and FHI-Aims<sup>80-82</sup>, are used in this dissertation. However, other programs such as Quantum Espresso<sup>83,84</sup> and Castep<sup>85</sup> were occasionally used to compare and validate results. Pseudopotentials for Abinit and Quantum Espresso are taken from the GBRV library<sup>86</sup>.

In [section 3.1](#) of this chapter, the approach of DFT is outlined and discussed. In [section 3.2](#), geometry limitations and considerations are communicated with a special emphasis on the periodicity of the  $\text{Hf}_{1-x}\text{Zr}_x\text{O}_2$  thin films. Thereafter, a Gibbs energy model is detailed in [section 3.3](#), and how the single contributions of this model can be calculated from DFT.

## 3.1 Approach

DFT was initially established by PIERRE HOHENBERG, WALTER KOHN and LU JEU SHAM<sup>87,88</sup> and deals with the solution of the SCHRÖDINGER equation of a many-body system with a finite number of interacting particles. In many-body systems, the interactions of every particle to every other particle must be considered, which rapidly ends in insoluble problem sizes. Because of the BORN-OPPENHEIMER approximation<sup>89</sup>, which splits the SCHRÖDINGER equation in two parts, namely one for the electrons and one for the nuclei by arguing that the electron velocity is very high and that the nuclei cannot follow (mass ratio  $m/M \sim 1/10000$ ), the electronic and ionic part of the SCHRÖDINGER equation can be solved independently, reducing the problem size. The time-independent SCHRÖDINGER equation for the electrons, after the application

### 3 Density Functional Theory

of the BORN-OPPENHEIMER (adiabatic) approximation, is

$$H_e \Phi_e(\mathbf{r}, \mathbf{R}) = E_e \Phi_e(\mathbf{r}, \mathbf{R}), \quad (3.1)$$

with  $\Phi_e$  and  $E_e$  the wave functions and eigenvalues of the electrons, and  $\mathbf{r}$  and  $\mathbf{R}$  are the sets of all electronic and ionic coordinates, respectively.  $H_e$  is the electronic Hamiltonian and is

$$H_e = T_e(\mathbf{r}) + V_{eN}(\mathbf{r}, \mathbf{R}) + V_{ee}(\mathbf{r}), \quad (3.2)$$

with  $T_e(\mathbf{r})$  the kinetic energy of the electrons,  $V_{eN}(\mathbf{r}, \mathbf{R})$  the potential energy between electrons and nuclei, and  $V_{ee}$  the potential energy from the Coulomb electron-electron repulsions.  $H$ ,  $T$  and  $V$  are mathematical operators. Because of the BORN-OPPENHEIMER approximation, the ionic part of the SCHRÖDINGER equation can be solved independently and enters the solution of the electronic SCHRÖDINGER equation only as a static electric potential.

The basic principle of DFT lies in using the electron density  $n(\mathbf{r})$  as the main variable instead of the spatial coordinates, which means that the energy contributions (e.g. total energy) of the system are functionals of the electron density. In their publication from 1964, Hohenberg and Kohn proved that the ground state wave function of a system is unambiguously defined by the electron density  $n(\mathbf{r})$ <sup>87</sup>. One year later, Kohn and Sham used this theorem and introduced a method that minimizes the energy functional  $E[n(\mathbf{r})]$  by varying  $n(\mathbf{r})$ . With this method the electronic SCHRÖDINGER equation for all electrons could be divided in  $n_e$  one electron SCHRÖDINGER equations ( $n_e$  is the number of electrons), which are today named the KOHN-SHAM (K.S.) equations<sup>88</sup>. These equations are

$$\left( -\frac{1}{2}\nabla^2 + v_{\text{eff}}(\mathbf{r}) \right) \phi_j(\mathbf{r}) = \epsilon_j \phi_j(\mathbf{r}), \quad (3.3)$$

with  $\phi_j(\mathbf{r})$  and  $\epsilon_j$  the K.S. wave functions and eigenvalues for an electron  $j$  ( $j = 1 \dots n_e$ ), respectively. It should be noted that [equation \(3.3\)](#) is given in atomic units. The K.S. effective potential is

$$v_{\text{eff}}(\mathbf{r}) = v_{\text{ext}}(\mathbf{r}) + \int \frac{n(\mathbf{r}')}{|\mathbf{r} - \mathbf{r}'|} d\mathbf{r}' + \frac{\delta E_{\text{XC}}[n(\mathbf{r})]}{\delta n(\mathbf{r})}, \quad (3.4)$$

and the electron density is constructed according to

$$n(\mathbf{r}) = \sum_j^{n_e} |\phi_j(\mathbf{r})|^2, \quad (3.5)$$

with the external potential  $v_{\text{ext}}(\mathbf{r})$  and  $E_{\text{XC}}[n(\mathbf{r})]$  the XC functional. Apparently, these equations form a self-consistent problem and the solution must be iterative. A typical DFT computation involves two steps: (i) the electronic structure problem is solved iteratively by using [equations \(3.3\)](#) to [\(3.5\)](#) and (ii) the nuclei are moved according to the calculated electronic potential to minimize the ionic forces. This steps

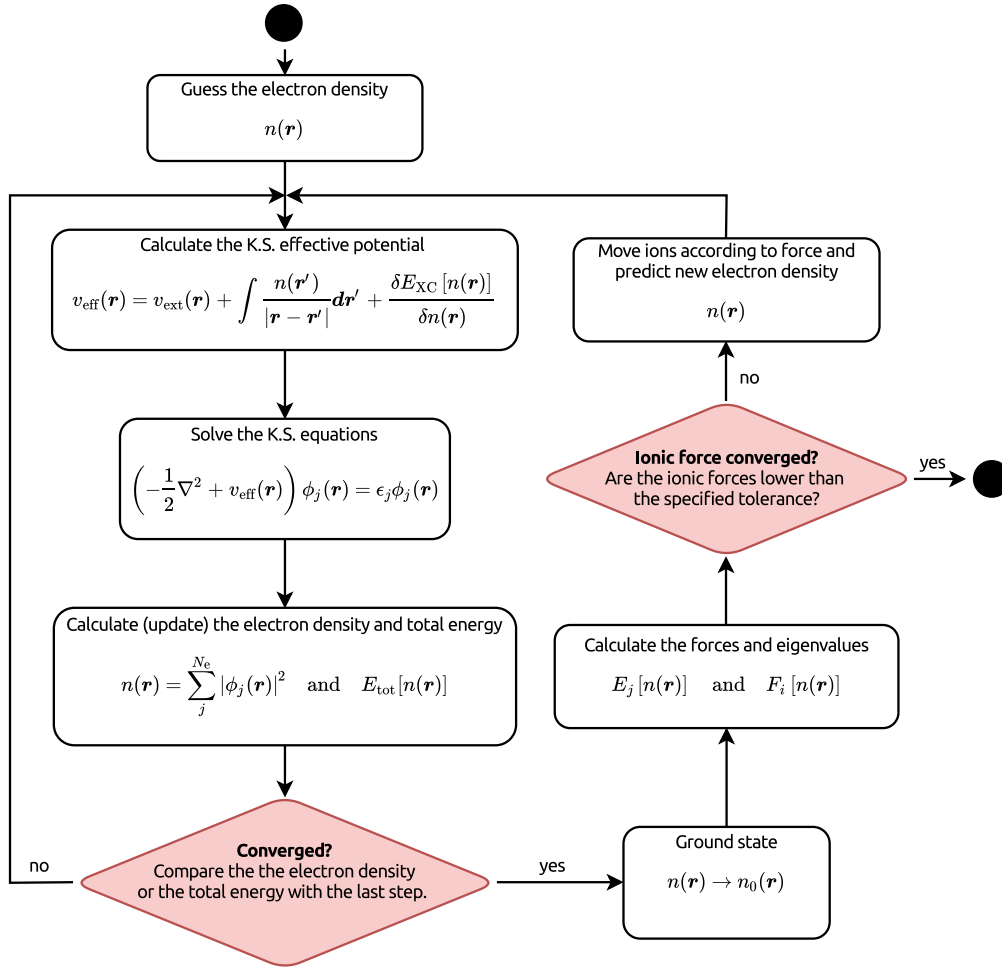


**Figure 3.1:** Schematic representation of the solution process of the electronic structure (K.S. equations) and of the ionic structure in DFT.

follows a recalculation of the electronic potential and is repeated iteratively until the remaining forces are below a certain limit. Finally, the main results from DFT calculations are the ground state electronic structure (electron density and eigenvalues) for an ionic structure with minimized forces of an arrangement of atoms (e.g. in a crystal), which are exclusively calculated from first-principles. A schematic flowchart of the solution process in a DFT computation can be found in [figure 3.1](#).

The advantages of DFT in comparison to HARTREE-FOCK lies in the acceleration of the computation by using the electron density with three dimensions instead of the spatial coordinates with  $3n_e$  dimensions and the inclusion of the full correlation of the electrons. However, the exact XC contribution in [equation \(3.4\)](#) is unknown but crucial for the results from DFT. Since we do not know the exact form of the XC functional, the functional is approximated. One of the first and simplest approach for the XC

functional was the local-density approximation (LDA), in which the XC functional is based on the homogeneous electron gas (Jellium) density<sup>88,90–92</sup> ( $E_{\text{XC}}[n(\mathbf{r})]$ ). An expansion of the LDA is the semi-local generalized gradient approximation (GGA), in which the XC functional is a function of the electron density and simultaneously the gradient of the electron density ( $E_{\text{XC}}[n(\mathbf{r}), \nabla n(\mathbf{r})]$ ) [93]. The GGA functional is an attempt to improve LDA by including the effects of inhomogeneities with the gradient of the electron density. More sophisticated methods are hybrid XC functionals, in which a local or semi-local XC functional is mixed with some part from the FOCK exchange. The HSE06<sup>94–96</sup> functional is a commonly used hybrid functional and results for different phases of HfO<sub>2</sub> are calculated by Barabash et al.<sup>37</sup> and for Si-doped HfO<sub>2</sub> by Künneth et al.<sup>3</sup>. In comparison to the less expensive local and semi-local XC functionals (LDA and GGA), hybrid functionals particularly improve the band gap problem, which is usually underestimated for LDA and GGA computations.

Apart from the XC functional, the representation of the K.S. orbitals plays a crucial role. Typically, the K.S. orbitals ( $\phi_j(\mathbf{r})$ ) are expanded in  $n_{\text{basis}}$  basis functions ( $\psi_i(\mathbf{r})$ ),

$$\phi_j(\mathbf{r}) = \sum_i^{n_{\text{basis}}} c_{ij} \psi_i(\mathbf{r}). \quad (3.6)$$

Several basis functions exist in the literature with different advantages and disadvantages with regards to the arrangement of the atoms and intended computation case. Three common choices for the basis sets are (i) GAUSSIAN-type orbitals (GTOs) (e.g. used in NWChem<sup>97</sup>), (ii) numerical basis functions (e.g. used in FHI-Aims<sup>80–82</sup> and Siesta<sup>98</sup>) and (iii) plane waves (e.g. used in Abinit<sup>78,79</sup>, Castep<sup>85</sup> and Quantum Espresso<sup>83,84</sup>). GTOs are often used for molecules and a lot of literature is available. However, they are non-orthogonal (superposition errors) and awkward to systematically improve. In numerical basis sets, the Gaussian-like function is replaced with a radial-shaped function which is fully flexible. Plane waves are orthogonal and can systematically be improved by increasing the kinetic cut-off of the waves, but pseudopotentials are needed as the rapid oscillations of the wave functions close to the nucleus would need a vast number of waves to be accurately represented. In addition, vacuums are as expensive in the computation as space occupied with atoms in the case of wave functions and are nearly for free for the numerical basis and GTO sets.

## 3.2 Limitations

DFT is presently limited to a few hundred to thousand electrons because of the currently available computer performance. In the solution process of a DFT computation (c.f. figure 3.1), all mathematical problems can be expressed in a linear  $\mathcal{O}(n_e)$  fashion except the solution of the eigenvalues and eigenvectors of equation (3.3) ( $n_e$  is the number of electrons)<sup>99</sup>. The solution of the eigenvalue problem scales approximately with cubic-order with the number of electrons ( $\sim \mathcal{O}(n_e^3)$ ) and is thus the limiting part in DFT computations. A very common and clever approach to overcome this limit



for crystals is to apply periodic boundary conditions (PBCs) by making the basis set a lattice periodic function (c.f. BLOCH's theorem) and introducing the wave vector  $k$ .

In particular, in this dissertation, the restriction of the number of electrons played an important role. In the case of  $\text{Hf}_{1-x}\text{Zr}_x\text{O}_2$ , when surfaces and interfaces are conjectured to be involved in the stabilization of the ferroelectric  $p$ - $o$ -phase, the computation of the interaction between interfaces, surfaces, and bulk (e.g. to sample a whole grain) would reveal interesting results. However, such collective computations would require much more electrons than possible in DFT and could thus not be performed.

### 3.3 Thermodynamics

$\text{Hf}_{1-x}\text{Zr}_x\text{O}_2$  is only ferroelectric in thin film geometries and not in bulk crystals. This experimental observation agrees well with the equilibrium bulk phase diagram for pressure and temperature, which is shown in [figure 2.1](#). More importantly, [figure 2.1](#) demonstrates that the influence of pressure, temperature or their combination cannot induce  $\text{HfO}_2$  to transform into the  $p$ - $o$ -phase, which was experimentally found as the root cause of the ferroelectricity in  $\text{Hf}_{1-x}\text{Zr}_x\text{O}_2$  thin films. Therefore, another physical factor must be present in  $\text{Hf}_{1-x}\text{Zr}_x\text{O}_2$  thin films, which is essential for the ferroelectric phase formation. These factors can be collectively expressed in a single Gibbs free energy function, which is for a given volume  $V$  of a crystal phase  $\alpha \in \{m, o, o', p-o, p-o', t, c\}$

$$G^\alpha = U^\alpha + pV^\alpha - V_0^\alpha \sum_{ij} \epsilon_{ij}^{d,\alpha} \sigma_{ij}^d + F_{\text{vib}}^\alpha - TS_{\text{conf}}^\alpha - V_0^\alpha \mathbf{D}^\alpha \mathbf{E} + \gamma^\alpha \mathcal{A} + \sum_I \mu_I N_I, \quad (3.7)$$

with  $U$  the internal energy,  $p$  the hydrostatic pressure,  $V$  the volume,  $V_0$  the reference volume,  $T$  the temperature,  $F_{\text{vib}} = E_{\text{ZPE}} - TS_{\text{vib}}$  the vibrational entropy contribution,  $E_{\text{ZPE}}$  the energy of the zero point motion,  $S_{\text{vib}}$  the vibrational entropy,  $S_{\text{conf}}$  the configurational entropy,  $\sigma_{ij}^d$  the deviatoric stress tensor,  $\epsilon_{ij}^d$  the deviatoric strain tensor,  $\mathbf{D}$  the electric displacement field,  $\mathbf{E}$  the electric field and  $\gamma$  the surface energy necessary to create or destroy a surface area  $\mathcal{A}$  ( $\gamma = dU/d\mathcal{A}$ ). In addition,  $\gamma$  can also be interpreted as an interface (or even grain boundary or domain wall) energy necessary to create the surface between two different crystal phases  $\{\alpha_1, \alpha_0\}$  as  $\gamma_{\alpha_1-\alpha_0} = d(U_{\alpha_1} - U_{\alpha_0})/d\mathcal{A}$ .  $\mu_I$  is the atomic chemical potential and  $N_I$  are the number of atoms of the species  $I$ .

The *first* energy contribution in [equation \(3.7\)](#) is the internal energy ( $U$ ), which can directly be obtained from DFT computations as the total energy  $E_{\text{tot}}[n_0(\mathbf{r})]$  of the ground state electron density from the solution of the K.S. equations. The total energy differences for the dissimilar phases are illustrated in [figure 3.2](#) (a). The *second* and *third* energy contributions ( $pV^\alpha - V_0^\alpha \sum_{ij} \epsilon_{ij}^{d,\alpha} \sigma_{ij}^d$ ) concern the mechanical deformation of the crystal and can likewise be computed from DFT by applying either strain or stress to the cell of the crystal. Alternatively, the  $U(V)$  relation of a crystal can be obtained by fitting an equation of state (e.g. BIRCH-MURNAGHAN). The change of the energy with strain or stress for the different phases in  $\text{Hf}_{1-x}\text{Zr}_x\text{O}_2$

### 3 Density Functional Theory

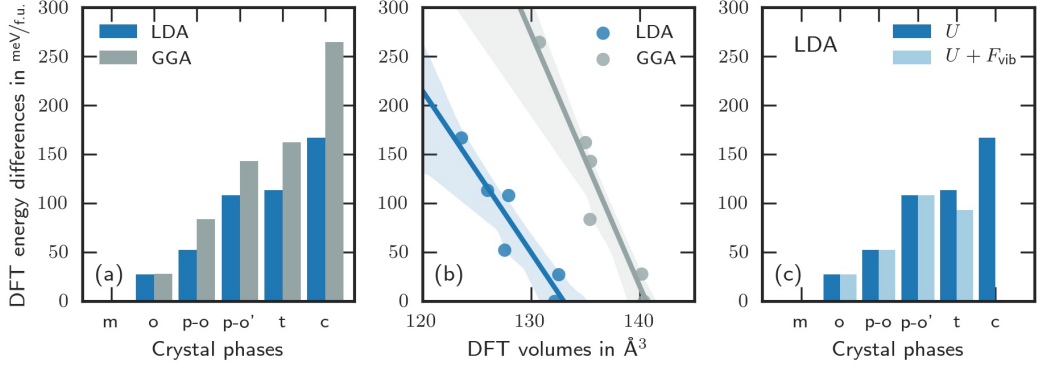


**Figure 3.2:** (a) Comparison of the total energy differences with respect to the  $m$ -phase from the LDA and GGA XC functionals, (b) correlation of the total energy differences with the volumes and (c) comparison of the total energy differences with and without the vibrational entropy contribution at 300 K. The calculations were consistently performed using the DFT code Abinit<sup>78,79</sup> with the PAW pseudo-potentials from the GBRV<sup>86</sup> library for HfO<sub>2</sub>. The vibrational entropy contribution of the  $c$ -phase is set to zero since it is a naturally unstable phase<sup>100</sup>.

varies strongly and can easily result in the stabilization of a different phase over the  $m$ -phase (c.f. figure 2.1)<sup>10,21,26</sup>. The *fourth* and *fifth* energy contributions ( $F_{\text{vib}} - TS_{\text{conf}}$ ) are the vibrational and configurational entropy of the crystal. A third possible entropy contribution from the electrons is neglected here as this contribution is zero for insulators like Hf<sub>1-x</sub>Zr<sub>x</sub>O<sub>2</sub>. The vibrational entropy  $S_{\text{vib}}$  can be calculated from phonon modes of the crystal using e.g. the finite difference<sup>100</sup> or the density functional perturbation theory (DFPT)<sup>101-104</sup> approach and is illustrated in figure 3.2 (c) for a temperature of 300 K. Figure 3.2 (c) shows that the vibrational entropies of the phases are indistinguishable on the level of meV/f.u.<sup>-1</sup> with the exception of the  $t$ -phase, which has a higher entropy than the other phases. Since the  $c$ -phase is naturally unstable, the calculation of its vibrational entropy is ill-defined and set to zero. The *sixth* contribution ( $V_0^\alpha \mathbf{D}^\alpha \mathbf{E}$ ) in equation (3.7) arises from a possible applied electric field and can be rewritten as  $V_0(\epsilon_r \epsilon_0 |\mathbf{E}|^2 + \mathbf{P} \mathbf{E})$ . In this form it is obvious that the contribution is symmetric (parabolic shaped) for all crystal phases in Hf<sub>1-x</sub>Zr<sub>x</sub>O<sub>2</sub>, except for the  $p$ - $o$  and  $p$ - $o'$ -phase with a non-zero polarization  $\mathbf{P}$ . Furthermore, since the dielectric constants ( $\epsilon_r$ ) for all the phases are of the same order of magnitude (20 to 40), the contributions from the electric field almost cancel out in the energy difference for all phases, except for the  $p$ - $o$  and  $p$ - $o'$ -phase<sup>10,26</sup>. This additional contribution from the electric field is suspected to be responsible for the electric-field-driven phase transformation from the  $p$ - $o$  to the  $t$ -phase, which produces pinched hystereses in measurements<sup>1,74</sup>. The *seventh* contribution ( $\gamma \mathcal{A}$ ) is caused by interfaces or surfaces (c.f. section 2.3) present in the thin films. The interface energy ( $\gamma$ ) of interfaces with a good coherence (e.g. domain walls, interphase) may have a small value and of an interface with a worse coherence (e.g. grain boundaries) may have a higher value<sup>1</sup>.

The surface energy is generally expected to be higher than any kind of interfaces (c.f. [section 2.3](#)). Furthermore,  $\gamma$  is expected to depend on the crystal phase and doping of the material.

In comparison to the first seven contributions in [equation \(3.7\)](#), which address “physical” contributions, the *last* contribution ( $\sum_I \mu_I N_I$ ) deals with the “chemical” addition or removal of atoms (point defects) and is a special contribution as it is usually defined by the manufacturing process of the  $\text{Hf}_{1-x}\text{Zr}_x\text{O}_2$  thin films. Typically, atoms are exchanged if the dopant is substitutionally incorporated or atoms are added if the dopant is interstitially inserted. In the case of ionic charge compensation of dopants with oxygen vacancies (c.f. [section 2.4](#)), atoms are removed. In general, point defects in  $\text{Hf}_{1-x}\text{Zr}_x\text{O}_2$  have a significant influence on the ferroelectricity of  $\text{Hf}_{1-x}\text{Zr}_x\text{O}_2$  and are computationally studied in literature<sup>3,71,72</sup>.

The final goal of the Gibbs energy model, which was described in the past paragraphs, is to explain why the ferroelectric *p-o*-phase, which is measured and found as the root cause of the ferroelectricity in experiments, is the thermodynamic ground state of the system. After the computation of the contributions of [equation \(3.7\)](#), the thermodynamic equilibrium phase can be obtained as

$$\mathcal{G}(p, \mathcal{A}, \mathbf{E}, \boldsymbol{\sigma}^d, T) = \min_{\alpha} G^{\alpha}(p, \mathcal{A}, \mathbf{E}, \boldsymbol{\sigma}^d, T) . \quad (3.8)$$

It should be noted that the contributions in [equation \(3.7\)](#) are in fact not independent of each other and a crosswise influence is expected, which magnitude must be checked carefully. Furthermore, the Gibbs free energy model only reflects the ground state of a system and not what happens if the experimentally found *p-o*-phase is in a “metastable” state<sup>105</sup>.



# 4 Publications

As this dissertation is publication based, the following chapter contains a summary of the publications and highlights the individual contribution of the author. A copy of the respective publication can be found in the appendix of this dissertation.

## 4.1 Modeling Ferroelectric Film Properties and Size Effects from Tetragonal Interlayer in $\text{Hf}_{1-x}\text{Zr}_x\text{O}_2$ Grains

Christopher Künneth, Robin Materlik, and Alfred Kersch  
J. Appl. Phys., vol. 121, no. 20, p. 205304, 2017.  
DOI: [10.1063/1.4983811](https://doi.org/10.1063/1.4983811)

### 4.1.1 Summary

An explanation of the ferroelectricity in polycrystalline  $\text{Hf}_{1-x}\text{Zr}_x\text{O}_2$  thin films is that an interface energy contribution between grains of different sizes and crystal phases favors the polar, orthorhombic (*p-o*-phase) phase. Each combination of adjacent crystal phases, building an interface, in  $\text{Hf}_{1-x}\text{Zr}_x\text{O}_2$  has its individual interface energy. It is experimentally observed that  $\text{Hf}_{1-x}\text{Zr}_x\text{O}_2$  is polycrystalline and that crystal phases coexist. Furthermore, it was observed that the polarization of the thin films and the fractions of crystal phases present in the film vary with the film thickness. This strongly indicates an influence of the film thickness on the crystal phase formation (size effect). In addition, experimental HAADF-STEM measurements suggest a pinned interlayer between the core of the grain and the electrodes. The phase of the interlayer seems to be fixed to the *t*-phase. Based on these findings, a Gibbs energy model to investigate and describe the relation between the grain sizes and the present crystal phases is developed in this publication. This model contains the total energy, the vibrational entropy for 300 K and the interface energy. The film thickness and grain radius distribution, which are necessary as a geometry factor to calculate the interface energy contribution to the Gibbs energy, are taken from experimental measurements. The total energy and vibrational energy are calculated with DFT computations. The interface energies are chosen as fit parameters and are adapted to the experimental values for the polarization and the dielectric constants match with the computation. As the interlayer is fixed to the *t*-phase, only interface energies between the crystal phase of the core and the *t*-phase interlayer are necessary for the model, which reduces the number of unknowns in the optimization problem to two interface energies for  $\text{ZrO}_2$  and two for  $\text{HfO}_2$ . The values between pure  $\text{ZrO}_2$  and  $\text{HfO}_2$  are linear interpolated. The adaption process is repeated for the total energies and vibrational entropies for different DFT XC functionals and programs. It turned out that the final and fitted set of interface energies give polarizations and dielectric constants that slightly differ quantitatively but agree qualitatively. Furthermore, the magnitudes of the interface energies are physically reasonable and in the expected range of experimental measurements. More interestingly and in summary, with just four parameters (two for  $\text{HfO}_2$  and two for  $\text{ZrO}_2$ ), a Gibbs energy model with a *t*-phase interlayer around a grain suffices to explain the ferroelectricity in the  $\text{Hf}_{1-x}\text{Zr}_x\text{O}_2$  system. This simple model gives credibility to the interface energies as the root cause of the formation of the *p-o*-phase and ferroelectricity in  $\text{Hf}_{1-x}\text{Zr}_x\text{O}_2$ .

### 4.1.2 Contribution

The main idea of this work arose from an earlier work of Materlik et al.<sup>10</sup>. They introduced a Gibbs energy model based on a single grain, which was successful in explaining the ferroelectricity in  $\text{Hf}_{1-x}\text{Zr}_x\text{O}_2$ . In this work, the idea was further developed and the surface energies were replaced by more realistic interface energies.

I carried out all the DFT calculations with the Abinit and FHI-Aims codes, except the calculations of the total energies for *SM-LDA*, which was done earlier by Robin

#### *4.1 Modeling Ferroelectric Film Properties and Size Effects from Tetragonal Interlayer*

Materlik. The idea of the Gibbs energy model to investigate single grains was initially from Alfred Kersch. I implemented the Gibbs energy model in a Python program, including the optimization process using global optimization algorithms from Scipy. I wrote the majority of the manuscript and created all the figures.

## 4.2 The Impact of Charge Compensated and Uncompensated Strontium Defects on the Stabilization of the Ferroelectric Phase in HfO<sub>2</sub>

Robin Materlik\*, Christopher Künneth\*, Thomas Mikolajick, and Alfred Kersch

\*Contributed equally to this work.

Appl. Phys. Lett., vol. 111, no. 8, p. 82902, 2017.

DOI: [10.1063/1.4993110](https://doi.org/10.1063/1.4993110)



### 4.2.1 Summary

Sr is a divalent dopant on a substitutional metal position ( $\text{Sr}_{\text{Hf}}$ ) in  $\text{Hf}_{1-x}\text{Zr}_x\text{O}_2$ . Sr-doped  $\text{HfO}_2$  thin films are experimentally known to show a ferroelectric hysteresis from 1.7 f.u. % to 7.9 f.u. % doping concentration. In this publication, the formation energies and total energies of the point defects,  $\text{Sr}_{\text{Hf}}$ ,  $\text{Sr}_{\text{I}}$ , and  $\text{Sr}_{\text{Hf}}\text{V}_{\text{O}}$  along with oxygen vacancies ( $\text{V}_{\text{O}}$ ) in  $\text{HfO}_2$  are computed and analyzed. Firstly, the total energies and volumes for the substitutional Sr defect ( $\text{Sr}_{\text{Hf}}$ ) of two different DFT programs, Abinit and FHI-Aims, are compared with the result that the trends of the energy differences are very similar. Afterward, the analysis of the energy differences with respect to the  $m$ -phase of all the Sr-related point defects in the different crystal phases reveals that the ionically compensated  $\text{Sr}_{\text{Hf}}\text{V}_{\text{O}}$  defect strongly favors the non-ferroelectric  $t$ -phase with increasing doping concentration, while the electronically compensated  $\text{Sr}_{\text{Hf}}$  defect favors the ferroelectric, polar-orthorhombic ( $p$ - $o$ -phase) phase. However, the energetic promotion of the  $p$ - $o$ -phase with increasing concentration of substitutional  $\text{Sr}_{\text{Hf}}$  doping alone is not sufficient to promote the  $p$ - $o$ -phase lower than the  $m$ - and  $o$ -phase, and thus a destabilization mechanism has to be assumed. The formation energies of the Sr-related defects in this publication are computed for two oxygen partial pressures (atomic chemical potentials). Oxygen-rich conditions are reflected with  $\text{O}_2$  and oxygen-poor conditions with  $\text{TiO}_2$ . Since  $\text{O}_2$  is a typical precursor in the ALD production process of such thin films and  $\text{TiN}$  is a typical electrode material,  $\text{O}_2$  samples the manufacturing condition and  $\text{TiO}_2$  the lifetime (of a device) of the  $\text{HfO}_2$  thin film. Formation energies for oxygen-rich (manufacturing) conditions reveal the  $\text{Sr}_{\text{Hf}}$  defect lower in energy and more likely to create than the  $\text{Sr}_{\text{Hf}}\text{V}_{\text{O}}$  defect. As a consequence, the  $p$ - $o$ -phase is favored with increasing Sr doping concentration. On the other hand, the formation energy of oxygen-poor (lifetime) conditions favors the  $\text{Sr}_{\text{Hf}}\text{V}_{\text{O}}$  defect with the results that the  $p$ - $o$ -phase is strongly disfavored. It was concluded that  $\text{Sr}_{\text{Hf}}$  defects prevail after the deposition process of the film, while during the lifetime more and more  $\text{Sr}_{\text{Hf}}$  transform to  $\text{Sr}_{\text{Hf}}\text{V}_{\text{O}}$  along with a degradation of the polarization of the films.

### 4.2.2 Contribution

The DFT calculations were equally carried out by Robin Materlik and me. Specifically, I conducted all the computations with FHI-Aims and calculated the formation energies with the necessary corrections from the raw DFT output. Alfred Kersch came up with the idea and story of this publication. Robin Materlik and I wrote the text in several iterations and drew the conclusion together with Alfred Kersch.

### **4.3 Impact of Four-Valent Doping on the Crystallographic Phase Formation for Ferroelectric HfO<sub>2</sub> from First-Principles: Implications for Ferroelectric Memory and Energy-Related Applications**

Christopher Künneth, Robin Materlik, Max Falkowski, and Alfred Kersch  
ACS Appl. Nano Mater., vol. 1, no. 1, pp. 254–264, Jan. 2018.  
DOI: [10.1021/acsnm.7b00124](https://doi.org/10.1021/acsnm.7b00124)

### 4.3.1 Summary

Ferroelectricity was first found by Böske et al.<sup>11</sup> in 2011 in HfO<sub>2</sub> thin films of 10 nm thickness with silicon doping. For this reason, silicon is one of the most prominent dopants in HfO<sub>2</sub> and additionally has a high importance in the industry as it is utilized in high doping concentrations to stabilize the *t*-phase with a high dielectric constant for applications that exploit the linear dielectricity. Nevertheless, the influence on the ferroelectricity of various other atoms like Sr, Ba, Mg, Al, Y, La, Gd, Ga, In, etc. was experimentally investigated in Hf<sub>1-x</sub>Zr<sub>x</sub>O<sub>2</sub>. Therefore, in this publication, first the total energies and volume changes of Si-doped and pure HfO<sub>2</sub> from two different DFT programs (Abinit and FHI-Aims) and three distinct XC approximations (LDA, PBE, and HSE06) are compared. It turned out that the total energies and volumes in this comparison are qualitatively the same but differ quantitatively. In addition, the energetic trends of the phases remain the same for the explored programs and XCs approximations. The formation energies for three different silicon complexes (Si<sub>Hf</sub>, Si<sub>Hf</sub>V<sub>O</sub>, V<sub>O</sub>, and Si<sub>I</sub>) and the oxygen vacancy (V<sub>O</sub>) in HfO<sub>2</sub> are computed as a function of the Fermi level. Based on these formation energies and two different atomic chemical potentials for oxygen, rendering the manufacturing and lifetime of a thin Hf<sub>1-x</sub>Zr<sub>x</sub>O<sub>2</sub> film, it was concluded that the incorporation of silicon (Si<sub>Hf</sub>) substitutionally is more likely during the deposition of the HfO<sub>2</sub> thin films in the case of all crystal phases. On the contrary, during the lifetime of a thin film in a device, the creation of an oxygen vacancy (V<sub>O</sub>) becomes energetically more likely. Consequently, it was concluded that the substitutional silicon (Si<sub>Hf</sub>) defect, which is created during the manufacturing process of the film, may be compensated with an oxygen vacancy (V<sub>O</sub>), which is created during the electric field cycling (lifetime) of the device. If both defects are already present in the material, the compensation of the substitutional silicon defect (Si<sub>Hf</sub>) with an oxygen vacancy (V<sub>O</sub>) releases an energy from 0.5 eV to 0.27 eV, depending on the phase. Along with the formation energies, the analysis of the DFT total energy differences with respect to the *m*-phase reveals a small energy change of  $\sim 10$  meV f.u.<sup>-1</sup> for the incorporation of the oxygen vacancy (V<sub>O</sub>) and  $\sim 100$  meV f.u.<sup>-1</sup> for the substitutional silicon defect (Si<sub>Hf</sub>). After determining the most likely silicon-related defect as the substitutional one, the total energies of the substitutional and silicon doped HfO<sub>2</sub> of the crystal phases are computed and analyzed for the silicon concentrations of 3.125 f.u. %, 6.25 f.u. % and 12.5 f.u. %. Böske et al.<sup>11</sup> found ferroelectricity in silicon doped HfO<sub>2</sub> in a concentration window from 2.6 f.u. % to 6 f.u. %. While the lower bound of 2.6 f.u. % does not agree with the computations without the assumption of a destabilization mechanism of the *m*- and *p-o'*-phase (c.f. section 4.1), the upper bound from the computations agrees well with the experiments. This simultaneously means that silicon doping alone is not sufficient to stabilize the *p-o*-phase. Apart from Si-doped HfO<sub>2</sub>, the total energies and formation energies of substitutional C-, Ge-, Ti-, Sn-, Zr- and Ce-doped HfO<sub>2</sub> are analyzed, demonstrating that Ce-doped HfO<sub>2</sub> has a similar influence on the energies as Si. Finally, the geometrical incorporation of the dopants is examined to complement the study.

### 4.3.2 **Contribution**

I conducted all the necessary DFT calculations with the DFT packages FHI-Aims and Abinit within this publication. I analyzed the raw DFT data and drew the conclusion together with Alfred Kersch. The structure and composition of the manuscript were developed by Alfred Kersch and me. I prepared all the figures in the manuscript and wrote the majority of the text together with Alfred Kersch. Robin Materlik and Max Falkowski worked on the text and conclusion of the manuscript.

#### **4.4 Ferroelectric Phase Transitions in Nanoscale HfO<sub>2</sub> Films Enable Giant Pyroelectric Energy Conversion and Highly Efficient Supercapacitors**

Michael Hoffmann, Uwe Schroeder, Christopher Künneth, Alfred Kersch, Sergej Starschich, Ulrich Böttger, and Thomas Mikolajick  
Nano Energy, vol. 18, pp. 154–164, 2015.  
DOI: [10.1016/j.nanoen.2015.10.005](https://doi.org/10.1016/j.nanoen.2015.10.005)

#### 4.4.1 Summary

In this joint study of experimental measurements with an emphasis on the theoretical description of the pyroelectric effect in polycrystalline materials, the energy conversion and storage characteristic of 3.8, 4.3 and 5.6 mol% Si-doped HfO<sub>2</sub> thin films are investigated. Measurements of the energy storage density of the thin films show a value of 40 Jcm<sup>-3</sup> with a very high efficiency of 80% for a silicon concentration of 5.6 mol%. More interestingly, a giant pyroelectric coefficient of up to 1300 μCm<sup>-2</sup>K<sup>-1</sup> under electric field cycling for 5.6 mol% could be observed. An estimation of the pyroelectric effect from the linear thermal expansion of the crystal reveals the pyroelectric coefficient to be around 23 μCm<sup>-2</sup>K<sup>-1</sup>. Therefore, it was concluded that the giant measured pyroelectric coefficient in this work is unlikely only caused by the thermal expansion but rather from a temperature-driven phase transition from the *p-o*-phase to the non-polar *t*-phase. Consequently, the standard formulation of the (proper) pyroelectric coefficient, which includes (i) the pyroelectric coefficient for constant strain (primary pyroelectric effect) and (ii) the contribution from thermal expansion (secondary pyroelectric effect), is expanded with (iii) a phase transition and temperature (*T*) dependent contribution by introducing a normalized function. Later, this function turned out to be equal to the normalized function of the remanent polarization with the temperature ( $P_r(T)$ ;  $0 \leq P_r(T) \leq 1$ ). The width of this normalized, remanent polarization against the temperature is explained and attributed to be caused by the grain radius distribution of the Hf<sub>1-x</sub>Zr<sub>x</sub>O<sub>2</sub> thin films. Using this relation, the correlation between the different grain radii and their CURIE temperature could be derived for the investigated silicon concentrations. Furthermore, the pyroelectric, harvestable energy per OLSEN cycle calculations have shown values of 20.27 Jcm<sup>-3</sup> for 5.6 mol% silicon concentration, which compares very well with other materials. Apart from measurements under applied electric field, static pyroelectric measurements without an electric field reveal a pyroelectric coefficient of up to 53 μCm<sup>-2</sup>K<sup>-1</sup>. Finally, 9.5 K and 19.6 Jcm<sup>-3</sup> was measured for the electrocaloric (inverse of the pyroelectric) effect. To complement the study, possible applications are discussed.

#### 4.4.2 Contribution

This work arose from a close collaboration with the Namlab at the TU Dresden and the Institut für Werkstoffe der Elektrotechnik at the RWTH Aachen. The polarization measurements at different temperatures under applied electric field of Si-doped HfO<sub>2</sub> thin film samples were conducted by Michael Hoffmann, while the static measurements of the pyroelectric coefficient were done by Sergej Starschich. The analysis and interpretation of the data in regard to the pyroelectricity, storage and its theoretical description were carried out in close discussions. My work included the analysis of the raw measurements of the remanent polarization and the scanning electron microscopy (SEM) measurements.

## 5 Summary & Conclusion

The *first publication*, which arose in this dissertation (reference 1), addresses the question, why  $\text{Hf}_{1-x}\text{Zr}_x\text{O}_2$  exhibits ferroelectricity under thin film conditions. Based on a Gibbs energy model, the extensive study of Materlik et al.<sup>10</sup> investigates the energetic influence of different physical factors, such as temperature, strain and electric field in  $\text{Hf}_{1-x}\text{Zr}_x\text{O}_2$ . They found that these factors alone or a combination cannot explain the stabilization of the *p-o*-phase, which is believed to be the source of the ferroelectric characteristic in  $\text{Hf}_{1-x}\text{Zr}_x\text{O}_2$ . For this reason, they proposed the surface energy, which is different for each crystal phase and its magnitude depends on the surface area, as the main cause for the stabilization of the *p-o*-phase and examined this approach with a simple Gibbs energy model. The first publication of this dissertation expands this simple Gibbs energy model of Materlik et al.<sup>10</sup> by replacing surface energies with interface energies, which better fit the requirements of the polycrystalline  $\text{Hf}_{1-x}\text{Zr}_x\text{O}_2$  thin films. Furthermore, the new and improved Gibbs energy model, which uses interface energies, is convoluted with a grain radius distribution from experiments to directly compute the polarization and dielectric constant of a thin film. Additionally, the computed polarizations and dielectric constants for  $\text{Hf}_{1-x}\text{Zr}_x\text{O}_2$  are compared with experiments while the interface energies are adapted until both match together. The fitted and adapted interface energies for the different crystal phases turned out to be in a reasonable but expected order of magnitude in comparison to the experiments. More importantly, the polarizations and the dielectric constants of the thin  $\text{Hf}_{1-x}\text{Zr}_x\text{O}_2$  films could be reproduced with a good agreement, showcasing that the interface energies have the capability to explain the ferroelectricity in  $\text{Hf}_{1-x}\text{Zr}_x\text{O}_2$ . However, a perfect match of the calculated and measured polarizations could not be achieved, which indicate a missing parameter in the model.

Although many arguments exist, which support the interface energy as the main cause of the stabilization of the *p-o*-phase in order that  $\text{Hf}_{1-x}\text{Zr}_x\text{O}_2$  becomes ferroelectric, other physical factors or combination of the factors should be considered. An influential factor to optimize any materials characteristics is doping. However, the investigation of doping on the phase stability and ferroelectric characteristics means not only the study of the interstitial or substitutional incorporation of a dopant in the crystal but also the consideration of the side effects such as the ionic charge compensation with oxygen vacancies or the adaption of the FERMI level. Since ferroelectricity was initially found in silicon doped  $\text{HfO}_2$ , the doping with silicon plays an important role among the dopants. In the *second* and *third publication* of this dissertation (reference 2 and 3), the doping of  $\text{HfO}_2$  was computationally investigated with

## 5 Summary & Conclusion

DFT. For this, in reference 2, the divalent doping of  $\text{HfO}_2$  with Sr was investigated as an example to first answer two questions: (i) the substitution of the divalent Sr with the tetravalent Hf introduces two excess charges, which must be compensated. What is the energetically preferred compensation mechanism?, and (ii) is this charge compensation mechanism promoting or diminishing the  $p$ - $o$ -phase? To answer these questions, the total energies and formation energies of the possible Sr incorporations and their related defects were computed with DFT. It turned out that Sr incorporates substitutionally without an oxygen vacancy as a result of the formation energy during the manufacturing (i.e. electronic charge compensation) and this substitutional  $\text{Sr}_{\text{Hf}}$  defect promotes the  $p$ - $o$ -phase. After the manufacturing and the change of the oxygen supply, the substitutional defect with oxygen vacancy  $\text{Sr}_{\text{Hf}}\text{V}_{\text{O}}$  is preferred. On the other hand, in reference 3, the incorporation of seven tetravalent dopants (C, Ge, Ti, Sn, Zr, Ce, and Si) in  $\text{HfO}_2$  was explored with a similar result that the substitutional incorporation  $\text{D}_{\text{Hf}}$  (D is the dopant) is preferred as a result of the formation energy, but with a different impact on the energies of the phases. Apart from Si, which is known to strongly favor the  $p$ - $o$ -phase and more the  $t$ -phase, Ce doping turned out to be an interesting dopant with less importance on the  $t$ -phase than Si. Lastly, the geometrical incorporation of the dopants in  $\text{HfO}_2$  was investigated with the objective to find a simple chemical causality between the energetic preference and e.g. the number of bonds or bond distance. However, such a causality could only be found for a small subset of atoms.

The *fourth* publication (reference 4) of this dissertation deals with the pyroelectricity and the storage capacity of silicon doped  $\text{HfO}_2$ . Since the pyroelectricity is strongly connected with the ferroelectricity and silicon is a well-known promoter of the ferroelectricity,  $\text{HfO}_2$  samples with three different silicon concentrations (3.8, 4.3 and 5.6 mol% ) were chosen. First, the pyroelectric coefficient of the samples was measured for two cases: (i) the ferroelectric hysteresis was cycled with an applied electric field, while the sample temperature was changed, and (ii) the sample was not exposed to any external electric field, while the temperature was changed. In the first case, a giant pyroelectric coefficient of up to  $-1300 \mu\text{C}/\text{m}^2\text{K}$  and a HED of  $40 \text{ J}/\text{cm}^3$  could be measured. The pyroelectric coefficient of the second case was only  $-52 \mu\text{C}/\text{m}^2\text{K}$ . The measured huge pyroelectric coefficient is conjectured to arise from a phase transition between the  $t$ - and  $p$ - $o$ -phase, which is initiated by the temperature change. To further study the huge pyroelectric coefficient, SEM measurements of the thin films were conducted with the result that the thin films have a polycrystalline structure with grain radii in the range of 5 nm to 40 nm. Since the stabilization of the  $p$ - $o$ -phase in  $\text{Hf}_{1-x}\text{Zr}_x\text{O}_2$  is believed to arise from the interface energies, which contribute to the Gibbs energy according to the surface area of a grain, every grain of the polycrystalline structure has its own phase transition temperature from the  $t$  to the  $p$ - $o$ -phase (CURIE temperature). By using this connection between the grain radius distribution and the temperature dependent polarization, a grain radii dependent CURIE temperature ( $T_c(r)$ ) could be computed for the samples. Furthermore, it was concluded that (i) the pyroelectric coefficient is caused by the phase transition from the  $t$ -phase, having no intrinsic polarization, to the  $p$ - $o$ -phase, having a maxi-



mum, intrinsic polarization according to the dopant species, (ii) the maximum of the pyroelectric coefficient can be shifted to other temperatures with changing the silicon concentration and (iii) the grain radius distribution adjusts the temperature range of sensitivity. While the last potential of optimization is rather interesting for pyroelectric sensors, the first two are particularly interesting for pyroelectric harvesting applications.



## 6 Outlook

The interface energies in the Gibbs energy model in reference 1 are obtained as fit parameters to experimental data, even though first-principles computations of the interface energies are possible. Typically, three types of interfaces in polycrystalline materials like  $\text{Hf}_{1-x}\text{Zr}_x\text{O}_2$  are conceivable: (i) interfaces between the material and the electrode, (ii) grain boundary interfaces, which are typically incoherent and (iii) domain walls within a grain, with a rather coherent interface between two phases or orientations of one phase. Taking into consideration the seven important crystal phases of  $\text{Hf}_{1-x}\text{Zr}_x\text{O}_2$  and the potential orientations of their surfaces, the three types of interfaces can be constructed in a supercell and computed with DFT. The limiting factor of the supercell calculations is the number of electrons, which is determined by the currently available computation power. To overcome this limitation, DFT computations are normally performed using PBCs. For interface energy calculations, this means that either the calculations must be constructed to sustain the periodicity or surfaces with vacuum must be introduced, which artificially break the PBCs. While in the first case, two equal interfaces in one supercell must be constructed to maintain the periodicity, in the second case, the supercell has only one interface and two surfaces towards the vacuum. In both cases, the cells must be constructed to sustain their stoichiometry (i.e. entities of 1 metal and 2 oxygen) and the symmetry of their surfaces or interfaces. Both limitations can only be maintained for the case of the *c*- and *t*-phase in  $\text{Hf}_{1-x}\text{Zr}_x\text{O}_2$ . A different approach to examine interface energies is to construct a grain-like structure of one crystal phase in the supercell and cover its shell with another phase. In this approach, various orientations of the interfaces are natively present and the value of the resulting interface energy would be a mixture of these. It should be noted that the number of electrons (atoms) in such calculations could be tremendous, which can make the calculations unfeasible.

To retain the advantages of first-principles approaches but resolve the restriction of the number of electrons of DFT, the results of DFT calculations can be adapted and used in *multiscale models*. One approach for this is to reuse the energies and forces of DFT in molecular dynamic (MD) computations by creating potentials which reproduce the DFT findings. Such MD simulations with accurate potentials would allow the investigation of kinetic effects (polarization switching, grain growth, domain wall motion, . . .) of  $\text{Hf}_{1-x}\text{Zr}_x\text{O}_2$  in more detail.

The final step of the manufacturing process of  $\text{Hf}_{1-x}\text{Zr}_x\text{O}_2$  thin films, which exhibit pyroelectricity and ferroelectricity, is an annealing step. The temperature of this anneal must be higher than the crystallization temperature of the participating

## 6 Outlook

atom species, and the annealing time controls the total thermal budget. Park et al.<sup>60</sup> experimentally found that the fraction of the *m*-phase in thin  $\text{Hf}_{0.5}\text{Zr}_{0.5}\text{O}_2$  films increases with higher annealing temperatures. This may suggest that the crystal phases in the thin films are located in shallow valleys with low energy barriers to other phases (“metastable” phase) and that a higher annealing temperature can already trigger the phase transition over the barrier (see also reference 105). A computational model to explore and investigate such transient transitions and grain growing processes of crystal phases is the Kolmogoroff-Johnson-Mehl-Avrami (KJMA) rate model<sup>106</sup>. The KJMA model calculates the fraction of the structural transformation based on a nucleation and crystal growing process, which is determined by a thermodynamic activation barrier. The thermodynamic activation barrier depends on the Gibbs energy, including the bulk (volume) and surface energy. Apart from the temperature, the electric field can induce structural transformations in  $\text{Hf}_{1-x}\text{Zr}_x\text{O}_2$ . Specifically, in the case of  $\text{ZrO}_2$ , when the *t*-phase is closer to the *p-o*-phase than in  $\text{HfO}_2$ <sup>1</sup>, the antiferroelectric-like shape of the hystereses is conjectured to be caused by an electric-field-driven phase transition. It should be noted that the applied electric field, which is required to switch the polarization in the materials system  $\text{Hf}_{1-x}\text{Zr}_x\text{O}_2$ , is close to the breakthrough field and can thus have a significant contribution to the Gibbs energy.

# Acknowledgments

At first, I want to thank my doctoral adviser, *Alfred Kersch*, cordially for the engagement and advice during my doctoral studies. Thank you in particular for the appropriated amount of guidance and motivation during the hard times. Furthermore, I want to thank my second and third doctoral advisers, *Karsten Reuter* and *Andreas Rüdiger*, for giving me the opportunity to work with them and for their advice on scientific and personal questions.

I want to express my special thanks to my colleagues, *Robin Materlik*, *Max Falkowski*, *Andreas Dörfler* and *Mustafa Yusufi* for the countless rational and irrational discussions on diverse topics. Although frequently ended up in a dissent, the discussions were always interesting and productive for me. In addition, I am very grateful to *Uwe Schröder*, *Tony Schenk*, *Ulrich Böttger* and *Sergej Starschich* for the fruitful discussions and helpful comments on my work in the monthly meetings within the DFG (German research foundation) project “Inferox”. Your perspectives were very useful and improved my research significantly.

Moreover, I want to warmly thank *Rampi Ramprasad*, *George Rossetti, Jr.*, *Rohit Batra*, *Deepak Kamal*, and the rest of the research group for the overwhelming six-month stay at the University of Connecticut as a research scholar. It was a great and formative experience for me. Thank you for the warm welcome, respectful interaction, and awesome time.

Furthermore, I would like to thank my mentor, *Andreas Spitzer*, for the interesting and exciting discussion on my doctoral research project. Your industrial perspectives, lateral thoughts, and experiences were a big benefit for my research and character development.

The Technical University of Munich (TUM) and the Munich School of Engineering (MSE) is gratefully acknowledged for granting me a full doctoral scholarship within the TUM Applied Technology Forum to conduct the research necessary for this dissertation. Specifically, I want to thank *Christiane Hamacher* from the MSE graduate school for the uncomplicated communications. Moreover, I want to thank the University of Applied Sciences Munich.

Finally, I would like to thank my *family* and *friends* for their support and motivating words. Love!

Munich, May 2, 2018



# Bibliography

- <sup>1</sup>C. Künneth, R. Materlik, and A. Kersch, “Modeling ferroelectric film properties and size effects from tetragonal interlayer in Hf<sub>1-x</sub>Zr<sub>x</sub>O<sub>2</sub> grains”, *J. Appl. Phys.* **121**, 205304 (2017).
- <sup>2</sup>R. Materlik, C. Künneth, T. Mikolajick, and A. Kersch, “The impact of charge compensated and uncompensated strontium defects on the stabilization of the ferroelectric phase in HfO<sub>2</sub>”, *Appl. Phys. Lett.* **111**, 082902 (2017).
- <sup>3</sup>C. Künneth, R. Materlik, M. Falkowski, and A. Kersch, “Impact of Four-Valent Doping on the Crystallographic Phase Formation for Ferroelectric HfO<sub>2</sub> from First-Principles: Implications for Ferroelectric Memory and Energy-Related Applications”, *ACS Appl. Nano Mater.* **1**, 254–264 (2018).
- <sup>4</sup>M. Hoffmann, U. Schroeder, C. Künneth, A. Kersch, S. Starschich, U. Böttger, and T. Mikolajick, “Ferroelectric phase transitions in nanoscale HfO<sub>2</sub> films enable giant pyroelectric energy conversion and highly efficient supercapacitors”, *Nano Energy* **18**, 154–164 (2015).
- <sup>5</sup>H. Mulaosmanovic, S. Slesazek, J. Ocker, M. Pesic, S. Muller, S. Flachowsky, J. Muller, P. Polakowski, J. Paul, S. Jansen, S. Kolodinski, C. Richter, S. Piontek, T. Schenk, A. Kersch, C. Künneth, R. Van Bentum, U. Schroeder, and T. Mikolajick, “Evidence of single domain switching in hafnium oxide based FeFETs: Enabler for multi-level FeFET memory cells”, in *Tech. dig. - int. electron devices meet. iedm*, Vol. 2016-Febru (Dec. 2015), pp. 26.8.1–26.8.3.
- <sup>6</sup>U. Schroeder, M. Pesic, T. Schenk, H. Mulaosmanovic, S. Slesazek, J. Ocker, C. Richter, E. Yurchuk, K. Khullar, J. Muller, P. Polakowski, E. D. Grimley, J. M. Lebeau, S. Flachowsky, S. Jansen, S. Kolodinski, R. van Bentum, A. Kersch, C. Künneth, and T. Mikolajick, “Impact of field cycling on HfO<sub>2</sub> based non-volatile memory devices”, in *2016 46th eur. solid-state device res. conf.* Vol. 2016-Octob (Sept. 2016), pp. 364–368.
- <sup>7</sup>F. P. G. Fengler, M. Pešić, S. Starschich, T. Schneller, C. Künneth, U. Böttger, H. Mulaosmanovic, T. Schenk, M. H. Park, R. Nigon, P. Mural, T. Mikolajick, and U. Schroeder, “Domain Pinning: Comparison of Hafnia and PZT Based Ferroelectrics”, *Adv. Electron. Mater.* **3**, 1600505 (2017).

## Bibliography

- <sup>8</sup>M. Pešić, C. Künneth, M. Hoffmann, H. Mulaosmanovic, S. Müller, E. T. Breyer, U. Schroeder, A. Kersch, T. Mikolajick, and S. Slesazeck, “A computational study of hafnia-based ferroelectric memories: from ab initio via physical modeling to circuit models of ferroelectric device”, *J. Comput. Electron.* **16**, 1236–1256 (2017).
- <sup>9</sup>R. Materlik, C. Künneth, M. Falkowski, T. Mikolajick, and A. Kersch, “Al-, Y-, and La-doping effects favoring intrinsic and field induced ferroelectricity in HfO<sub>2</sub>: A first principles study”, *J. Appl. Phys.* **123**, 164101 (2018).
- <sup>10</sup>R. Materlik, C. Künneth, and A. Kersch, “The origin of ferroelectricity in Hf<sub>1-x</sub>Zr<sub>x</sub>O<sub>2</sub>: A computational investigation and a surface energy model”, *J. Appl. Phys.* **117**, 134109 (2015).
- <sup>11</sup>T. S. Böске, J. Müller, D. Bräuhaus, U. Schröder, and U. Böttger, “Ferroelectricity in hafnium oxide thin films”, *Appl. Phys. Lett.* **99**, 102903 (2011).
- <sup>12</sup>J. Müller, T. S. Böске, U. Schröder, S. Mueller, D. Bräuhaus, U. Böttger, L. Frey, and T. Mikolajick, “Ferroelectricity in simple binary ZrO<sub>2</sub> and HfO<sub>2</sub>”, *Nano Lett.* **12**, 4318–4323 (2012).
- <sup>13</sup>S. Starschich and U. Böttger, “Doped ZrO<sub>2</sub> for future lead free piezoelectric devices”, *J. Appl. Phys.* **123**, 044101 (2018).
- <sup>14</sup>S. Starschich and U. Boettger, “An extensive study of the influence of dopants on the ferroelectric properties of HfO<sub>2</sub>”, *J. Mater. Chem. C* **5**, 333–338 (2017).
- <sup>15</sup>M. E. Lines and A. M. Glass, *Principles and applications of ferroelectrics and related materials* (Clarendon Press, Oxford, 1977).
- <sup>16</sup>G. D. Wilk, R. M. Wallace, and J. M. Anthony, “High- $\kappa$  gate dielectrics: Current status and materials properties considerations”, *J. Appl. Phys.* **89**, 5243–5275 (2001).
- <sup>17</sup>J. Robertson, “High dielectric constant gate oxides for metal oxide Si transistors”, *Reports Prog. Phys.* **69**, 327–396 (2006).
- <sup>18</sup>H. Zhu, C. Tang, L. R. C. Fonseca, and R. Ramprasad, “Recent progress in ab initio simulations of hafnia-based gate stacks”, *J. Mater. Sci.* **47**, 7399–7416 (2012).
- <sup>19</sup>H. Klapper and T. Hahn, “Point-group symmetry and physical properties of crystals”, in *Int. tables crystallogr.* Vol. A, edited by M. I. Aroyo (International Union of Crystallography, Chester, England, Oct. 2006), pp. 804–808.
- <sup>20</sup>X. Sang, E. D. Grimley, T. Schenk, U. Schroeder, and J. M. Lebeau, “On the structural origins of ferroelectricity in HfO<sub>2</sub> thin films”, *Appl. Phys. Lett.* **106**, 162905 (2015).
- <sup>21</sup>T. D. Huan, V. Sharma, G. A. Rossetti, and R. Ramprasad, “Pathways towards ferroelectricity in hafnia”, *Phys. Rev. B - Condens. Matter Mater. Phys.* **90**, 1–5 (2014).
- <sup>22</sup>L. Zhao, M. Nelson, H. Aldridge, T. Iamsasri, C. M. Fancher, J. S. Forrester, T. Nishida, S. Moghaddam, and J. L. Jones, “Crystal structure of Si-doped HfO<sub>2</sub>”, *J. Appl. Phys.* **115**, 034104 (2014).



- <sup>23</sup>C. M. Fancher, L. Zhao, M. Nelson, L. Bai, G. Shen, and J. L. Jones, “Pressure-induced structures of Si-doped HfO<sub>2</sub>”, *J. Appl. Phys.* **117**, 234102 (2015).
- <sup>24</sup>E. H. Kisi and C. Howard, “Crystal Structures of Zirconia Phases and their Inter-Relation”, *Key Eng. Mater.* **153-154**, 1–36 (1998).
- <sup>25</sup>E. H. Kisi, C. J. Howard, and R. J. Hill, “Crystal Structure of Orthorhombic Zirconia in Partially Stabilized Zirconia”, *J. Am. Ceram. Soc.* **72**, 1757–1760 (1989).
- <sup>26</sup>R. Batra, T. D. Huan, J. L. Jones, G. Rossetti, and R. Ramprasad, “Factors Favoring Ferroelectricity in Hafnia: A First-Principles Computational Study”, *J. Phys. Chem. C* **121**, 4139–4145 (2017).
- <sup>27</sup>O. Ohtaka, H. Fukui, T. Kunisada, T. Fujisawa, K. Funakoshi, W. Utsumi, T. Irifune, K. Kuroda, and T. Kikegawa, “Phase Relations and Volume Changes of Hafnia under High Pressure and High Temperature”, *J. Am. Ceram. Soc.* **84**, 1369–1373 (2004).
- <sup>28</sup>R. Ruh, H. J. Garret, R. F. Domagala, and N. M. Tallan, “The System Zirconia - Hafnia”, *J. Am. Ceram. Soc.* **51**, 23–28 (1968).
- <sup>29</sup>T. Schenk, S. Mueller, U. Schroeder, R. Materlik, A. Kersch, M. Popovici, C. Adelman, S. Van Elshocht, and T. Mikolajick, “Strontium doped hafnium oxide thin films: Wide process window for ferroelectric memories”, in *Eur. solid-state device res. conf.* (Sept. 2013), pp. 260–263.
- <sup>30</sup>C. Richter, T. Schenk, U. Schroeder, and T. Mikolajick, “Film properties of low temperature HfO<sub>2</sub> grown with H<sub>2</sub>O, O<sub>3</sub>, or remote O<sub>2</sub>-plasma”, *J. Vac. Sci. Technol. A Vacuum, Surfaces, Film.* **32**, 01A117 (2014).
- <sup>31</sup>S. Starschich, D. Griesche, T. Schneller, and U. Böttger, “Chemical Solution Deposition of Ferroelectric Hafnium Oxide for Future Lead Free Ferroelectric Devices”, *ECS J. Solid State Sci. Technol.* **4**, P419–P423 (2015).
- <sup>32</sup>S. Starschich, D. Griesche, T. Schneller, R. Waser, and U. Böttger, “Chemical solution deposition of ferroelectric yttrium-doped hafnium oxide films on platinum electrodes”, *Appl. Phys. Lett.* **104**, 202903 (2014).
- <sup>33</sup>A. Wei, C. Chen, L. Tang, K. Zhou, and D. Zhang, “Chemical solution deposition of ferroelectric Sr:HfO<sub>2</sub> film from inorganic salt precursors”, *J. Alloys Compd.* **731**, 546–553 (2018).
- <sup>34</sup>T. Olsen, U. Schröder, S. Müller, A. Krause, D. Martin, A. Singh, J. Müller, M. Geidel, and T. Mikolajick, “Co-sputtering yttrium into hafnium oxide thin films to produce ferroelectric properties”, *Appl. Phys. Lett.* **101** (2012) 10.1063/1.4747209.
- <sup>35</sup>T. Shimizu, K. Katayama, T. Kiguchi, A. Akama, T. J. Konno, and H. Funakubo, “Growth of epitaxial orthorhombic YO<sub>1.5</sub>-substituted HfO<sub>2</sub> thin film”, *Appl. Phys. Lett.* **107**, 032910 (2015).

## Bibliography

- <sup>36</sup>T. Shimizu, K. Katayama, T. Kiguchi, A. Akama, T. J. Konno, O. Sakata, and H. Funakubo, “The demonstration of significant ferroelectricity in epitaxial Y-doped HfO<sub>2</sub> film”, *Sci. Rep.* **6**, 1–8 (2016).
- <sup>37</sup>S. V. Barabash, “Prediction of new metastable HfO<sub>2</sub> phases: toward understanding ferro- and antiferroelectric films”, *J. Comput. Electron.* **16**, 1227–1235 (2017).
- <sup>38</sup>L.-G. Liu, “New high pressure phases of ZrO<sub>2</sub> and HfO<sub>2</sub>”, *J. Phys. Chem. Solids* **41**, 331–334 (1980).
- <sup>39</sup>H. J. Kim, M. H. Park, Y. J. Kim, Y. H. Lee, W. Jeon, T. Gwon, T. Moon, K. D. Kim, and C. S. Hwang, “Grain size engineering for ferroelectric Hf<sub>0.5</sub> Zr<sub>0.5</sub> O<sub>2</sub> films by an insertion of Al<sub>2</sub>O<sub>3</sub> interlayer”, *Appl. Phys. Lett.* **105**, 192903 (2014).
- <sup>40</sup>M. Hyuk Park, H. Joon Kim, Y. Jin Kim, T. Moon, and C. Seong Hwang, “The effects of crystallographic orientation and strain of thin Hf<sub>0.5</sub> Zr<sub>0.5</sub> O<sub>2</sub> film on its ferroelectricity”, *Appl. Phys. Lett.* **104**, 072901 (2014).
- <sup>41</sup>M. Hoffmann, U. Schroeder, T. Schenk, T. Shimizu, H. Funakubo, O. Sakata, D. Pohl, M. Drescher, C. Adelman, R. Materlik, A. Kersch, and T. Mikolajick, “Stabilizing the ferroelectric phase in doped hafnium oxide”, *J. Appl. Phys.* **118**, 072006 (2015).
- <sup>42</sup>E. D. Grimley, T. Schenk, X. Sang, M. Pešić, U. Schroeder, T. Mikolajick, and J. M. LeBeau, “Structural Changes Underlying Field-Cycling Phenomena in Ferroelectric HfO<sub>2</sub> Thin Films”, *Adv. Electron. Mater.* **2**, 1600173 (2016).
- <sup>43</sup>M. Pešić, F. P. G. Fengler, L. Larcher, A. Padovani, T. Schenk, E. D. Grimley, X. Sang, J. M. LeBeau, S. Slesazek, U. Schroeder, and T. Mikolajick, “Physical Mechanisms behind the Field-Cycling Behavior of HfO<sub>2</sub>-Based Ferroelectric Capacitors”, *Adv. Funct. Mater.* **26**, 4601–4612 (2016).
- <sup>44</sup>E. D. Grimley, T. Schenk, T. Mikolajick, U. Schroeder, and J. M. Lebeau, “Atomic Structure of Domain and Interphase Boundaries in Ferroelectric HfO<sub>2</sub>”, *Adv. Mater. Interfaces* **1701258**, 1–9 (2018).
- <sup>45</sup>M. H. Park, Y. H. Lee, H. J. Kim, T. Schenk, W. Lee, K. D. Kim, F. P. G. Fengler, T. Mikolajick, U. Schroeder, and C. S. Hwang, “Surface and grain boundary energy as the key enabler of ferroelectricity in nanoscale hafnia-zirconia: a comparison of model and experiment”, *Nanoscale* **9**, 9973–9986 (2017).
- <sup>46</sup>T. Mikolajick, S. Müller, T. Schenk, E. Yurchuk, S. Slesazek, U. Schröder, S. Flachowsky, R. van Bentum, S. Kolodinski, P. Polakowski, and J. Müller, “Doped Hafnium Oxide – An Enabler for Ferroelectric Field Effect Transistors”, *Adv. Sci. Technol.* **95**, 136–145 (2014).
- <sup>47</sup>S. E. Reyes-Lillo, K. F. Garrity, and K. M. Rabe, “Antiferroelectricity in thin-film ZrO<sub>2</sub> from first principles”, *Phys. Rev. B - Condens. Matter Mater. Phys.* **90**, 140103 (2014).

- <sup>48</sup>Z. Fan, J. Deng, J. Wang, Z. Liu, P. Yang, J. Xiao, X. Yan, Z. Dong, J. Wang, and J. Chen, “Ferroelectricity emerging in strained (111)-textured ZrO<sub>2</sub> thin films”, *Appl. Phys. Lett.* **108**, 012906 (2016).
- <sup>49</sup>D. Zhou, Y. Guan, M. M. Vopson, J. Xu, H. Liang, F. Cao, X. Dong, J. Mueller, T. Schenk, and U. Schroeder, “Electric field and temperature scaling of polarization reversal in silicon doped hafnium oxide ferroelectric thin films”, *Acta Mater.* **99**, 240–246 (2015).
- <sup>50</sup>D. Damjanovic, “Ferroelectric, dielectric and piezoelectric properties of ferroelectric thin films and ceramics”, *Reports Prog. Phys.* **61**, 1267 (1998).
- <sup>51</sup>M. H. Park, H. J. Kim, Y. J. Kim, T. Moon, K. D. Kim, and C. S. Hwang, “Thin Hfx Zr<sub>1-x</sub> O<sub>2</sub> Films: A New Lead-Free System for Electrostatic Supercapacitors with Large Energy Storage Density and Robust Thermal Stability”, *Adv. Energy Mater.* **4**, 1400610 (2014).
- <sup>52</sup>M. H. Park, Y. H. Lee, H. J. Kim, Y. J. Kim, T. Moon, K. D. Kim, J. Müller, A. Kersch, U. Schroeder, T. Mikolajick, and C. S. Hwang, “Ferroelectricity and Antiferroelectricity of Doped Thin HfO<sub>2</sub>-Based Films”, *Adv. Mater.* **27**, 1811–1831 (2015).
- <sup>53</sup>M. H. Park, H. J. Kim, Y. J. Kim, T. Moon, K. D. Kim, and C. S. Hwang, “Toward a multifunctional monolithic device based on pyroelectricity and the electrocaloric effect of thin antiferroelectric HfxZr<sub>1-x</sub>O<sub>2</sub> films”, *Nano Energy* **12**, 131–140 (2015).
- <sup>54</sup>C. Mart, T. Kampfe, S. Zybelle, and W. Weinreich, “Layer thickness scaling and wake-up effect of pyroelectric response in Si-doped HfO<sub>2</sub>”, *Appl. Phys. Lett.* **112**, 052905 (2018).
- <sup>55</sup>R. B. Olsen, J. M. Briscoe, D. A. Bruno, and W. F. Butler, “A pyroelectric energy converter which employs regeneration”, *Ferroelectrics* **38**, 975–978 (1981).
- <sup>56</sup>M. H. Park, H. J. Kim, Y. J. Kim, T. Moon, K. D. Kim, Y. H. Lee, S. D. Hyun, and C. S. Hwang, “Giant Negative Electrocaloric Effects of Hf<sub>0.5</sub>Zr<sub>0.5</sub>O<sub>2</sub> Thin Films”, *Adv. Mater.*, 1–6 (2016).
- <sup>57</sup>M. H. Park, H. J. Kim, Y. J. Kim, Y. H. Lee, T. Moon, K. D. Kim, S. D. Hyun, and C. S. Hwang, “Study on the size effect in Hf<sub>0.5</sub>Zr<sub>0.5</sub>O<sub>2</sub> films thinner than 8 nm before and after wake-up field cycling”, *Appl. Phys. Lett.* **107**, 192907 (2015).
- <sup>58</sup>P. Polakowski and J. Müller, “Ferroelectricity in undoped hafnium oxide”, *Appl. Phys. Lett.* **106**, 232905 (2015).
- <sup>59</sup>S. Starschich, T. Schenk, U. Schroeder, and U. Boettger, “Ferroelectric and piezoelectric properties of Hf<sub>1-x</sub>Zr<sub>x</sub>O<sub>2</sub> and pure ZrO<sub>2</sub> films”, *Appl. Phys. Lett.* **110**, 182905 (2017).
- <sup>60</sup>M. Hyuk Park, H. Joon Kim, Y. Jin Kim, W. Lee, T. Moon, and C. Seong Hwang, “Evolution of phases and ferroelectric properties of thin Hf<sub>0.5</sub>Zr<sub>0.5</sub>O<sub>2</sub> films according to the thickness and annealing temperature”, *Appl. Phys. Lett.* **102**, 242905 (2013).

## Bibliography

- <sup>61</sup>R. Batra, H. D. Tran, and R. Ramprasad, “Stabilization of metastable phases in hafnia owing to surface energy effects”, *Appl. Phys. Lett.* **108**, 172902 (2016).
- <sup>62</sup>S. V. Ushakov, A. Navrotsky, Y. Yang, S. Stemmer, K. Kukli, M. Ritala, M. A. Leskelä, P. Fejes, A. Demkov, C. Wang, B. Y. Nguyen, D. Triyoso, and P. Tobin, “Crystallization in hafnia- and zirconia-based systems”, *Phys. Status Solidi Basic Res.* **241**, 2268–2278 (2004).
- <sup>63</sup>R. C. Garvie, “The occurrence of metastable tetragonal zirconia as a crystallite size effect”, *J. Phys. Chem.* **69**, 1238–1243 (1965).
- <sup>64</sup>M. W. Pitcher, S. V. Ushakov, A. Navrotsky, B. F. Woodfield, G. Li, J. Boerio-Goates, and B. M. Tissue, “Energy crossovers in nanocrystalline zirconia”, *J. Am. Ceram. Soc.* **88**, 160–167 (2005).
- <sup>65</sup>W. Zhou, S. V. Ushakov, T. Wang, J. G. Ekerdt, A. A. Demkov, and A. Navrotsky, “Hafnia: Energetics of thin films and nanoparticles”, *J. Appl. Phys.* **107**, 123514 (2010).
- <sup>66</sup>P. D. Lomenzo, Q. Takmeel, C. Zhou, C. C. Chung, S. Moghaddam, J. L. Jones, and T. Nishida, “Mixed Al and Si doping in ferroelectric HfO<sub>2</sub> thin films”, *Appl. Phys. Lett.* **107**, 3–8 (2015).
- <sup>67</sup>U. Schroeder, E. Yurchuk, J. Müller, D. Martin, T. Schenk, P. Polakowski, C. Adelman, M. I. Popovici, S. V. Kalinin, and T. Mikolajick, “Impact of different dopants on the switching properties of ferroelectric hafniumoxide”, *Jpn. J. Appl. Phys.* **53**, 2–7 (2014).
- <sup>68</sup>C. Richter, T. Schenk, M. H. Park, F. A. Tschardt, E. D. Grimley, J. M. LeBeau, C. Zhou, C. M. Fancher, J. L. Jones, T. Mikolajick, and U. Schroeder, “Si Doped Hafnium Oxide—A “Fragile” Ferroelectric System”, *Adv. Electron. Mater.* **3**, 1–12 (2017).
- <sup>69</sup>A. G. Chernikova, M. G. Kozodaev, D. V. Negrov, E. V. Korostylev, M. H. Park, U. Schroeder, C. S. Hwang, and A. M. Markeev, “Improved ferroelectric switching endurance of La-doped Hf<sub>0.5</sub>Zr<sub>0.5</sub>O<sub>2</sub> thin films”, *ACS Appl. Mater. Interfaces* **10**, acsami.7b15110 (2017).
- <sup>70</sup>J. Müller, U. Schröder, T. S. Böske, I. Müller, U. Böttger, L. Wilde, J. Sundqvist, M. Lemberger, P. Kücher, T. Mikolajick, and L. Frey, “Ferroelectricity in yttrium-doped hafnium oxide”, *J. Appl. Phys.* **110**, 1–6 (2011).
- <sup>71</sup>R. Materlik, C. Kuenneth, M. Falkowski, T. Mikolajick, and A. Kersch, “The Impact of Al-, Y-, and La-doping on Phase Stability Favoring Intrinsic and Field Induced Ferroelectricity in HfO<sub>2</sub>: A First Principles Study”, *J. Appl. Phys.* (2018).
- <sup>72</sup>R. Batra, T. D. Huan, G. A. Rossetti, and R. Ramprasad, “Dopants Promoting Ferroelectricity in Hafnia: Insights from a comprehensive Chemical Space Exploration”, *Chem. Mater.* **29**, 9102–9109 (2017).

- <sup>73</sup>M. H. Park, H. J. Kim, Y. J. Kim, W. Jeon, T. Moon, and C. S. Hwang, “Ferroelectric properties and switching endurance of Hf<sub>0.5</sub> Zr<sub>0.5</sub> O<sub>0.5</sub> films on TiN bottom and TiN or RuO<sub>2</sub> top electrodes”, *Phys. status solidi - Rapid Res. Lett.* **8**, 532–535 (2014).
- <sup>74</sup>M. H. Park, H. J. Kim, Y. J. Kim, Y. H. Lee, T. Moon, K. D. Kim, S. D. Hyun, F. Fengler, U. Schroeder, and C. S. Hwang, “Effect of Zr Content on the Wake-Up Effect in Hf<sub>1-x</sub>Zr<sub>x</sub>O<sub>2</sub> Films”, *ACS Appl. Mater. Interfaces* **8**, 15466–15475 (2016).
- <sup>75</sup>S. Starschich, S. Menzel, and U. Böttger, “Pulse wake-up and breakdown investigation of ferroelectric yttrium doped HfO<sub>2</sub>”, *J. Appl. Phys.* **121** (2017) 10.1063/1.4981893.
- <sup>76</sup>S. Starschich, S. Menzel, and U. Böttger, “Evidence for oxygen vacancies movement during wake-up in ferroelectric hafnium oxide”, *Appl. Phys. Lett.* **108**, 032903 (2016).
- <sup>77</sup>T. Shimizu, T. Yokouchi, T. Oikawa, T. Shiraishi, T. Kiguchi, A. Akama, T. J. Konno, A. Gruverman, and H. Funakubo, “Contribution of oxygen vacancies to the ferroelectric behavior of Hf<sub>0.5</sub> Zr<sub>0.5</sub> O<sub>2</sub> thin films”, *Appl. Phys. Lett.* **106**, 112904 (2015).
- <sup>78</sup>X. Gonze, F. Jollet, F. Abreu Araujo, D. Adams, B. Amadon, T. Applencourt, C. Audouze, J. M. Beuken, J. Bieder, A. Bokhanchuk, E. Bousquet, F. Bruneval, D. Caliste, M. Côté, F. Dahm, F. Da Pieve, M. Delaveau, M. Di Gennaro, B. Dorado, C. Espejo, G. Geneste, L. Genovese, A. Gerossier, M. Giantomassi, Y. Gillet, D. R. Hamann, L. He, G. Jomard, J. Laffamme Janssen, S. Le Roux, A. Levitt, A. Lherbier, F. Liu, I. Lukačević, A. Martin, C. Martins, M. J. Oliveira, S. Poncé, Y. Pouillon, T. Rangel, G. M. Rignanese, A. H. Romero, B. Rousseau, O. Rubel, A. A. Shukri, M. Stankovski, M. Torrent, M. J. Van Setten, B. Van Troeye, M. J. Verstraete, D. Waroquiers, J. Wiktor, B. Xu, A. Zhou, and J. W. Zwanziger, “Recent developments in the ABINIT software package”, *Comput. Phys. Commun.* **205**, 106–131 (2016).
- <sup>79</sup>X. Gonze, B. Amadon, P. M. Anglade, J. M. Beuken, F. Bottin, P. Boulanger, F. Bruneval, D. Caliste, R. Caracas, M. Côté, T. Deutsch, L. Genovese, P. Ghosez, M. Giantomassi, S. Goedecker, D. R. Hamann, P. Hermet, F. Jollet, G. Jomard, S. Leroux, M. Mancini, S. Mazevet, M. J. Oliveira, G. Onida, Y. Pouillon, T. Rangel, G. M. Rignanese, D. Sangalli, R. Shaltaf, M. Torrent, M. J. Verstraete, G. Zerah, and J. W. Zwanziger, “ABINIT: First-principles approach to material and nanosystem properties”, *Comput. Phys. Commun.* **180**, 2582–2615 (2009).
- <sup>80</sup>V. Blum, R. Gehrke, F. Hanke, P. Havu, V. Havu, X. Ren, K. Reuter, and M. Scheffler, “Ab initio molecular simulations with numeric atom-centered orbitals”, *Comput. Phys. Commun.* **180**, 2175–2196 (2009).

## Bibliography

- <sup>81</sup>X. Ren, P. Rinke, V. Blum, J. Wieferink, A. Tkatchenko, A. Sanfilippo, K. Reuter, and M. Scheffler, “Resolution-of-identity approach to Hartree - Fock, hybrid density functionals, RPA, MP2 and GW with numeric atom-centered orbital basis functions”, *New J. Phys.* **14**, 053020 (2012).
- <sup>82</sup>V. Havu, V. Blum, P. Havu, and M. Scheffler, “Efficient O (N) integration for all-electron electronic structure calculation using numeric basis functions”, *J. Comput. Phys.* **228**, 8367–8379 (2009).
- <sup>83</sup>P. Giannozzi, S. Baroni, N. Bonini, M. Calandra, R. Car, C. Cavazzoni, D. Ceresoli, G. L. Chiarotti, M. Cococcioni, I. Dabo, A. Dal Corso, S. De Gironcoli, S. Fabris, G. Fratesi, R. Gebauer, U. Gerstmann, C. Gougoussis, A. Kokalj, M. Lazzeri, L. Martin-Samos, N. Marzari, F. Mauri, R. Mazzarello, S. Paolini, A. Pasquarello, L. Paulatto, C. Sbraccia, S. Scandolo, G. Sclauzero, A. P. Seitsonen, A. Smogunov, P. Umari, and R. M. Wentzcovitch, “QUANTUM ESPRESSO: A modular and open-source software project for quantum simulations of materials”, *J. Phys. Condens. Matter* **21**, 395502 (2009).
- <sup>84</sup>P. Giannozzi, O. Andreussi, T. Brumme, O. Bunau, M. Buongiorno Nardelli, M. Calandra, R. Car, C. Cavazzoni, D. Ceresoli, M. Cococcioni, N. Colonna, I. Carnimeo, A. Dal Corso, S. De Gironcoli, P. Delugas, R. A. Distasio, A. Ferretti, A. Floris, G. Fratesi, G. Fugallo, R. Gebauer, U. Gerstmann, F. Giustino, T. Gorni, J. Jia, M. Kawamura, H. Y. Ko, A. Kokalj, E. Küçükbenli, M. Lazzeri, M. Marsili, N. Marzari, F. Mauri, N. L. Nguyen, H. V. Nguyen, A. Otero-De-La-Roza, L. Paulatto, S. Poncé, D. Rocca, R. Sabatini, B. Santra, M. Schlipf, A. P. Seitsonen, A. Smogunov, I. Timrov, T. Thonhauser, P. Umari, N. Vast, X. Wu, and S. Baroni, “Advanced capabilities for materials modelling with Quantum ESPRESSO”, *J. Phys. Condens. Matter* **29**, 465901 (2017).
- <sup>85</sup>S. J. Clark, M. D. Segall, C. J. Pickard, P. J. Hasnip, M. I. Probert, K. Refson, and M. C. Payne, “First principles methods using CASTEP”, *Zeitschrift für Krist.* **220**, 567–570 (2005).
- <sup>86</sup>K. F. Garrity, J. W. Bennett, K. M. Rabe, and D. Vanderbilt, “Pseudopotentials for high-throughput DFT calculations”, *Comput. Mater. Sci.* **81**, 446–452 (2014).
- <sup>87</sup>A. K. Rajagopal and J. Callaway, “Inhomogeneous electron gas”, *Phys. Rev. B* **7**, 1912–1919 (1973).
- <sup>88</sup>W. Kohn and L. J. Sham, “Self-consistent equations including exchange and correlation effects”, *Phys. Rev.* **140**, A1133–A1138 (1965).
- <sup>89</sup>M. Born and R. Oppenheimer, “Zur Quantentheorie der Molekeln”, *Ann. Phys.* **389**, 457–484 (1927).
- <sup>90</sup>D. M. Ceperley and B. J. Alder, “Ground state of the electron gas by a stochastic method”, *Phys. Rev. Lett.* **45**, 566–569 (1980).
- <sup>91</sup>J. P. Perdew and A. Zunger, “Self-interaction correction to density-functional approximations for many-electron systems”, *Phys. Rev. B* **23**, 5048–5079 (1981).

- <sup>92</sup>J. P. Perdew and Y. Wang, “Accurate and simple analytic representation of the electron-gas correlation energy”, *Phys. Rev. B* **45**, 13244–13249 (1992).
- <sup>93</sup>J. P. Perdew, K. Burke, and M. Ernzerhof, “Generalized gradient approximation made simple”, *Phys. Rev. Lett.* **77**, 3865–3868 (1996).
- <sup>94</sup>J. Heyd, G. E. Scuseria, and M. Ernzerhof, “Hybrid functionals based on a screened Coulomb potential”, *J. Chem. Phys.* **118**, 8207–8215 (2003).
- <sup>95</sup>J. Heyd, G. E. Scuseria, and M. Ernzerhof, “Erratum: Hybrid functionals based on a screened Coulomb potential (Journal of Chemical Physics (2003) 118 (8207))”, *J. Chem. Phys.* **124**, 219906 (2006).
- <sup>96</sup>A. V. Kruckau, O. A. Vydrov, A. F. Izmaylov, and G. E. Scuseria, “Influence of the exchange screening parameter on the performance of screened hybrid functionals”, *J. Chem. Phys.* **125**, 224106 (2006).
- <sup>97</sup>M. Valiev, E. J. Bylaska, N. Govind, K. Kowalski, T. P. Straatsma, H. J. Van Dam, D. Wang, J. Nieplocha, E. Apra, T. L. Windus, and W. A. De Jong, “NWChem: A comprehensive and scalable open-source solution for large scale molecular simulations”, *Comput. Phys. Commun.* **181**, 1477–1489 (2010).
- <sup>98</sup>J. M. Soler, E. Artacho, J. D. Gale, A. García, J. Junquera, P. Ordejón, and D. Sánchez-Portal, “The SIESTA method for ab initio order- N materials”, *J. Phys. Condens. Matter* **2745**, 2745–2779 (2002).
- <sup>99</sup>V. W.-z. Yu, F. Corsetti, A. García, W. P. Huhn, M. Jacquelin, W. Jia, B. Lange, L. Lin, J. Lu, W. Mi, A. Seifitokaldani, Á. Vázquez-Mayagoitia, C. Yang, H. Yang, and V. Blum, “ELSI: A unified software interface for Kohn–Sham electronic structure solvers”, *Comput. Phys. Commun.* **222**, 267–285 (2018).
- <sup>100</sup>K. Parlinski, Z. Li, and Y. Kawazoe, “First-Principles Determination of the Soft Mode in Cubic ZrO<sub>2</sub>”, *Phys. Rev. Lett.* **78**, 4063–4066 (1997).
- <sup>101</sup>X. Gonze, “Perturbation expansion of variational principles at arbitrary order”, *Phys. Rev. A* **52**, 1086–1095 (1995).
- <sup>102</sup>X. Gonze, “Adiabatic density-functional perturbation theory”, *Phys. Rev. A* **52**, 1096–1114 (1995).
- <sup>103</sup>X. Gonze, “Erratum: Adiabatic density-functional perturbation theory”, *Phys. Rev. A* **54**, 4591–4591 (1996).
- <sup>104</sup>X. Gonze, “Dynamical matrices, Born effective charges, dielectric permittivity tensors, and interatomic force constants from density-functional perturbation theory”, *Phys. Rev. B* **55**, 10355–10368 (1997).
- <sup>105</sup>M. H. Park, Y. H. Lee, H. J. Kim, Y. J. Kim, T. Moon, K. D. Kim, S. D. Hyun, T. Mikolajick, U. Schroeder, and C. S. Hwang, “Understanding the formation of the metastable ferroelectric phase in hafnia–zirconia solid solution thin films”, *Nanoscale* **10**, 716–725 (2018).
- <sup>106</sup>M. Avrami, “Kinetics of Phase Change. I General Theory”, *J. Chem. Phys.* **7**, 1103–1112 (1939).





# Appendices



# Modeling Ferroelectric Film Properties and Size Effects from Tetragonal Interlayer in $\text{Hf}_{1-x}\text{Zr}_x\text{O}_2$ Grains

Christopher Künneth, Robin Materlik, and Alfred Kersch

J. Appl. Phys., vol. 121, no. 20, p. 205304, 2017.

DOI: [10.1063/1.4983811](https://doi.org/10.1063/1.4983811)

Reproduced from the Journal of Applied Physics, with the permission of AIP Publishing.

## Modeling ferroelectric film properties and size effects from tetragonal interlayer in $\text{Hf}_{1-x}\text{Zr}_x\text{O}_2$ grains

Christopher Künneth,<sup>a)</sup> Robin Materlik, and Alfred Kersch<sup>b)</sup>

Department of Applied Sciences and Mechatronics, Munich University of Applied Sciences,  
Lothstr. 34, D-80335 Munich, Germany

(Received 17 February 2017; accepted 8 May 2017; published online 24 May 2017)

Size effects from surface or interface energy play a pivotal role in stabilizing the ferroelectric phase in recently discovered thin film Zirconia-Hafnia. However, sufficient quantitative understanding has been lacking due to the interference with the stabilizing effect from dopants. For the important class of undoped  $\text{Hf}_{1-x}\text{Zr}_x\text{O}_2$ , a phase stability model based on free energy from Density functional theory (DFT) and surface energy values adapted to the sparse experimental and theoretical data has been successful to describe key properties of the available thin film data. Since surfaces and interfaces are prone to interference, the predictive capability of the model is surprising and directs to a hitherto undetected, underlying reason. New experimental data hint on the existence of an interlayer on the grain surface fixed in the tetragonal phase possibly shielding from external influence. To explore the consequences of such a mechanism, we develop an interface free energy model to include the fixed interlayer, generalize the grain model to include a grain radius distribution, calculate average polarization and permittivity, and compare the model with available experimental data. Since values for interface energies are sparse or uncertain, we obtain its values from minimizing the least square difference between predicted key parameters to experimental data in a global optimization. Since the detailed values for DFT energies depend on the chosen method, we repeat the search for different computed data sets and come out with quantitatively different but qualitatively consistent values for interface energies. The resulting values are physically very reasonable and the model is able to give qualitative prediction. On the other hand, the optimization reveals that the model is not able to fully capture the experimental data. We discuss possible physical effects and directions of research to possibly close this gap. *Published by AIP Publishing.*

[<http://dx.doi.org/10.1063/1.4983811>]

### I. INTRODUCTION

The discovery of ferroelectricity in  $\text{HfO}_2$  based polycrystalline, thin films in 2011<sup>1</sup> has attracted increasing attention in the research community and industry after its favorable properties have been revealed. In 2012, Müller *et al.*<sup>2</sup> found that the mixture of  $\text{HfO}_2$  with  $\text{ZrO}_2$  ( $\text{Hf}_{1-x}\text{Zr}_x\text{O}_2$ ,  $x = [0, 1]$ ) is ferroelectric with a maximum remanent polarization of around  $17 \mu\text{C cm}^{-2}$  in  $\text{Hf}_{0.5}\text{Zr}_{0.5}\text{O}_2$ . The orthorhombic  $\text{Pca}2_1$  crystallographic phase (f-phase), which was first described by Kisi *et al.*,<sup>3</sup> has been identified as the source of the ferroelectric behavior<sup>1,4,5</sup> but cannot be found under bulk conditions in ceramic  $\text{Hf}_{1-x}\text{Zr}_x\text{O}_2$ . Crystal phases of  $\text{Hf}_{1-x}\text{Zr}_x\text{O}_2$  in a crystalline state are the naturally occurring low energy monoclinic  $\text{P}2_1/c$  (m-phase), the tetragonal  $\text{P}4_2/mnc$  (t-phase), and cubic  $\text{Fm-}3m$  (c-phase) high temperature phases. The f-phase is only preferred under certain conditions for which the film thickness and deposition procedure are of importance.<sup>6</sup>

The thinnest Atomic Layer Deposition (ALD) deposited, polycrystalline  $\text{Hf}_{1-x}\text{Zr}_x\text{O}_2$  films below 6 nm have a large t-phase fraction, films around 10 nm the largest fraction of f-phase and thicker films an increasing m-phase fraction.<sup>6,7</sup> Density functional theory (DFT) calculations for phase stability from several groups<sup>8–10</sup> have consistently reported that

the m-phase has the lowest total energy followed by the f-, t-, and c-phase. A full explanation of the stabilization mechanism of the f-phase for ferroelectric properties in  $\text{Hf}_{1-x}\text{Zr}_x\text{O}_2$  with a thickness dependence of the phase fractions based on DFT total energies is missing so far. Stabilization of an actually energetically less favourable phase in a pure, crystalline state is in principle possible under specific stress conditions which have also been calculated.<sup>8,10,11</sup> Nevertheless, since the required stress values exceed several GPa this mechanism might be considered as not the dominant one. In addition, a combination of strain and electric field has been proposed by the authors of Ref. 12. According to their results, the stabilization requires around  $-2\%$  of strain together with an electric field of  $1.5 \text{ MV cm}^{-1}$  which has to persist at zero bias in a polarization measurement.

The explanation of the stability of the energetically less favourable f-phase with stress or electric field effects, however, does not explain the observed thickness dependence. Comparison of  $\text{Hf}_{1-x}\text{Zr}_x\text{O}_2$  with differently doped, ferroelectric  $\text{HfO}_2$  shows a size effect for the presence of the f-phase,<sup>13</sup> but with a dopant specific thickness dependence. The fact that dopants modify the free energy of the phases<sup>14</sup> suggests a combination of a dopant specific free energy together with a generally present size effect. 3% Gd doped  $\text{HfO}_2$  seems to be sufficient for stabilizing the f-phase without the need for the size effect. For Si as a dopant, a concentration around 3%–6%

<sup>a)</sup>Electronic mail: [kuenneth@hm.edu](mailto:kuenneth@hm.edu)

<sup>b)</sup>Electronic mail: [akersch@hm.edu](mailto:akersch@hm.edu)

is required but in addition a size effect is present limiting the f-phase to films of a thickness below  $\approx 30$  nm. In ALD  $\text{Hf}_{0.5}\text{Zr}_{0.5}\text{O}_2$ , a size effect is again present limiting the ferroelectric properties to a thickness of about 25 nm. The effect of the dopants on the free energy depends on its defect structure and charge compensation which is presently not known. The defect structure might change with field cycling and contribute to or cause a temporal change of the film properties which has been reported as “wake-up.”<sup>15</sup> We will consider these properties as fixed in our investigation in the sense that we fix the total energy.

For optimization of materials for specific industrial applications, it is mandatory to gain a deeper insight into the mechanism of phase stabilization for  $\text{Hf}_{1-x}\text{Zr}_x\text{O}_2$ . In 1965, Garvie<sup>16</sup> showed that nanocrystalline  $\text{ZrO}_2$  transforms from the m- to t-phase for crystallites smaller than 30 nm and proposed excess surface energy for the mechanism which has to be bigger for the m-phase to make such a phase transition energetically favourable. The surface energy of nanocrystalline  $\text{ZrO}_2$  was measured by Pitcher *et al.*<sup>17</sup> and of  $\text{HfO}_2$  by Zhou *et al.*<sup>18</sup> They found the surface energy of the m-phase to be larger than for the t-phase for both  $\text{HfO}_2$  and  $\text{ZrO}_2$ . These surface energies are averages over all surfaces of crystallites in a powder and, moreover, depend on the chemical environment. In DFT calculations, Christensen and Carter<sup>19</sup> calculated surface energies of  $\text{ZrO}_2$  for the t- and m-phase for various low index surfaces and found values between  $2.0 \text{ J m}^{-2}$  and  $2.5 \text{ J m}^{-2}$ . Batra *et al.*<sup>20</sup> calculated surface energies for  $\text{HfO}_2$  for the t-, m-, and f-phase for various surfaces and found values between  $1.0 \text{ J m}^{-2}$  and  $2.7 \text{ J m}^{-2}$ . These calculations showed consistently higher values for the m-phase than t-phase, but gave no clear results regarding the surface energy of the f-phase.

To stabilize the f-phase against the m-phase with surface energy, its value has to be smaller than that for the m-phase. Furthermore, the appearance of the t-phase for small crystallites dictates that the surface energy value of the f-phase is slightly larger than that of the t-phase. For such surface energy values, a window of stability for a certain range of the surface to volume ratio in crystalline grains appears. The authors<sup>10</sup> used the concept of surface energy to build a free energy model with total energies from DFT and surface energies as fit parameters to find the preferred phase for a grain with a given height and radius. They found that the value of the surface energy must be ordered as  $t < f < m$  to be consistent with DFT total energy calculations for the bulk and to lead to the observed size effect. In the work of Garvie,<sup>16</sup> two phases with two different surface energies were addressed. In contrast, the authors<sup>10</sup> used three different surface energies for  $\text{ZrO}_2$  (for  $\text{HfO}_2$ ),  $\tilde{\gamma}_m = 3.0 \text{ J/m}^2$  ( $3.4 \text{ J/m}^2$ ),  $\tilde{\gamma}_f = 2.0 \text{ J/m}^2$  ( $3.15 \text{ J/m}^2$ ),  $\tilde{\gamma}_t = 1.9 \text{ J/m}^2$  ( $3.1 \text{ J/m}^2$ ), and interpolated linearly in  $x$  to obtain values for  $\text{Hf}_{1-x}\text{Zr}_x\text{O}_2$ . With this model, the dominant phases of grains in the available data for thin films could be well described. Furthermore, it was predicted that ultrathin  $\text{HfO}_2$  should be ferroelectric, which was subsequently observed in 6 nm thin films.<sup>7</sup> Another prediction was ferroelectricity in thick, columnar grown, Chemical Solution Deposition (CSD) deposited  $\text{ZrO}_2$  which was confirmed by Starschich *et al.*<sup>21</sup> The success of the simple surface energy

model is surprising and directs actually to a hitherto undetected, underlying reason.

Indeed, it is not clear that the concept of surface energy is appropriate for grains in thin, polycrystalline films without free surfaces but with interfaces towards the neighbour grain and the electrodes. Experimentally, a few interface energies have been obtained for crystalline t- $\text{HfO}_2$  and t- $\text{ZrO}_2$  in contact to  $\text{SiO}_2$  with values of 0.25 and  $0.13 \text{ J m}^{-2}$ , respectively.<sup>22</sup> Such small values indicate a homogeneous (coherent), defect poor interface. It should be expected that the interface energy of an inhomogeneous (incoherent) interface towards a neighbour grain or electrode will have larger values similar to the surface energies. In any case, all three surface energy densities result in an additional grain size dependent energy contribution.

Further investigation of the grain boundaries, however, yielded surprising structural and electrical results. Grimley *et al.*<sup>23</sup> and Pešić *et al.*<sup>15</sup> recorded high-angle annular dark-field scanning transmission electron microscopy (HAADF-STEM) images of Gd doped ferroelectric  $\text{HfO}_2$  thin films and found a t-phase interlayer below the interface to the TiN electrode which is between half and several unit cells of thickness (one unit cell  $\approx 0.5$  nm). Below this interlayer (at the internal interface), the crystallographic structure abruptly changes into an m- or f-phase core region. It was suspected from images before and after electric field cycling that the thickness of the t-phase interlayer was reduced and the phase of the core could have changed in some cases. However, the existence of a t-phase interlayer is not necessarily located at the interface of an electrode material. Previously, Kasatkin *et al.*<sup>24</sup> investigated  $\text{ZrO}_2$  with HRTEM and HREM, respectively, and found a tetragonal interlayer at the boundary of nanocrystalline, monoclinic particles. They furthermore found the internal interface between the interlayer and core to be coherent and could propose a structural model. Kim *et al.*<sup>25</sup> investigated electrically transient effects in capacitance and resistance of  $\text{Hf}_{0.5}\text{Zr}_{0.5}\text{O}_2$  during field cycling and explained their results with a capacitor model containing a core and two interlayers towards the electrodes with the dielectric constant of the t-phase and a thickness of the interlayer around 1 nm slightly decreasing in thickness during field cycling. Finally, Pešić *et al.*<sup>15</sup> used the assumption of a tetragonal interlayer together with a transient oxygen vacancy distribution to model successfully electrical behaviour during field cycling with a TCAD (Technology Computer Aided Design) model.

The purpose of this paper is to improve the previous free energy model<sup>10</sup> with an experimental grain radius distribution instead of only a fixed grain radius. For this reason, the resulting film properties are phase mixtures which can be compared with experimental data. A further new model feature is to use an interlayer and coherent interface energy model, which is suggested by experimental observations and is used in the evaluation of electrical data and electrical simulation, instead of a surface energy model. Irrespective of the interpretation of the surface energy related data, these values are treated as essentially unknown parameter and are fitted to available data. The resulting optimal values then prove the feasibility of the model as well its limitation. Finally, this procedure is repeated with different data sets of

DFT total energies since there is no stringent criterion to prefer the one above the other.

## II. MATERIALS AND METHODS

The free energy model in this publication is based on a thermodynamic energy functional for a formula unit (f.u.) of a grain in a certain phase  $\phi \in \{m, t, f\}$

$$F_\phi = U_\phi + U_{\phi,0}(T) - TS_\phi + \Gamma_\phi + C_t, \quad (1)$$

with  $U_\phi$  the total energy from the core phase,  $U_{\phi,0}(T)$  the total energy contribution from vibrational modes,  $T$  the temperature, and  $S_\phi$  the vibrational entropy.<sup>26</sup>  $\Gamma_\phi$  is the internal interface energy between the t-phase interlayer and the core for a formula unit, and  $C_t$  is a constant containing the bulk and external interface energy of the tetragonal interlayer.  $\Gamma_\phi$  is calculated assuming cylindrical grains

$$\Gamma_\phi = \frac{2\pi(\tilde{r}^2 + \tilde{r}\tilde{d})V_0}{\pi\tilde{r}^2\tilde{d}} \tilde{\gamma}_{\phi t}$$

with  $\tilde{\gamma}_{\phi t}$  the internal interface energy of phase  $\phi$ ,  $\tilde{r}$  the grain core radius,  $\tilde{d}$  the height of the grain core, and  $V_0$  the volume of a formula unit. The temperature  $T$  is fixed to 300 K.

DFT calculations in this publication are carried out with the plane-wave code ABINIT<sup>27–29</sup> and the all-electron code FHI-Aims (FHIA).<sup>30</sup> Two different kinds of pseudopotential (PP) libraries are used in ABINIT to calculate the total energy  $U_\phi$ , the vibrational entropy  $S_\phi$ , the vibrational contribution to the total energy  $U_{\phi,0}(T)$ , and the volume of a formula unit  $V_0$ . The first library is self-made norm conserving PP's (SM-LDA) detailed in Ref. 10 and the second is designed for highly throughput calculations (GBRV-LDA) detailed in Ref. 31. Both are using the local-density approximation (LDA) and the later one uses the PAW formalism. FHI-Aims uses numeric atom-centered basis functions for all electrons with different default settings for each species named tiers. The total energies, the vibrational contributions, and volumes were calculated with the settings tight and tier 2 in the local-density (FHIA-LDA) and generalized-gradient approximation (FHIA-GGA). Vibrational contributions with ABINIT were carried out by DFPT using the ABINIT utility ANADDB and with FHI-Aims by the utility Phonopy.<sup>32</sup>

The DFT calculations of the crystal phases were carried out in 12 atomic unit cells with the k-points sampled by the Monkhorst–Pack<sup>33</sup> with an  $8 \times 8 \times 8$  grid. The convergence in ABINIT was reached at a plane wave cut off of 816 and 490 eV (PAW cut off 599 eV) for SM-LDA and GBRV-LDA, respectively. The forces during cell optimization were carefully converged up to  $5 \times 10^{-5} \text{ eV } \text{\AA}^{-1}$  for all calculations. The vibrational contributions were calculated with a  $2 \times 2 \times 2$  q-point grid in ANADDB with DFPT and a  $2 \times 2 \times 2$  supercell in FHI-AIMS with the finite displacement method where the forces are converged up to  $5 \times 10^{-5} \text{ eV } \text{\AA}^{-1}$  for both cases.

The preferred phase  $\phi$  as a function  $\Phi$  of a grain with a given radius  $r$  and height  $d$  is obtained by calculating  $F_\phi$  with Eq. (1) for all phases and choosing the energetically most favourable as

$$\Phi(r, d, x) = \min_{\phi \in \{m, f, t\}} F_\phi(r, d, x). \quad (2)$$

For this reason, the DFT data were implemented in a Python script where missing values between  $\text{HfO}_2$  to  $\text{Hf}_{0.5}\text{Zr}_{0.5}\text{O}_2$  and  $\text{ZrO}_2$  to  $\text{Hf}_{0.5}\text{Zr}_{0.5}\text{O}_2$  are linearly interpolated.

The difference of the interface energy model to the previous surface energy model of Ref. 10 is merely a matter of physical interpretation instead of numerical results. Since the t-phase interlayer of thickness  $\delta = 1 \text{ nm}$  has a fixed energy contribution for the same grain geometry, only the interface energy and the core of the grains matter for the optimization. The grain core radius  $\tilde{r}$  and core thickness  $\tilde{d}$  can be obtained from the grain radius  $r$  and thickness  $d$  as

$$\tilde{d} = d - 2\delta \quad \text{and} \quad \tilde{r} = r - \delta.$$

The internal interface energies  $\tilde{\gamma}_{\phi t}$  are obtained from the previous surface energies of Ref. 10  $\gamma_\phi$  as

$$\tilde{\gamma}_{mt} = \gamma_m - \gamma_t, \quad \tilde{\gamma}_{ft} = \gamma_f - \gamma_t \quad \text{and} \quad \tilde{\gamma}_{tt} = 0.$$

The interface free energy model gives exactly the same optimization results as the surface free energy model for a vanishing interlayer thickness  $\delta$ . A schematic representation of the interfaces in the grains with different radii can be found in Fig. 1.

The material properties of individual grains are difficult to assess with experiments. Since most experimental results like XRD spectra or capacitance measurements contain values averaged over many grains of different radii and orientation in the film of thickness  $d$ , we generalize the interface free energy model to give results for a specific grain radius distribution  $f_{\alpha,\beta}(r, d, x)$  (see below). First, the volume fraction for each phase is calculated for a specific grain radius distribution by solving Eq. (2) for a grid consisting of a radius space and  $x$  in  $\text{Hf}_{1-x}\text{Zr}_x\text{O}_2$  space. For this purpose, the grain radius distribution is weighted with  $2\pi rd$  to obtain the volume distribution assuming that the grains are cylindrical and grow from the bottom to the top electrode. Second, the remanent polarization  $\bar{P}_r$  and permittivity  $\bar{k}$  are calculated by taking the value  $\hat{P}_r(\Phi(r, d, x))$  and  $k(\Phi(r, d, x))$  and average these properties with a volumetric weight

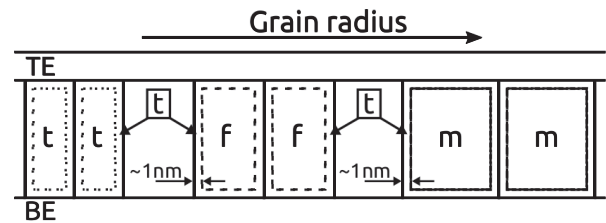


FIG. 1. Columnar grains of three different radii and core phases are illustrated. The phase of the core region depends on composition  $x$  in  $\text{Hf}_{1-x}\text{Zr}_x\text{O}_2$  and the grain radius. The interlayer is located between the grain boundary (continuous lines) and the core interface (three different dashed lines). The interlayer is always in the t-phase and has a thickness of 1 nm for all radii. The different styles of dashed lines indicate different values of coherent interface energy. TE means top electrode and BE bottom electrode.

$$\begin{aligned}\overline{k(d,x)} &= \int_0^\infty 2\pi r d \cdot f_{\alpha,\beta}(r,d,x) k(\Phi(r,d,x)) dr, \\ \overline{P_r(d,x)} &= \int_0^\infty 2\pi r d \cdot f_{\alpha,\beta}(r,d,x) \hat{P}_r(\Phi(r,d,x)) dr.\end{aligned}\quad (3)$$

The dielectric permittivity  $k$  is calculated by a capacitor model where the value of the t-phase is set to experimental values since the DFT results depend too much on the chosen functional.<sup>34</sup> The remaining dielectric permittivities for the m- and f-phase are taken from DFT results of the SM-LDA calculations. The maximum, isotropic averaged polarization  $\hat{P}_r$  is obtained as

$$\hat{P}_r = \frac{1}{4\pi} \int_0^{2\pi} \int_0^{\pi/2} (P_{\text{calc}} \sin \theta) d \cos \theta d\varphi = P_{\text{calc}} \frac{\pi}{8}. \quad (4)$$

Values for  $\hat{P}_r$  and  $k$  are linearly interpolated for HfO<sub>2</sub> to Hf<sub>0.5</sub>Zr<sub>0.5</sub>O<sub>2</sub> and ZrO<sub>2</sub> to Hf<sub>0.5</sub>Zr<sub>0.5</sub>O<sub>2</sub>. A summary of the parameters used in this publication can be found in Table I.

The grain radius distribution of polycrystalline Hf<sub>1-x</sub>Zr<sub>x</sub>O<sub>2</sub> depends on several process conditions of the thin film such as thickness, Zr concentration, or dopant concentration. Hoffmann *et al.*<sup>36</sup> proposed that the grain radius distribution of silicon doped HfO<sub>2</sub> deposited by ALD follows an incomplete gamma function with a constant shape parameter  $s$  for different silicon concentrations. Park *et al.*<sup>37</sup> determined the grain radius distribution from SEM pictures for  $x=0, 0.19, 0.43, 0.70$ , and 1 in Hf<sub>1-x</sub>Zr<sub>x</sub>O<sub>2</sub> and 14.2, 19.2, 24.2, and 29.2 nm of thickness. They found the thickness dependence of the grain radius distribution to decrease from HfO<sub>2</sub> to ZrO<sub>2</sub> and nearly disappear for pure ZrO<sub>2</sub>. Furthermore, Kim *et al.*<sup>38</sup> showed that films deposited by ALD increase the grain radius with the thickness of the film for Hf<sub>0.5</sub>Zr<sub>0.5</sub>O<sub>2</sub>. All publications reveal a similar behavior of the grain radius distribution to change with dopant or rather Zr concentration and thickness. For the implementation of a continuous distribution in Eq. (3), the raw data of Park *et al.*<sup>37</sup> are fitted to the probability density function (pdf) of the beta distribution

$$\begin{aligned}f_{\alpha,\beta}(r,d,x) &= \frac{\Gamma(\alpha+\beta)}{\Gamma(\alpha)\Gamma(\beta)} \cdot \frac{1}{2g(x,d)} \cdot \left(\frac{r}{2g(x,d)}\right)^{\alpha-1} \\ &\times \left(1 - \frac{r}{2g(x,d)}\right)^{\beta-1},\end{aligned}\quad (5)$$

where  $\alpha$  and  $\beta$  are shape parameters and  $\Gamma$  is the gamma function. The shape parameters are found to best match the data from Park *et al.* for  $\alpha = \beta = 3$  by manual adjustment.

TABLE I. Dielectric permittivity  $k$  and isotropic averaged polarization  $\hat{P}_r$  from Eq. (4) used in the interface free energy model.

	$k$			$\hat{P}_r$ ( $\mu\text{C cm}^{-2}$ )	$P_{\text{calc}}$ ( $\mu\text{C cm}^{-2}$ )
	m <sup>a</sup>	t <sup>a</sup>	t <sup>b</sup>		
HfO <sub>2</sub>	22	27	40	20	51
Hf <sub>0.5</sub> Zr <sub>0.5</sub> O <sub>2</sub>	24	29	42	21	54
ZrO <sub>2</sub>	26	31	44	23	58

<sup>a</sup>Calculated with SM-LDA library.

<sup>b</sup>Values from experiments.<sup>35</sup>

By introducing the scale function  $g(x, d)$  in Eq. (5) with units of nm, the beta pdf is adapted to the grain radius range. Since the experimental data clearly demonstrate a thickness and concentration dependency, the phenomenological scale function is

$$g(x, d) = d \cdot \frac{7}{10} (1-x) + 18\pi x \arctan\left(\frac{d}{10}\right). \quad (6)$$

The first term of Eq. (6) constitutes the thickness dependence of the experimental data for low Zr content and due to the second term, the thickness dependence for Zr-rich Hf<sub>1-x</sub>Zr<sub>x</sub>O<sub>2</sub> is small.  $g(x, d)$  was determined by manual adjustment to the experimental data and is illustrated for different thicknesses and Zr concentrations in Fig. S1 in the [supplementary material](#).

Altogether there are  $N$  experimental data points with  $i=1, \dots, N$  for films of thickness  $d_i$  with average remanent polarization  $\bar{P}_{r,i}$  and an average permittivity  $\bar{k}_i$ . The cost function for the optimization contains the total energy values for the crystal phases and other values like vibrational contribution, polarization, and permittivity, denoted with  $\vec{U}$ , which are kept fixed. Furthermore, interface energy parameters  $\vec{\gamma} = \{\tilde{\gamma}_{\text{mt}}^{\text{HfO}_2}, \tilde{\gamma}_{\text{ft}}^{\text{HfO}_2}, \tilde{\gamma}_{\text{mt}}^{\text{ZrO}_2}, \tilde{\gamma}_{\text{ft}}^{\text{ZrO}_2}\}$  are kept variable with linearly interpolated values for intermediate compositions. The cost function for the optimization problem is finally given as a least square difference between the model and experimental data

$$\begin{aligned}\mathcal{E}[\vec{\gamma}] &= \sum_{i=1,N} \left[ \left( \overline{P_r(d,x)}[\vec{\gamma}, \vec{U}] - P_{r,i} \right)^2 \right. \\ &\quad \left. + \left( \overline{k(d,x)}[\vec{\gamma}, \vec{U}] - k_i \right)^2 \right].\end{aligned}\quad (7)$$

All the formulas and DFT values of the different PP's and basis functions are implemented in a Python program. The global minimum is searched with a Basin-hopping stochastic algorithm<sup>39</sup> implemented in SciPy (Python).

### III. RESULTS AND DISCUSSION

Basis of our investigation is the calculated total and free energy differences of the crystal phases relative to the m-phase in Fig. 2. Although there is some theoretical uncertainty from DFT, a common result is that the energy differences are significantly larger on the Hf-rich side than on the Zr-rich side. Furthermore, all total energy differences are higher for GGA than for LDA which is a general trend for Hf<sub>1-x</sub>Zr<sub>x</sub>O<sub>2</sub> compounds.<sup>10,40</sup> The LDA results for a ZrO<sub>2</sub> phase are very similar and the maximum discrepancy is approximately 8%. In contrast, the maximum discrepancy of the LDA results for a HfO<sub>2</sub> phase is approximately 25%. This mirrors the well known difficulties to obtain reliable results from DFT for Hf-rich compounds. The dependencies on the Zr content  $x$  of the total energy difference as well as the temperature dependent entropy contribution turn out to be almost linear in all computations which expresses the very good solubility of ZrO<sub>2</sub> in HfO<sub>2</sub> and vice versa. The difference between the t- and f-phase energies reduces almost

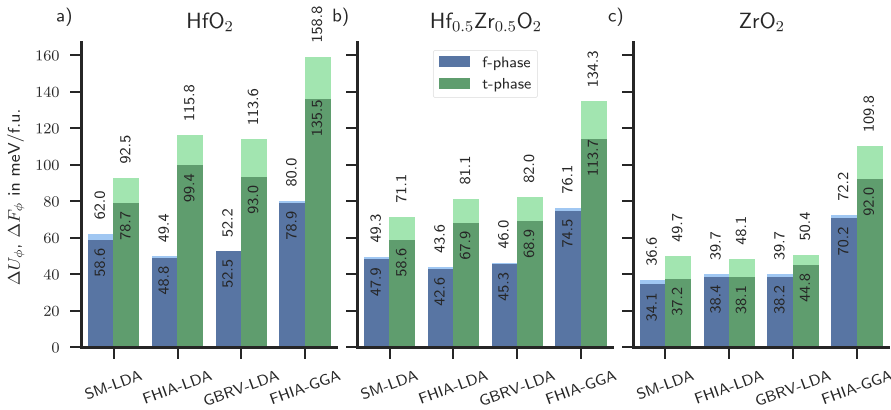


FIG. 2. The full height of the bars indicate the total energy differences  $\Delta U_\phi$  to the m-phase for ZrO<sub>2</sub>, Hf<sub>0.5</sub>Zr<sub>0.5</sub>O<sub>2</sub> and HfO<sub>2</sub> for different basis sets and PP's from DFT calculations. The values on the dark bars show the free energy difference  $\Delta F_\phi = \Delta U_\phi + \Delta U_{\phi,0}(T) - T\Delta S_\phi$  for 300 K to the m-phase.

linearly from HfO<sub>2</sub> with a value of about 50 meV/f.u. to ZrO<sub>2</sub> with a value of about 10 meV/f.u. The vibrational contribution is always higher for the t-phase than for the other phases, implying the temperature driven transition to t-phase for increasing temperatures, and leads to an almost alignment of the t- and f-phase for pure ZrO<sub>2</sub> for 300 K. The vibrational contribution shows a linear dependence on composition like the total energy.

Figure 3 schematically depicts the combination of the composition and grain radius dependent phase diagram generated from the interface model with the grain radius distribution for two different thicknesses of SM-LDA (figures for the other libraries can be found in the [supplementary material](#) Figs. S2–S4). (a) and (c) of Fig. 3 are for 9 nm and (b) and (d) for 6 nm film thickness. The grain radius distribution in a) is depicted for Hf<sub>0.5</sub>Zr<sub>0.5</sub>O<sub>2</sub> and in b) for pure ZrO<sub>2</sub> as indicated with the crosses. By comparing Figs. 3(c) and 3(d), it can be seen that for decreasing film thickness pure, ferroelectric ZrO<sub>2</sub> becomes more unlikely. The grain radius distribution for 6 nm and pure HfO<sub>2</sub> is significantly broader than

for 9 nm and Hf<sub>0.5</sub>Zr<sub>0.5</sub>O<sub>2</sub>. The different grain radius distributions for  $x$  in Hf<sub>1-x</sub>Zr<sub>x</sub>O<sub>2</sub> can be attributed to a different grain growing process which arise from different crystallization temperatures of HfO<sub>2</sub> and ZrO<sub>2</sub>.<sup>22</sup>

Müller *et al.*<sup>2</sup> and Park *et al.*<sup>6</sup> experimentally found a very small m-phase fraction for Hf<sub>0.5</sub>Zr<sub>0.5</sub>O<sub>2</sub> and a thickness of 9 and 10 nm, respectively. In Fig. 3(c), no m-phase remains which agrees well with the experimental data. In addition, all grains in the film from 1 nm to 8 nm radius are either in the t-phase with 39.8% or in the f-phase with 60.2%.

We think that presently the surface or interface energy densities—coherent or incoherent—cannot be calculated with sufficient accuracy. We, therefore, treat them as fit parameters. Optimization of Eq. (7) was performed with the Basin-hopping algorithm for the different libraries SM-LDA, FHIA-LDA, GBRV-LDA, and FHIA-GGA where the values of the resulting coherent interface energies  $\bar{\gamma}$  are documented in Table II and linearly interpolated from HfO<sub>2</sub> to Hf<sub>0.5</sub>Zr<sub>0.5</sub>O<sub>2</sub> and ZrO<sub>2</sub> to Hf<sub>0.5</sub>Zr<sub>0.5</sub>O<sub>2</sub>. This seems likely since the other energy contributions are also mostly linear dependent. As experimental

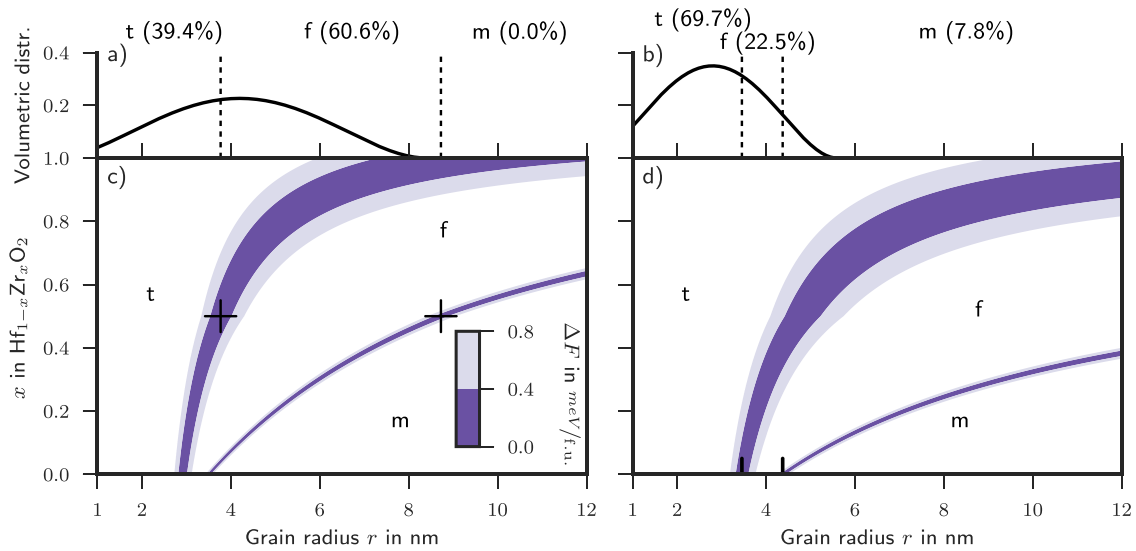


FIG. 3. (a) and (b) shows the grain radius distribution for 9 and 6 nm which correspond to experimental data from Müller *et al.*<sup>2</sup> and Polakowski and Müller.<sup>7</sup> respectively. (c) and (d) shows the associated phase map produced with Eq. (1) and SM-LDA. t, f, and m divided by the purple lines in (c) and (d) indicate the preferred phase for a given radius and Zr concentration. The purple shaded lines indicate the energy difference between the adjacent phases. Since the grain radius distribution is thickness and Zr concentration dependent, the distributions in (a) and (b) are depicted for the associated ZrO<sub>2</sub> concentration of the cross in (c) and (d) which is Hf<sub>0.5</sub>Zr<sub>0.5</sub>O<sub>2</sub> and pure HfO<sub>2</sub>, respectively. t, f, and m (divided by the black dashed line) in (a) and (b) indicate the phase of the partitioned grain radius distribution. The values in parentheses show the percentage of the phase.



TABLE II. Coherent interface energies in  $\text{mJ m}^{-2}$  resulting from optimization to experimental data.

	SM-LDA		FHIA-LDA		GBRV-LDA		FHIA-GGA	
	$\tilde{\gamma}_{m,t}$	$\tilde{\gamma}_{f,t}$	$\tilde{\gamma}_{m,t}$	$\tilde{\gamma}_{f,t}$	$\tilde{\gamma}_{m,t}$	$\tilde{\gamma}_{f,t}$	$\tilde{\gamma}_{m,t}$	$\tilde{\gamma}_{f,t}$
HfO <sub>2</sub>	174	36	106	10	210	77	312	109
ZrO <sub>2</sub>	490	21	403	10	555	49	890	113
$\mathcal{E}^a$	1		2.8		1.3		1.2	

<sup>a</sup> $\mathcal{E}$  of Eq. (7) after optimization. Values are relative to SM-LDA.

data,  $P_r$ , and  $k$  values are used from the Refs. 2 and 7. The optimized coherent interface energies are in the expected order of magnitude<sup>22</sup> and the difference between the t- and f-phase energies is in the order of one magnitude. The FHIA-GGA energies are higher consistent with the total energy differences in Fig. 2. The value of the cost function  $\mathcal{E}$  is normalized to the SM-LDA library since it has the closest value.

Since the cost function value is a measure of the quality of the optimization, the best result could be obtained with the SM-LDA and the worst with the FHIA-LDA library. To energetically stabilize the f-phase at all the interface energies of the m-phase must be larger than from the f-phase since under normal condition the m-phase is always stable. Therefore, the order of magnitude difference in  $\mathcal{E}$  of m- and f-phase ensures that the f-phase can be energetically preferred. However, the t-phase in Fig. 2(c) of the FHIA-LDA library for 300 K is already lower than the f-phase. This means that a stabilization of the f-phase for pure ZrO<sub>2</sub> is only possible for either lower temperatures or a negative interface energy. Since both changes are not allowed in the optimization process, the cost function value of the FHIA-LDA is significantly higher than the others. Furthermore, since no optimization on the ZrO<sub>2</sub> side can be performed the values of the interface energies for the f-phase are both  $10 \text{ mJ m}^{-2}$ .

To stabilize the f-phase in polycrystalline films, it is sufficient that the energy surface density is largest for the m-phase. Since at room temperature the free energy of the f-phase is below the t-phase (except for FHIA-LDA), the size dependent contribution for the f-phase must be larger than for the t-phase otherwise the t-phase would prevail in thick films. In the Hf-rich material, the total contribution has to be relatively large to overcome the large free energy difference requiring the surface to volume ratio of small grains of a few nm present in thin films. In Hf<sub>0.5</sub>Zr<sub>0.5</sub>O<sub>2</sub>, the required contribution is created from grains of the size of 10 nm–20 nm thick films. Polycrystalline Hf<sub>0.5</sub>Zr<sub>0.5</sub>O<sub>2</sub> films thinner than about 5 nm should be the t-phase. In the Zr-rich material with a small free energy difference, the contribution must be small and may be created from large grains present in thick films. Small grains should be the t-phase and very large grains m-phase.

The purple shaded lines in Fig. 3 show the total energy difference between the adjacent phases of a grain and give the energy necessary to transform between phases. For Zr-rich mixtures about  $x=0.75$  in Hf<sub>1-x</sub>Zr<sub>x</sub>O<sub>2</sub>, films of about 9 nm thickness contain many grains close to the phase boundary between the t-phase and f-phase. In this region,

phase transitions are easily induced by temperature, stress, or electric field. Furthermore, for increasing Zr content the shaded lines at the phase boundary of the t- and f-phase become wider and more grains are involved in a phase transition. Concerning the electric field contribution, this agrees with Müller *et al.*<sup>2</sup> where Zr-rich HfO<sub>2</sub> shows anti-ferroelectric behavior which can be also attributed to electric field induced ferroelectricity.<sup>8</sup> In the shallow energy landscape of these films, additional effects affecting phase stability should become visible more easily than for other thickness and composition.

Figure 4 depicts the dielectric permittivity of the experimental data and model results. All DFT calculations reveal almost equal results which indicates equal phase fractions. Besides an offset which may arise due to the uncertainties of the DFT results for the  $k$ , the trend for 9 nm film thickness is in good agreement.

Besides a general consistency of the model with the data, discrepancies become visible between calculated and measured polarizations in Fig. 5. The data seem to show a further stabilization mechanism around Hf<sub>0.5</sub>Zr<sub>0.5</sub>O<sub>2</sub> which the model cannot reproduce. The data indicate some nonlinear dependence on the composition which is missing. It has to be added that energetic effects of about 5 meV/f.u. may significantly change Fig. 3 especially in the shallow regions.

One possible source of a nonlinearity may come from the grain radius. Although Zr-rich ALD films lead to nearly crystalline as deposited films in contrast to nearly amorphous as deposited Hf-rich films, the subsequent annealing leads to complete crystallization and fixes the grain radius distribution. In the model, the variation of the grain radius distribution with composition and thickness found experimentally has been taken into account. Such a variation introduced indeed a nonlinearity. However, the used data show only a moderate variation of the size distribution.

Shiraishi *et al.*<sup>41</sup> discussed the importance of in-plane stress for the polarization in Hf<sub>0.5</sub>Zr<sub>0.5</sub>O<sub>2</sub> and found that the polarization increases for increasing tensile strain with the maximum at 0.5%. Therefore, a possible composition dependent film stress leading to energetic effects of a few meV/f.u. cannot be excluded. A possible built-in electrical field could lead to a nonlinear effect since built-in electrical fields

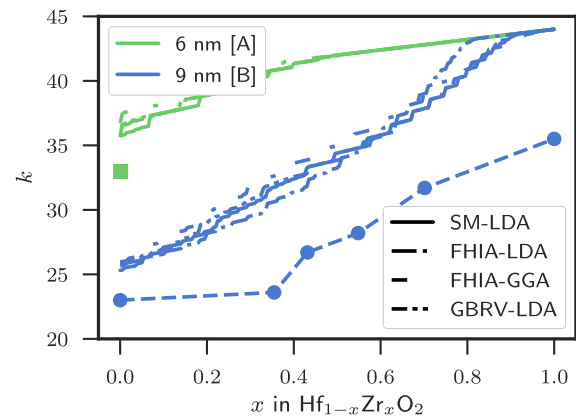


FIG. 4. The dielectric permittivity for Hf<sub>1-x</sub>Zr<sub>x</sub>O<sub>2</sub> for 6 and 9 nm. The symbols of color [A] correspond to Ref. 7 and [B] to Ref. 2.

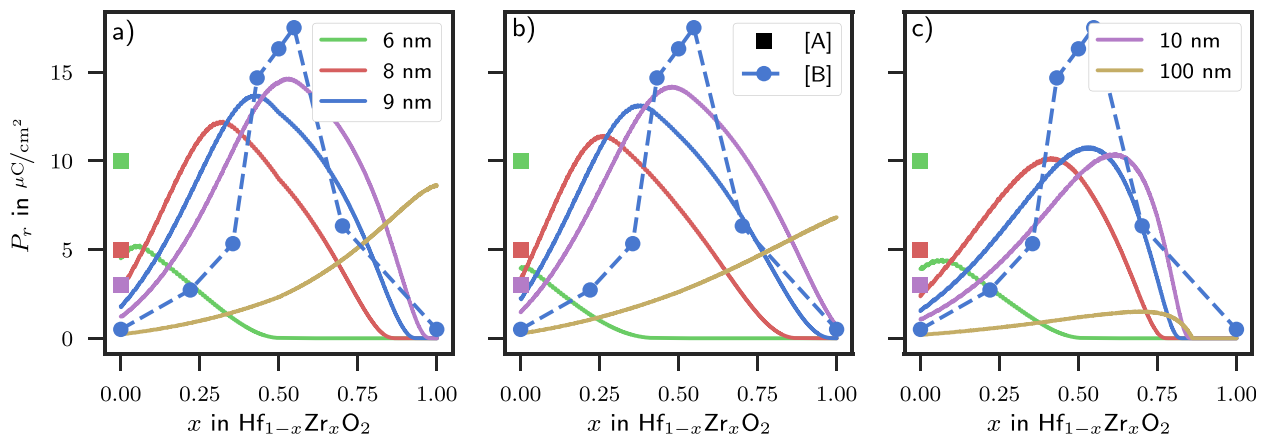


FIG. 5. The remanent polarization  $P_r$ , resulting from optimization. Symbols indicate experimental data, where [A] is taken from Ref. 7 and [B] from Ref. 2, and continuous lines results from the interface energy model. Furthermore, (a) is for SM-LDA, (b) for FHIA-GGA, and (c) for FHIA-LDA.

mostly affect the phase stability in the shallow energy region of Fig. 3 on the Zr-rich side. The question of different surface energies compared to internal surface energies has already been addressed. However, only an effect depending non linearly on composition would add a new feature to the model with a potentially better fit to the data.

Finally, inhomogeneities (e.g., islands or exclaves) of the film composition may affect the phase stability. Although the solubility of Zr and Hf is very good and spontaneous separation processes seem unlikely, the ALD manufacturing method introduces a stoichiometric inhomogeneity for Zr- and Hf-poor films. This has not been systematically investigated, but could be researched experimentally by comparing ALD films with Hf and Zr layers with CSD films containing supposedly perfect mixtures of Hf and Zr.

#### IV. CONCLUSION

In conclusion, a free energy model for polarization and dielectric constant of ALD deposited, polycrystalline  $\text{Hf}_{1-x}\text{Zr}_x\text{O}_2$  was investigated based on data calculated from DFT and on phenomenological coherent interface energy data obtained from a fit to data following an optimization scheme. The calculated volumetric energy data are generated with four different DFT methods and give insight into the uncertainty on the theory side. A common result is the linear dependence on composition comprising the very good solubility of the metal ions and that the energy landscape for the Zr-rich mixtures is very shallow compared to the Hf-rich compounds. The fitted surface related energy data may be interpreted as coherent interface energy between grain cores and surface interlayer and render the picture obtained from several experimental observations consistent from the thermodynamic point of view. The fit based on results from all four different methods gives qualitatively a first order model for film properties. On the other hand, the optimization reveals that the mathematical structure of the composition and size dependence of the model is insufficient and needs some nonlinear physical second order effect to better adapt to the data. Possible directions to investigate in future research are possible stoichiometric inhomogeneities from the deposition procedure, composition dependent stress and

internal electric fields. Furthermore, a question is why the grain surface has a tendency to acquire the t-phase.

#### SUPPLEMENTARY MATERIAL

See [supplementary material](#) for the grain radius distributions and Fig. 3 plotted for other libraries.

#### ACKNOWLEDGMENTS

The author wants to thank U. Schröder, T. Schenk, Min Hyuk Park from NamLab/SNU, and U. Böttger and S. Starschich from RWTH Aachen for discussions. The German Research Foundation (Deutsche Forschungsgemeinschaft) is acknowledged for funding this research in the frame of the project “Inferox” (Project No. MI 1247/11–1). The authors gratefully acknowledge the Gauss Centre for Supercomputing e.V. ([www.gauss-centre.eu](http://www.gauss-centre.eu)) for funding this project by providing computing time on the GCS Supercomputer SuperMUC at Leibniz Supercomputing Center (LRZ, [www.lrz.de](http://www.lrz.de)).

- <sup>1</sup>T. S. Böske, J. Müller, D. Bräuhaus, U. Schröder, and U. Böttger, “Ferroelectricity in hafnium oxide thin films,” *Appl. Phys. Lett.* **99**, 102903 (2011).
- <sup>2</sup>J. Müller, T. S. Böske, U. Schröder, S. Mueller, D. Bräuhaus, U. Böttger, L. Frey, and T. Mikolajick, “Ferroelectricity in Simple Binary  $\text{ZrO}_2$  and  $\text{HfO}_2$ ,” *Nano Lett.* **12**, 4318–4323 (2012).
- <sup>3</sup>E. H. Kisi, C. J. Howard, and R. J. Hill, “Crystal structure of orthorhombic zirconia in partially stabilized zirconia,” *J. Am. Ceram. Soc.* **72**, 1757–1760 (1989).
- <sup>4</sup>X. Sang, E. D. Grimley, T. Schenk, U. Schroeder, and J. M. Lebeau, “On the structural origins of ferroelectricity in  $\text{HfO}_2$  thin films,” *Appl. Phys. Lett.* **106**, 162905 (2015).
- <sup>5</sup>T. Shimizu, T. Yokouchi, T. Oikawa, T. Shiraishi, T. Kiguchi, A. Akama, T. J. Konno, A. Gruverman, and H. Funakubo, “Contribution of oxygen vacancies to the ferroelectric behavior of  $\text{Hf}_{0.5}\text{Zr}_{0.5}\text{O}_2$  thin films,” *Appl. Phys. Lett.* **106**, 112904 (2015).
- <sup>6</sup>M. H. Park, H. J. Kim, Y. J. Kim, W. Lee, T. Moon, and C. S. Hwang, “Evolution of phases and ferroelectric properties of thin  $\text{Hf}_{0.5}\text{Zr}_{0.5}\text{O}_2$  films according to the thickness and annealing temperature,” *Appl. Phys. Lett.* **102**, 242905 (2013).
- <sup>7</sup>P. Polakowski and J. Müller, “Ferroelectricity in undoped hafnium oxide,” *Appl. Phys. Lett.* **106**, 232905 (2015).
- <sup>8</sup>S. E. Reyes-Lillo, K. F. Garrity, and K. M. Rabe, “Antiferroelectricity in thin-film  $\text{ZrO}_2$  from first principles,” *Phys. Rev. B* **90**, 140103(R) (2014).
- <sup>9</sup>T. D. Huan, V. Sharma, G. A. Rossetti, and R. Ramprasad, “Pathways towards ferroelectricity in hafnia,” *Phys. Rev. B* **90**, 064111 (2014).

- <sup>10</sup>R. Materlik, C. Künneth, and A. Kersch, "The origin of ferroelectricity in Hf<sub>1-x</sub>Zr<sub>x</sub>O<sub>2</sub>: A computational investigation and a surface energy model," *J. Appl. Phys.* **117**, 134109 (2015).
- <sup>11</sup>M. Hyuk Park, H. Joon Kim, Y. Jin Kim, T. Moon, and C. Seong Hwang, "The effects of crystallographic orientation and strain of thin Hf<sub>0.5</sub>Zr<sub>0.5</sub>O<sub>2</sub> film on its ferroelectricity," *Appl. Phys. Lett.* **104**, 072901 (2014).
- <sup>12</sup>R. Batra, T. D. Huan, J. L. Jones, G. A. Rossetti, and R. Ramprasad, "Factors favoring ferroelectricity in Hafnia: A first principles computational study," *J. Phys. Chem. C* **121**(8), 4139 (2017).
- <sup>13</sup>M. Hoffmann, U. Schroeder, T. Schenk, T. Shimizu, H. Funakubo, O. Sakata, D. Pohl, M. Drescher, C. Adelman, R. Materlik, A. Kersch, and T. Mikolajick, "Stabilizing the ferroelectric phase in doped hafnium oxide," *J. Appl. Phys.* **118**, 072006 (2015).
- <sup>14</sup>D. Fischer and A. Kersch, "Stabilization of the high-k tetragonal phase in HfO<sub>2</sub>: The influence of dopants and temperature from ab initio simulations," *J. Appl. Phys.* **104**(8), 084104 (2008).
- <sup>15</sup>M. Pešić, F. P. G. Fengler, L. Larcher, A. Padovani, T. Schenk, E. D. Grimley, X. Sang, J. M. LeBeau, S. Slesazek, U. Schroeder, and T. Mikolajick, "Physical mechanisms behind the field-cycling behavior of HfO<sub>2</sub>-based ferroelectric capacitors," *Adv. Funct. Mater.* **26**, 4601–4612 (2016).
- <sup>16</sup>R. C. Garvie, "The occurrence of metastable tetragonal zirconia as a crystallite size effect," *J. Phys. Chem.* **69**, 1238–1243 (1965).
- <sup>17</sup>M. W. Pitcher, S. V. Ushakov, A. Navrotsky, B. F. Woodfield, G. Li, J. Boerio-Goates, and B. M. Tissue, "Energy crossovers in nanocrystalline zirconia," *J. Am. Ceram. Soc.* **88**, 160–167 (2004).
- <sup>18</sup>W. Zhou, S. V. Ushakov, T. Wang, J. G. Ekerdt, A. A. Demkov, and A. Navrotsky, "Hafnia: Energetics of thin films and nanoparticles," *J. Appl. Phys.* **107**, 123514 (2010).
- <sup>19</sup>A. Christensen and E. A. Carter, "First-principles study of the surfaces of zirconia," *Phys. Rev. B* **58**, 8050–8064 (1998).
- <sup>20</sup>R. Batra, H. D. Tran, and R. Ramprasad, "Stabilization of metastable phases in hafnia owing to surface energy effects," *Appl. Phys. Lett.* **108**, 172902 (2016).
- <sup>21</sup>S. Starschich, T. Schenk, U. Schroeder, and U. Boettger, "Ferroelectric and piezoelectric properties of Hf<sub>1-x</sub>Zr<sub>x</sub>O<sub>2</sub> and pure ZrO<sub>2</sub> films," *Appl. Phys. Lett.* **110**, 182905 (2017).
- <sup>22</sup>S. V. Ushakov, A. Navrotsky, Y. Yang, S. Stemmer, K. Kukli, M. Ritala, M. a. Leskelä, P. Fejes, A. Demkov, C. Wang, B.-Y. Nguyen, D. Triyoso, and P. Tobin, "Crystallization in hafnia- and zirconia-based systems," *Phys. Status Solidi* **241**, 2268–2278 (2004).
- <sup>23</sup>E. D. Grimley, T. Schenk, X. Sang, M. Pešić, U. Schroeder, T. Mikolajick, and J. M. LeBeau, "Structural changes underlying field-cycling phenomena in ferroelectric HfO<sub>2</sub> thin films," *Adv. Electron. Mater.* **2**, 1600173 (2016).
- <sup>24</sup>I. Kasatkin, F. Girgsdies, T. Ressler, R. A. Caruso, J. H. Schattka, J. Urban, and K. Weiss, "HRTEM observation of the monoclinic-to-tetragonal (m-t) phase transition in nanocrystalline ZrO<sub>2</sub>," *J. Mater. Sci.* **39**, 2151–2157 (2004).
- <sup>25</sup>H. J. Kim, M. H. Park, Y. J. Kim, Y. H. Lee, T. Moon, K. D. Kim, S. D. Hyun, and C. S. Hwang, "A study on the wake-up effect of ferroelectric Hf<sub>0.5</sub>Zr<sub>0.5</sub>O<sub>2</sub> films by pulse-switching measurement," *Nanoscale* **8**, 1383–1389 (2016).
- <sup>26</sup>C. Lee and X. Gonze, "Lattice dynamics and dielectric properties of SiO<sub>2</sub> stishovite," *Phys. Rev. Lett.* **72**, 1686–1689 (1994).
- <sup>27</sup>X. Gonze, B. Amadon, P.-M. M. Anglade, J.-M. M. Beuken, F. Bottin, P. Boulanger, F. Bruneval, D. Caliste, R. Caracas, M. Côté, T. Deutsch, L. Genovese, P. Ghosez, M. Giantomassi, S. Goedecker, D. R. Hamann, P. Hermet, F. Jollet, G. Jomard, S. Leroux, M. Mancini, S. Mazevet, M. J. T. Oliveira, G. Onida, Y. Pouillon, T. Rangel, G. M. Rignanese, D. Sangalli, R. Shaltaf, M. Torrent, M. J. Verstraete, G. Zerah, J. W. Zwanziger, and M. Cote, "ABINIT: First-principles approach to material and nanosystem properties," *Comput. Phys. Commun.* **180**, 2582–2615 (2009).
- <sup>28</sup>X. Gonze, F. Jollet, F. Abreu Araujo, B. Adams, B. Amadon, T. Applencourt, C. Audouze, J.-M. Beuken, J. Bieder, A. Bokhanchuk, E. Bousquet, F. Bruneval, D. Caliste, M. Côté, F. Dahm, F. Da Pieve, M. Delaveau, M. Di Gennaro, B. Dorado, C. Espejo, G. Geneste, L. Genovese, A. Gerossier, M. Giantomassi, Y. Gillet, D. Hamann, L. He, G. Jomard, J. L. Janssen, S. L. Roux, A. Levitt, A. Lherbier, F. Liu, I. Lukačević, A. Martin, C. Martins, M. Oliveira, S. Poncé, Y. Pouillon, T. Rangel, G.-M. Rignanese, A. Romero, B. Rousseau, O. Rubel, A. Shukri, M. Stankovski, M. Torrent, M. Van Setten, B. Van Troeye, M. Verstraete, D. Waroquiers, J. Wiktor, B. Xu, A. Zhou, and J. Zwanziger, "Recent developments in the ABINIT software package," *Comput. Phys. Commun.* **205**, 106–131 (2016).
- <sup>29</sup>M. Torrent, F. Jollet, G. Zerah, and X. Gonze, "Implementation of the projector augmented-wave method in the ABINIT code: Application to the study of iron under pressure," *Comput. Mater. Sci.* **42**, 337–351 (2008).
- <sup>30</sup>V. Blum, R. Gehrke, F. Hanke, P. Havu, V. Havu, X. Ren, K. Reuter, and M. Scheffler, "Ab initio molecular simulations with numeric atom-centered orbitals," *Comput. Phys. Commun.* **180**, 2175–2196 (2009).
- <sup>31</sup>K. F. Garrity, J. W. Bennett, K. M. Rabe, and D. Vanderbilt, "Pseudopotentials for high-throughput DFT calculations," *Comput. Mater. Sci.* **81**, 446–452 (2014).
- <sup>32</sup>A. Togo and I. Tanaka, "First principles phonon calculations in materials science," *Scr. Mater.* **108**, 1–5 (2015).
- <sup>33</sup>H. J. Monkhorst and J. D. Pack, "Special points for Brillouin-zone integrations," *Phys. Rev. B* **13**, 5188–5192 (1976).
- <sup>34</sup>X. Zhao and D. Vanderbilt, "First-principles study of structural, vibrational, and lattice dielectric properties of hafnium oxide," *Phys. Rev. B* **65**, 233106 (2002); e-print [arXiv:0202454](https://arxiv.org/abs/0202454) [cond-mat].
- <sup>35</sup>P. Tsipas, S. N. Volkos, A. Sotiropoulos, S. F. Galata, G. Mavrou, D. Tsoutsou, Y. Panayiotatos, A. Dimoulas, C. Marchiori, and J. Fompeyrine, "Germanium-induced stabilization of a very high-k zirconia phase in ZrO<sub>2</sub>/GeO<sub>2</sub> gate stacks," *Appl. Phys. Lett.* **93**, 082904 (2008).
- <sup>36</sup>M. Hoffmann, U. Schroeder, C. Künneth, A. Kersch, S. Starschich, U. Böttger, and T. Mikolajick, "Ferroelectric phase transitions in nanoscale HfO<sub>2</sub> films enable giant pyroelectric energy conversion and highly efficient supercapacitors," *Nano Energy* **18**, 154–164 (2015).
- <sup>37</sup>M. H. Park, Y. H. Lee, H. J. Kim, S. Tony, L. Woonkyu, K. D. Kim, F. P. G. Fengler, T. Mikolajick, U. Schroeder, and C. S. Hwang, "Surface energy as key to ferroelectricity in nanoscale hafnia-zirconia: Comparison of model and experiment," (unpublished).
- <sup>38</sup>H. J. Kim, M. H. Park, Y. J. Kim, Y. H. Lee, W. Jeon, T. Gwon, T. Moon, K. D. Kim, and C. S. Hwang, "Grain size engineering for ferroelectric Hf<sub>0.5</sub>Zr<sub>0.5</sub>O<sub>2</sub> films by an insertion of Al<sub>2</sub>O<sub>3</sub> interlayer," *Appl. Phys. Lett.* **105**, 192903 (2014).
- <sup>39</sup>D. J. Wales and J. P. K. Doye, "Global optimization by basin-hopping and the lowest energy structures of Lennard-Jones clusters containing up to 110 atoms," *J. Phys. Chem. A* **101**, 5111–5116 (1997).
- <sup>40</sup>T. D. Huan, V. Sharma, G. A. Rossetti, and R. Ramprasad, "Pathways towards ferroelectricity in hafnia," *Phys. Rev. B: Condens. Matter Mater. Phys.* **90**, 064111 (2014).
- <sup>41</sup>T. Shiraishi, K. Katayama, T. Yokouchi, T. Shimizu, T. Oikawa, O. Sakata, H. Uchida, Y. Imai, T. Kiguchi, T. J. Konno, and H. Funakubo, "Impact of mechanical stress on ferroelectricity in (Hf<sub>0.5</sub>Zr<sub>0.5</sub>)O<sub>2</sub> thin films," *Appl. Phys. Lett.* **108**, 262904 (2016).



# The Impact of Charge Compensated and Uncompensated Strontium Defects on the Stabilization of the Ferroelectric Phase in HfO<sub>2</sub>

Robin Materlik\*, Christopher Künneth\*, Thomas Mikolajick, and Alfred Kersch

\*Contributed equally to this work.

Appl. Phys. Lett., vol. 111, no. 8, p. 82902, 2017.

DOI: [10.1063/1.4993110](https://doi.org/10.1063/1.4993110)

Reproduced from the Applied Physics Letters, with the permission of AIP Publishing.

# The impact of charge compensated and uncompensated strontium defects on the stabilization of the ferroelectric phase in HfO<sub>2</sub>

Robin Materlik,<sup>1,a)</sup> Christopher Künneth,<sup>1,a)</sup> Thomas Mikolajick,<sup>2,3</sup> and Alfred Kersch<sup>1,b)</sup>

<sup>1</sup>Department of Applied Sciences and Mechatronics, Munich University of Applied Sciences, Lothstr. 34, 80335 Munich, Germany

<sup>2</sup>NaMLab gGmbH, Noethnitzer Strasse 64, 01187 Dresden, Germany

<sup>3</sup>Technische Universität Dresden, Noethnitzer Strasse 64, 01187 Dresden, Germany

(Received 27 June 2017; accepted 12 August 2017; published online 22 August 2017)

Different dopants with their specific dopant concentration can be utilized to produce ferroelectric HfO<sub>2</sub> thin films. In this work, it is explored for Sr in a comprehensive first-principles study. Density functional calculations reveal structure, formation energy, and total energy of the Sr related defects in HfO<sub>2</sub>. We found the charge compensated defect with an associated oxygen vacancy Sr<sub>Hf</sub>V<sub>O</sub> to strongly favour the non-ferroelectric, tetragonal P4<sub>2</sub>/mnc phase energetically. In contrast, the uncompensated defect without oxygen vacancy Sr<sub>Hf</sub> favours the ferroelectric, orthorhombic Pca2<sub>1</sub> phase. According to the formation energy, the uncompensated defect can form easily under oxygen rich conditions in the production process. Low oxygen partial pressure existing over the lifetime promotes the loss of oxygen leading to V<sub>O</sub>, and thus, the destabilization of the ferroelectric, orthorhombic Pca2<sub>1</sub> phase is accompanied by an increase of the leakage current. This study attempts to fundamentally explain the stabilization of the ferroelectric, orthorhombic Pca2<sub>1</sub> phase by doping. Published by AIP Publishing. [<http://dx.doi.org/10.1063/1.4993110>]

Polycrystalline HfO<sub>2</sub> thin films produced by Atomic Layer Deposition (ALD) or Chemical Solution Deposition (CSD) can exhibit ferroelectric properties if they are appropriately doped.<sup>1–9</sup> An orthorhombic, non-centrosymmetric phase (Pca2<sub>1</sub>) has been proposed as the source of these properties which has since been confirmed by an electron diffraction study.<sup>10</sup> Furthermore, another theoretically proposed ferroelectric Pmn2<sub>1</sub> phase has been ruled out by the same study and is therefore not included in this work. Pure HfO<sub>2</sub> occurs naturally in a monoclinic (P2<sub>1</sub>/c) phase. With increasing temperature, a transformation into the tetragonal (P4<sub>2</sub>/mnc) and then the cubic (Fm3m) phase occurs,<sup>11</sup> avoiding the orthorhombic phase. Different Density Functional Theory (DFT) studies consistently calculate the total energy of the orthorhombic phase as the second most stable phase after the monoclinic phase and are able to reproduce the thermally driven phase transformation,<sup>12,13</sup> giving credibility to the used density functionals.

To explain the occurrence of the ferroelectric phenomena, factors favouring the orthorhombic phase, including entropy contribution, surface or interface energy, stress, and doping, have been proposed.<sup>13–15</sup> Surface or interface energy stems from the large surface to volume ratio of the individual crystals in the polycrystalline HfO<sub>2</sub> thin films<sup>13,16</sup> with grain sizes typically in the range of the film thickness (5 nm–30 nm).<sup>17–20</sup> It explains the generally observed decrease or disappearance of the ferroelectric properties with the increasing film thickness.<sup>21</sup> For the case of Hf<sub>1–x</sub>Zr<sub>x</sub>O<sub>2</sub>, at  $x = 0.5$ , surface energy or interface energy has been found to be sufficient to explain the stability of the orthorhombic phase.<sup>13,16</sup> For thin films based on pure HfO<sub>2</sub>, surface or interface energy is insufficient, except for the case of very small grains.<sup>17</sup>

In such thin films, further stabilization by appropriate doping is required.<sup>7–9,22,23</sup> In the case of Sr doping, ferroelectricity was observed in a 10 nm film between 1.7 and 7.9 mol. % SrO content with the maximum polarization observed at around 3.4 mol. % SrO.<sup>24</sup> The effect of doping on HfO<sub>2</sub> phases has been investigated in earlier works,<sup>25,26</sup> but the Pca2<sub>1</sub> and II-valent dopants were not included in the study. The authors found stabilization of the tetragonal phase by IV-valent dopants and stabilization of the cubic phase by III-valent dopants. Due to its II-valent nature, it is expected that each Sr dopant atom is accompanied by an oxygen vacancy for charge compensation. Furthermore, due to opposite charges, the Sr<sub>Hf</sub><sup>–2</sup> and V<sub>O</sub><sup>+2</sup> defect should strongly attract each other leading to [Sr<sub>Hf</sub>V<sub>O</sub>]<sup>0</sup>, similar to the case of Mg<sub>Hf</sub><sup>–2</sup> or Ba<sub>Hf</sub><sup>–2</sup> doping investigated in Refs. 27 and 28. However, the defect concentration created during the manufacturing process is not explicitly known and strongly depends on the chemical potential of the defects. In this work, the defect notation of Freysoldt *et al.* is used.<sup>29</sup>

To propose a consistent scenario for the ferroelectric stability of a Sr doped HfO<sub>2</sub> thin film, we determined total energy and defect formation energy for various defects in monoclinic, orthorhombic, tetragonal, and cubic HfO<sub>2</sub> from first principle calculations. These defects include single oxygen vacancies V<sub>O</sub><sup>q</sup> with the charges  $q = 0, +1, +2$ , Sr substituted for Hf with Sr<sub>Hf</sub><sup>q</sup> ( $q = 0, -1, -2$ ), and the compensated defect [Sr<sub>Hf</sub>V<sub>O</sub>]<sup>q</sup> ( $q = 0, -1, -2$ ). Oxygen vacancies were placed on the eight next neighboring oxygen sites of a given Sr or Hf atom excluding structural equivalent positions. All shown results always depict the energetically most favourable position. Placing one defect in a 96 or 48 atomic super cell corresponds to a concentration of 3.125 f.u.% (= 1 defect/32 formula units) and 6.25 f.u.% (= 1 defect/16 formula units), respectively.

<sup>a)</sup>R. Materlik and C. Künneth contributed equally to this work.

<sup>b)</sup>Electronic mail: [alfred.kersch@hm.edu](mailto:alfred.kersch@hm.edu).

DFT calculations were performed using the Local Density Approximation (LDA) and Projector Augmented Wave (PAW)<sup>30</sup> Pseudo Potentials (PP) from the GBRV library<sup>31,32</sup> with the ABINIT code.<sup>33–35</sup> Several LDA calculations were repeated with the all electron code FHI-AIMS<sup>36</sup> based upon numeric, atom-centered orbitals of type tight with first and second tier enabled. In the remainder of this work, we will refer to those two methods as plane waves (PW) and numerical orbitals (NO), respectively. The stopping criteria for the electronic convergence were force criteria of  $10^{-6}$  Hartree/Bohr (PW) and  $10^{-4}$  eV/Å (NO). The stopping criteria for the structural convergence were force criteria of  $10^{-5}$  Hartree/Bohr (PW) and  $10^{-3}$  eV/Å (NO). Charged and neutral defect calculations in monoclinic, tetragonal, cubic, and orthorhombic HfO<sub>2</sub> were performed with 96 atomic super cells using a  $2 \times 2 \times 2$  Monkhorst-Pack k-point set, a plane wave cut off of 18 Ha, and a PAW cut off of 22 Ha in accordance with a convergence study. Charge neutral 48 atomic super cells with a  $2 \times 4 \times 2$  k-point grid were used to determine the phase stability at the defect concentration of 6.25 f.u.%.

The defect formation energies  $E_f$  were calculated as

$$E_f(X, q) = U(X, q) - U(\text{pure}) - \sum_i n_i \mu_i + q(\epsilon_F + \epsilon_{\text{VB}}(\text{pure}) + \Delta V(X, 0)) + E_{\text{Corr}}(X, q), \quad (1)$$

using the DFT total energies  $U$  of both HfO<sub>2</sub> without and with a defect  $X \in \{\text{Sr}_{\text{Hf}}^q, [\text{Sr}_{\text{Hf}}\text{V}_\text{O}]^q, \text{V}_\text{O}^q\}$  and charge  $q$ . The chemical potential and number of defect atoms of each species is given by  $\mu_i$  and  $n_i$ , respectively. The Fermi energy is  $\epsilon_F$ , and the valence band edge is  $\epsilon_{\text{VB}}$ . A charge correction  $E_{\text{Corr}}$  with the scaling law<sup>37</sup>  $E_f \sim a/L + c$  using a 324 atomic super cell and a potential alignment  $\Delta V$  was applied.  $a$  and  $c$  are fit parameters, and  $L$  is the size of the super cell. The chemical potential of Hf was set to the total energy of hcp Hf and of Sr was calculated by the equilibrium condition  $\mu_{\text{Sr}} = \mu_{\text{SrO}} - \mu_{\text{O}}$ . For the chemical potential of oxygen, two cases are considered: oxygen rich and oxygen deficient.<sup>38,39</sup> In the oxygen rich case,  $\mu_{\text{O}}$  is set to  $\mu_{\text{O}_2}/2$ . Ferroelectric HfO<sub>2</sub> is often deposited on TiN electrodes,<sup>1,2,10,17–20,24,40</sup> which can exist in a partially oxidized state. The oxygen chemical potential  $\mu_{\text{O}}$  for the deficient conditions uses oxygen precipitation into anatase TiO<sub>2</sub>. In similar studies,<sup>28</sup> precipitation into SiO<sub>2</sub> has been used adapting to a Si substrate. Both assumptions, however, lead to very similar formation enthalpies. We therefore calculate  $\mu_{\text{O}} = (\mu_{\text{TiO}_2} - \mu_{\text{Ti}})/2$  for the oxygen deficient case.

The main result of this paper is the connection between the phase stability of defective HfO<sub>2</sub> and the conditions under which the defective material can form. Figure 1(a) shows the total energy difference  $\Delta U$  in the monoclinic phase for the Sr<sub>Hf</sub> defect as a function of the Sr concentration. Both the orthorhombic and tetragonal phases are depicted and calculated with PW and NO. The cubic phase turned out to be unstable and is therefore not shown here.

The defect free orthorhombic phase has a  $\Delta U$  of 53 meV (PW) and 49 meV (NO), while the tetragonal phase has a  $\Delta U$  of 115 meV (PW) or 114 meV (NO). The Sr<sub>Hf</sub> defects lead to

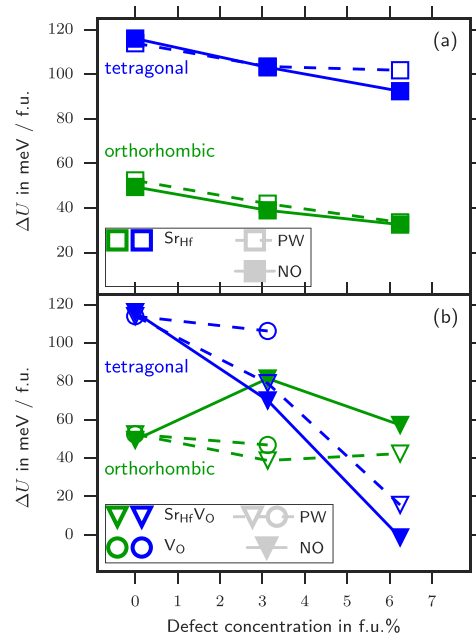


FIG. 1. Defect concentration dependent energy difference  $\Delta U = U(o \parallel t) - U(m)$  to the monoclinic phase for the PW (empty symbols, dashed line) and NO (full symbols, continuous line) methodology for the tetragonal (blue) and orthorhombic (green) phases. The different defects are indicated by symbols. (a) shows the vacancy free defects Sr<sub>Hf</sub> (squares) and (b) shows the vacancy related defects V<sub>O</sub> (triangles) and Sr<sub>Hf</sub>V<sub>O</sub> (circles).

a decrease in  $\Delta U$  of about 20 meV for 6 Sr-f.u.% which is roughly the same for both the tetragonal and orthorhombic phases. Therefore, the defect contributes to the stabilization but not sufficiently to fully stabilize the orthorhombic phase on its own. However, according to previous works, in Hf<sub>1-x</sub>Zr<sub>x</sub>O<sub>2</sub>,<sup>13,16,41</sup> the surface or interface energy of grains can decrease the energy of the tetragonal and orthorhombic phases below the monoclinic phase and, thus, suppress the formation of the monoclinic phase. The surface or interface energy for the tetragonal and orthorhombic phase is expected to be very similar. Proposing a surface or interface energy penalty for the monoclinic phase is difficult in this case since the issue has not been investigated for doped HfO<sub>2</sub> so far. In Hf<sub>1-x</sub>Zr<sub>x</sub>O<sub>2</sub> considering Zr as a dopant, a typical energy penalty of about 20 meV (for typical grains of 10 nm diameter in a 10 nm film) was found for HfO<sub>2</sub> linearly increasing to about 60 meV for ZrO<sub>2</sub>. At the same time, the interface energies increased from 174 mJ/m<sup>2</sup> to 490 mJ/m<sup>2</sup>.<sup>16</sup> There is another argument in favour of a significant increase in the energy penalty for the monoclinic phase with doping. The authors<sup>16</sup> identified the energy penalty with the energy of the tetragonal/monoclinic interface observed by Grimley.<sup>42</sup> An interface energy, however, is expected to depend sensitively on doping. Altogether, we expect a surface or interface related energy penalty for the monoclinic phase starting at around 30 meV for pure HfO<sub>2</sub> and increasing significantly with doping. We therefore expect  $\Delta U$  of the orthorhombic phase to become negative for some Sr concentrations and the film to become ferroelectric. The main factor for the ferroelectric stabilization is that the orthorhombic phase turns out always to be more favourable than the tetragonal phase.

This is not the case for the compensated defect [Sr<sub>Hf</sub>V<sub>O</sub>]<sup>0</sup> as shown in Fig. 1(b). The change in  $\Delta U$  is much

larger for the tetragonal phase than for the orthorhombic phase. Above a threshold of 2 f.u.% to 3 f.u.% (NO) or 5 f.u.% (PW), the material loses ferroelectricity, and the tetragonal phase replaces the orthorhombic phase as the most favorable. This would severely limit the dopant concentration range in which ferroelectric properties can be observed and is therefore in conflict with the experimentally observed range for ferroelectricity of 1.7 mol. % to 7.9 mol. % dopant concentration.<sup>8,24</sup>

This leads to the question, whether the  $\text{Sr}_{\text{Hf}}$  is indeed always compensated with an oxygen vacancy  $\text{V}_{\text{O}}$  as stoichiometry suggests. An estimation of the vacancy concentration results from an electrical measurement of the leakage current in Sr doped Hf by Pešić *et al.*,<sup>40</sup> who extracted a vacancy concentration of  $5 \times 10^{19} \text{ cm}^{-3}$ , which is significantly less than required to pair every Sr atom ( $1.4 \times 10^{21} \text{ cm}^{-3}$  for 5 f.u.%) with a vacancy. Crucial for the question whether  $\text{Sr}_{\text{Hf}}$  or  $\text{Sr}_{\text{Hf}}\text{V}_{\text{O}}$  should be expected is the formation energy as a function of the oxygen chemical potential and a kinetic process creating the defect.<sup>43</sup>

Figure 2(a) shows the formation energies under oxygen rich conditions for the orthorhombic phase and for oxygen in the III-valent and IV-valent positions. The formation energy does not differ very much from the monoclinic phase (not shown here). The LDA bandgap for the orthorhombic phase was found to be 4.41 eV (3.98 eV for the monoclinic phase and 4.56 eV for the tetragonal phase). The individual formation energy of charged  $\text{Sr}_{\text{Hf}}^{-2}$  and  $\text{V}_{\text{O}}^{+2}$  defects is lower than the formation energy of the combined charged neutral  $[\text{Sr}_{\text{Hf}}\text{V}_{\text{O}}]^0$  defect. This might lead to a separated creation of  $\text{Sr}_{\text{Hf}}^{-2}$  and  $\text{V}_{\text{O}}^{+2}$ . However, since vacancies are very mobile, the positively charged vacancies  $\text{V}_{\text{O}}^{+2}$  combine with the negatively charged  $\text{Sr}_{\text{Hf}}^{-2}$  creating  $[\text{Sr}_{\text{Hf}}\text{V}_{\text{O}}]^0$  with an energy release

of 2.36 eV. Under oxygen rich conditions, few  $\text{Sr}_{\text{Hf}}\text{V}_{\text{O}}$  are expected in the end except close to the interface where some oxygen loss towards the electrode has to be expected. As a result, a film with substitutional  $\text{Sr}_{\text{Hf}}$  defects and few compensated defects is expected, but at the electrode interface, a significant amount of compensated  $\text{Sr}_{\text{Hf}}\text{V}_{\text{O}}$  defects is possible which may stabilize a tetragonal interlayer<sup>42</sup> and may be a prerequisite of the energy penalty to suppress the monoclinic phase. This would support the assumptions made by Pešić.<sup>40</sup> The acceptor doping without charge compensation achieved under oxygen rich conditions is often desired to improve electric isolation since the negative space charge increases the band offset to the electrode.

During the life time of a ferroelectric  $\text{HfO}_2$  stack, the external oxygen partial pressure is defined by the oxidized electrodes. Figure 2(b) shows the formation energy under such oxygen deficient conditions. As there is no new Sr-source, only vacancies can be created possibly due to field cycling. Since the energy of  $[\text{Sr}_{\text{Hf}}\text{V}_{\text{O}}]^0$  is lower than the sum of  $\text{V}_{\text{O}}^{+2}$  and  $\text{Sr}_{\text{Hf}}^{-2}$ , these vacancies will recombine quickly with the already present substitutional Sr defects, leading to a charge compensation. The concentration of  $\text{Sr}_{\text{Hf}}^{-2}$  will decrease and that of  $[\text{Sr}_{\text{Hf}}\text{V}_{\text{O}}]^0$  will increase. The implication on the phase stability is a gradual degradation of the orthorhombic phase content accompanied by a decrease in the remanent polarization. A further implication concerning the electron transport is that the charge transition level of a deep defect state promotes trap assisted tunneling (TAT). The related charge transition levels  $\epsilon(0/-1) = 3.63 \text{ eV}$  and  $\epsilon(-1/-2) = 3.92 \text{ eV}$  close to the conduction band release electrons which modify the space charge and contribute to TAT. Therefore, a moderate increase in leakage current with time would be expected, indicating an increase in charge compensated defects. As the creation of  $\text{Sr}_{\text{Hf}}\text{V}_{\text{O}}$  under oxygen deficient conditions is preferred, the concentration of  $\text{V}_{\text{O}}$  will stay on a relatively low level and constant over time. However, the  $\text{V}_{\text{O}}$  defects with charge transition levels at  $\epsilon(+2/+1) = 2.41 \text{ eV}$  and  $\epsilon(+1/0) = 2.81 \text{ eV}$  are about 2 eV below the conduction band and, therefore, can be occupied by tunneling electrons promoting leakage current.

A last argument explains why the  $\text{Sr}_{\text{Hf}}$  defect favors the orthorhombic phase and  $\text{Sr}_{\text{Hf}}\text{V}_{\text{O}}$  defect favors the tetragonal phase in total energy. The cause for the stabilization of the orthorhombic and tetragonal phases by  $\text{Sr}_{\text{Hf}}$  defects can be found in the bond length of the Sr atom to its neighboring oxygen atoms. Calculations of SrO and SrO<sub>2</sub> show a bond length between 2.53 and 2.60 Å, respectively. In undoped  $\text{HfO}_2$ , the average bond length is 2.12 Å for the monoclinic and orthorhombic phases and 2.17 Å for the tetragonal phase. Substituting a Sr atom on a Hf site, the bond length increases to only 2.35 Å for the monoclinic phase but to 2.37 Å for the orthorhombic and tetragonal phases. Sr in monoclinic  $\text{HfO}_2$  is therefore energetically more unfavourable than in the orthorhombic or tetragonal phase; therefore, the energy difference to the monoclinic phase decreases with doping. Introducing vacancies, the monoclinic average bond length increases to 2.38 Å, but the tetragonal value of 2.47 Å almost matches the value of SrO and is accompanied by the significant decrease in the total energy difference (see Fig. 1).

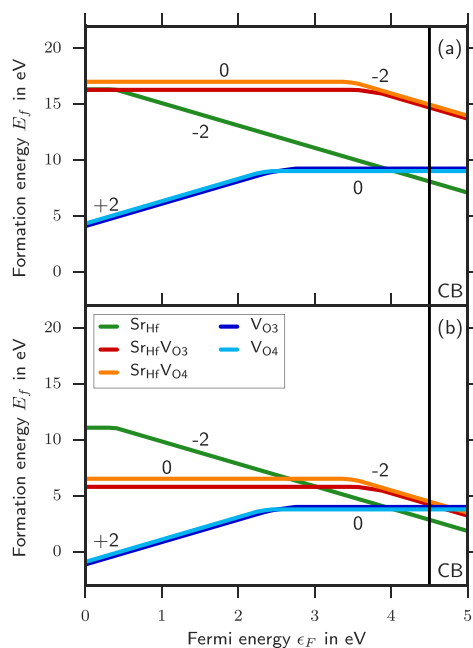


FIG. 2. It shows the formation energies of the orthorhombic phase for (a) oxygen rich and (b) oxygen deficient conditions, respectively. The formation energies are calculated by Eq. (1), and the charge states are indicated by numbers. The values are not scaled to the experimental bandgap, and CB marks the LDA-DFT calculated conduction band.



In summary, a mechanism is proposed, based on first-principles DFT calculations, to explain the influence of Sr doping on the phase stability in  $\text{HfO}_2$ . The tetragonal phase is strongly preferred by the incorporation of the  $\text{Sr}_{\text{Hf}}\text{V}_\text{O}$  defects, while the  $\text{Sr}_{\text{Hf}}$  allows for the stabilization of the ferroelectric orthorhombic phase. The uncompensated defect can form in sufficiently oxygen rich environments, which might exist during the production process. The loss of oxygen during field cycling may increase the charge compensation which promotes the phase transformation into other  $\text{HfO}_2$  polymorphs. This contributes to the fatigue behavior. The proposed mechanism has the potential to describe the action of other dopants on the ferroelectric phase in  $\text{HfO}_2$  if appropriately adapted and expanded.

The authors are thankful to U. Schröder, T. Schenk, and Min Hyuk Park from NamLab/SNU and U. Böttger and S. Starschich from RWTH Aachen for discussions. The German Research Foundation (Deutsche Forschungsgemeinschaft) is acknowledged for funding this research in the frame of the project “Inferox” (Project No. MI 1247/11-1). The authors gratefully acknowledge the Gauss Centre for Supercomputing e.V. ([www.gauss-centre.eu](http://www.gauss-centre.eu)) for funding this project by providing computing time on the GCS Supercomputer SuperMUC at Leibniz Supercomputing Center (LRZ, [www.lrz.de](http://www.lrz.de)).

- <sup>1</sup>T. S. Böske, J. Müller, D. Bräuhäus, U. Schröder, and U. Böttger, “Ferroelectricity in hafnium oxide thin films,” *Appl. Phys. Lett.* **99**, 102903 (2011).
- <sup>2</sup>J. Müller, T. S. Böske, U. Schröder, S. Mueller, D. Bräuhäus, U. Böttger, L. Frey, and T. Mikolajick, “Ferroelectricity in simple binary  $\text{ZrO}_2$  and  $\text{HfO}_2$ ,” *Nano Lett.* **12**, 4318–4323 (2012), pMID: 22812909.
- <sup>3</sup>M. H. Park, H. J. Kim, Y. J. Kim, W. Lee, H. K. Kim, and C. S. Hwang, “Effect of forming gas annealing on the ferroelectric properties of  $\text{Hf}_{0.5}\text{Zr}_{0.5}\text{O}_2$  thin films with and without Pt electrodes,” *Appl. Phys. Lett.* **102**, 112914 (2013).
- <sup>4</sup>P. D. Lomenzo, Q. Takmeel, C. Zhou, Y. Liu, C. M. Fancher, J. L. Jones, S. Moghaddam, and T. Nishida, “The effects of layering in ferroelectric Si-doped  $\text{HfO}_2$  thin films,” *Appl. Phys. Lett.* **105**, 072906 (2014).
- <sup>5</sup>T. Shimizu, K. Katayama, T. Kiguchi, A. Akama, T. J. Konno, O. Sakata, and H. Funakubo, “The demonstration of significant ferroelectricity in epitaxial Y-doped  $\text{HfO}_2$  film,” *Sci. Rep.* **6**, 32931 (2016).
- <sup>6</sup>S. Starschich, T. Schenk, U. Schroeder, and U. Boettger, “Ferroelectric and piezoelectric properties of  $\text{Hf}_{1-x}\text{Zr}_x\text{O}_2$  and pure  $\text{ZrO}_2$  films,” *Appl. Phys. Lett.* **110**, 182905 (2017).
- <sup>7</sup>M. H. Park, Y. H. Lee, H. J. Kim, Y. J. Kim, T. Moon, K. D. Kim, J. Müller, A. Kersch, U. Schroeder, T. Mikolajick, and C. S. Hwang, “Ferroelectricity and antiferroelectricity of doped thin  $\text{HfO}_2$ -based films,” *Adv. Mater.* **27**, 1811–1831 (2015).
- <sup>8</sup>U. Schroeder, E. Yurchuk, J. Müller, D. Martin, T. Schenk, P. Polakowski, C. Adelman, M. I. Popovici, S. V. Kalinin, and T. Mikolajick, “Impact of different dopants on the switching properties of ferroelectric hafniumoxide,” *Jpn J. Appl. Phys., Part 2* **53**, 08LE02 (2014).
- <sup>9</sup>T. Olsen, U. Schröder, S. Müller, A. Krause, D. Martin, A. Singh, J. Müller, M. Geidel, and T. Mikolajick, “Co-sputtering yttrium into hafnium oxide thin films to produce ferroelectric properties,” *Appl. Phys. Lett.* **101**, 082905 (2012).
- <sup>10</sup>X. Sang, E. D. Grimley, T. Schenk, U. Schroeder, and J. M. LeBeau, “On the structural origins of ferroelectricity in  $\text{HfO}_2$  thin films,” *Appl. Phys. Lett.* **106**, 162905 (2015).
- <sup>11</sup>J. Wang, H. P. Li, and R. Stevens, “Hafnia and hafnia-toughened ceramics,” *J. Mater. Sci.* **27**, 5397–5430 (1992).
- <sup>12</sup>T. D. Huan, V. Sharma, G. A. Rossetti, and R. Ramprasad, “Pathways towards ferroelectricity in hafnia,” *Phys. Rev. B* **90**, 064111 (2014).
- <sup>13</sup>R. Materlik, C. Künneht, and A. Kersch, “The origin of ferroelectricity in  $\text{Hf}_{1-x}\text{Zr}_x\text{O}_2$ : A computational investigation and a surface energy model,” *J. Appl. Phys.* **117**, 134109 (2015).
- <sup>14</sup>S. E. Reyes-Lillo, K. F. Garrity, and K. M. Rabe, “Antiferroelectricity in thin-film  $\text{ZrO}_2$  from first principles,” *Phys. Rev. B* **90**, 140103 (2014).
- <sup>15</sup>R. Batra, H. D. Tran, and R. Ramprasad, “Stabilization of metastable phases in hafnia owing to surface energy effects,” *Appl. Phys. Lett.* **108**, 172902 (2016).
- <sup>16</sup>C. Künneht, R. Materlik, and A. Kersch, “Modeling ferroelectric film properties and size effects from tetragonal interlayer in  $\text{Hf}_{1-x}\text{Zr}_x\text{O}_2$  grains,” *J. Appl. Phys.* **121**, 205304 (2017).
- <sup>17</sup>P. Polakowski and J. Müller, “Ferroelectricity in undoped hafnium oxide,” *Appl. Phys. Lett.* **106**, 232905 (2015).
- <sup>18</sup>M. H. Park, H. J. Kim, Y. J. Kim, Y. H. Lee, T. Moon, K. D. Kim, S. D. Hyun, and C. S. Hwang, “Study on the size effect in  $\text{Hf}_{0.5}\text{Zr}_{0.5}\text{O}_2$  films thinner than 8 nm before and after wake-up field cycling,” *Appl. Phys. Lett.* **107**, 192907 (2015).
- <sup>19</sup>M. H. Park, H. J. Kim, Y. J. Kim, W. Lee, T. Moon, and C. S. Hwang, “Evolution of phases and ferroelectric properties of thin  $\text{Hf}_{0.5}\text{Zr}_{0.5}\text{O}_2$  films according to the thickness and annealing temperature,” *Appl. Phys. Lett.* **102**, 242905 (2013).
- <sup>20</sup>H. J. Kim, M. H. Park, Y. J. Kim, Y. H. Lee, W. Jeon, T. Gwon, T. Moon, K. D. Kim, and C. S. Hwang, “Grain size engineering for ferroelectric  $\text{Hf}_{0.5}\text{Zr}_{0.5}\text{O}_2$  films by an insertion of  $\text{Al}_2\text{O}_3$  interlayer,” *Appl. Phys. Lett.* **105**, 192903 (2014).
- <sup>21</sup>M. Hoffmann, U. Schroeder, T. Schenk, T. Shimizu, H. Funakubo, O. Sakata, D. Pohl, M. Drescher, C. Adelman, R. Materlik, A. Kersch, and T. Mikolajick, “Stabilizing the ferroelectric phase in doped hafnium oxide,” *J. Appl. Phys.* **118**, 072006 (2015).
- <sup>22</sup>S. Mueller, J. Mueller, A. Singh, S. Riedel, J. Sundqvist, U. Schroeder, and T. Mikolajick, “Incipient ferroelectricity in Al-doped  $\text{HfO}_2$  thin films,” *Adv. Funct. Mater.* **22**, 2412–2417 (2012).
- <sup>23</sup>S. Mueller, C. Adelman, A. Singh, S. Van Elshocht, U. Schroeder, and T. Mikolajick, “Ferroelectricity in Gd-doped  $\text{HfO}_2$  thin films,” *ECS J. Solid State Sci. Technol.* **1**, N123–N126 (2012).
- <sup>24</sup>T. Schenk, S. Mueller, U. Schroeder, R. Materlik, A. Kersch, M. Popovici, C. Adelman, S. V. Elshocht, and T. Mikolajick, “Strontium doped hafnium oxide thin films: Wide process window for ferroelectric memories,” in *2013 Proceedings of the European Solid-State Device Research Conference (ESSDERC)* (2013), pp. 260–263.
- <sup>25</sup>C.-K. Lee, E. Cho, H.-S. Lee, C. S. Hwang, and S. Han, “First-principles study on doping and phase stability of  $\text{HfO}_2$ ,” *Phys. Rev. B* **78**, 012102 (2008).
- <sup>26</sup>D. Fischer and A. Kersch, “Stabilization of the high-k tetragonal phase in  $\text{HfO}_2$ : The influence of dopants and temperature from ab initio simulations,” *J. Appl. Phys.* **104**, 084104 (2008).
- <sup>27</sup>N. Umezawa, M. Sato, and K. Shiraishi, “Reduction in charged defects associated with oxygen vacancies in hafnia by magnesium incorporation: First-principles study,” *Appl. Phys. Lett.* **93**, 223104 (2008).
- <sup>28</sup>N. Umezawa, “Effects of barium incorporation into  $\text{HfO}_2$  gate dielectrics on reduction in charged defects: First-principles study,” *Appl. Phys. Lett.* **94**, 022903 (2009).
- <sup>29</sup>C. Freysoldt, B. Grabowski, T. Hickel, J. Neugebauer, G. Kresse, A. Janotti, and C. G. Van de Walle, “First-principles calculations for point defects in solids,” *Rev. Mod. Phys.* **86**, 253–305 (2014).
- <sup>30</sup>P. E. Blöchl, “Projector augmented-wave method,” *Phys. Rev. B* **50**, 17953–17979 (1994).
- <sup>31</sup>K. M. R. Kevin, F. Garrity, J. W. Bennett, and D. Vanderbilt, <https://www.physics.rutgers.edu/gbrv/> for “GBRV high-throughput pseudopotentials.”
- <sup>32</sup>K. F. Garrity, J. W. Bennett, K. M. Rabe, and D. Vanderbilt, “Pseudopotentials for high-throughput dft calculations,” *Comput. Mater. Sci.* **81**, 446–452 (2014).
- <sup>33</sup>X. Gonze, B. Amadon, P.-M. Anglade, J.-M. Beuken, F. Bottin, P. Boulanger, F. Bruneval, D. Caliste, R. Caracas, M. Côté, T. Deutsch, L. Genovese, P. Ghosez, M. Giantomassi, S. Goedecker, D. Hamann, P. Hermet, F. Jollet, G. Jomard, S. Leroux, M. Mancini, S. Mazevet, M. Oliveira, G. Onida, Y. Pouillon, T. Rangel, G.-M. Rignanese, D. Sangalli, R. Shaltaf, M. Torrent, M. Verstraete, G. Zerah, and J. Zwanziger, “Abinit: First-principles approach to material and nanosystem properties,” *Comput. Phys. Commun.* **180**, 2582–2615 (2009). 40 YEARS OF CPC: A celebratory issue focused on quality software for high performance, grid and novel computing architectures.
- <sup>34</sup>X. Gonze, F. Jollet, F. A. Araujo, D. Adams, B. Amadon, T. Applencourt, C. Audouze, J.-M. Beuken, J. Bieder, A. Bokhanchuk, E. Bousquet, F. Bruneval, D. Caliste, M. Côté, F. Dahm, F. D. Pieve, M. Delaveau, M. D. Gennaro, B. Dorado, C. Espejo, G. Geneste, L. Genovese, A. Gerossier, M. Giantomassi, Y. Gillet, D. Hamann, L. He, G. Jomard, J. L. Janssen, S. L. Roux, A. Levitt, A. Lherbier, F. Liu, I. Lukačević, A. Martin, C.

- Martins, M. Oliveira, S. Ponc e, Y. Pouillon, T. Rangel, G.-M. Rignanese, A. Romero, B. Rousseau, O. Rubel, A. Shukri, M. Stankovski, M. Torrent, M. V. Setten, B. V. Troeye, M. Verstraete, D. Waroquiers, J. Wiktor, B. Xu, A. Zhou, and J. Zwanziger, "Recent developments in the abinit software package," *Comput. Phys. Commun.* **205**, 106–131 (2016).
- <sup>35</sup>M. Torrent, F. Jollet, F. Bottin, G. Z erah, and X. Gonze, "Implementation of the projector augmented-wave method in the abinit code: Application to the study of iron under pressure," *Comput. Mater. Sci.* **42**, 337–351 (2008).
- <sup>36</sup>V. Blum, R. Gehrke, F. Hanke, P. Havu, V. Havu, X. Ren, K. Reuter, and M. Scheffler, "Ab initio molecular simulations with numeric atom-centered orbitals," *Comput. Phys. Commun.* **180**, 2175–2196 (2009).
- <sup>37</sup>G. Makov and M. C. Payne, "Periodic boundary conditions in ab initio calculations," *Phys. Rev. B* **51**, 4014–4022 (1995).
- <sup>38</sup>C. Tang and R. Ramprasad, "Point defect chemistry in amorphous HfO<sub>2</sub>: Density functional theory calculations," *Phys. Rev. B* **81**, 161201 (2010).
- <sup>39</sup>J. Lyons, A. Janotti, and C. V. de Walle, "The role of oxygen-related defects and hydrogen impurities in HfO<sub>2</sub> and ZrO<sub>2</sub>," in *Proceedings of the 17th Biennial International Insulating Films on Semiconductor Conference* [Microelectron. Eng. **88**, 1452–1456 (2011)].
- <sup>40</sup>M. Pe i c, F. P. G. Fengler, L. Larcher, A. Padovani, T. Schenk, E. D. Grimley, X. Sang, J. M. LeBeau, S. Slesazeck, U. Schroeder, and T. Mikolajick, "Physical mechanisms behind the field-cycling behavior of HfO<sub>2</sub>-based ferroelectric capacitors," *Adv. Funct. Mater.* **26**, 4601–4612 (2016).
- <sup>41</sup>R. C. Garvie, "The occurrence of metastable tetragonal zirconia as a crystallite size effect," *J. Phys. Chem.* **69**, 1238–1243 (1965).
- <sup>42</sup>E. D. Grimley, T. Schenk, X. Sang, M. Pe i c, U. Schroeder, T. Mikolajick, and J. M. LeBeau, "Structural changes underlying field-cycling phenomena in ferroelectric HfO<sub>2</sub> thin films," *Adv. Electron. Mater.* **2**, 1600173 (2016).
- <sup>43</sup>P. McIntyre, "Bulk and interfacial oxygen defects in HfO<sub>2</sub> gate dielectric stacks: A critical assessment," *ECS Trans.* **11**, 235–249 (2007).

# Impact of Four-Valent Doping on the Crystallographic Phase Formation for Ferroelectric HfO<sub>2</sub> from First-Principles: Implications for Ferroelectric Memory and Energy-Related Applications


Christopher Künneth, Robin Materlik, Max Falkowski, and Alfred Kersch  
ACS Appl. Nano Mater., vol. 1, no. 1, pp. 254–264, Jan. 2018.  
DOI: [10.1021/acsanm.7b00124](https://doi.org/10.1021/acsanm.7b00124)

Reprinted (adapted) with permission from ACS Applied Nano Materials. Copyright 2018 American Chemical Society.

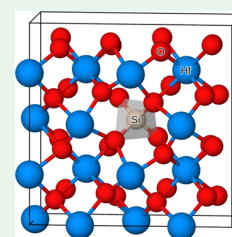
# Impact of Four-Valent Doping on the Crystallographic Phase Formation for Ferroelectric HfO<sub>2</sub> from First-Principles: Implications for Ferroelectric Memory and Energy-Related Applications

Christopher Künneth,\*<sup>ORCID</sup> Robin Materlik, Max Falkowski, and Alfred Kersch\*

Department of Applied Sciences and Mechatronics, Munich University of Applied Sciences, Lothstr. 34, D-80335 Munich, Germany

 Supporting Information

**ABSTRACT:** The ferroelectric properties of nanoscale silicon-doped HfO<sub>2</sub> promise a multitude of applications ranging from ferroelectric memory to energy-related applications. The reason for the unexpected behavior has not been clearly proven and presumably includes contributions from size effects and doping effects. Silicon incorporation in HfO<sub>2</sub> is investigated computationally by first-principles using different density functional theory (DFT) methods. Formation energies of interstitial and substitutional silicon in HfO<sub>2</sub> paired with and without an oxygen vacancy prove the substitutional defect as the most likely. Within the investigated concentration window up to 12.5 formula unit %, silicon doping alone is not sufficient to stabilize the polar and orthorhombic crystal phase (*p-o*-phase), which has been identified as the source of the ferroelectricity in HfO<sub>2</sub>. On the other hand, silicon incorporation is one of the strongest promoters of the *p-o*-phase and the tetragonal phase (*t*-phase) within the group of investigated dopants, confirming the experimental ferroelectric window. Aside from silicon, the favoring effects on the energy of other four-valent dopants, C, Ge, Ti, Sn, Zr, and Ce, are examined, revealing Ce as a very promising candidate. The evolution of the volume changes with increasing doping concentration of these four-valent dopants shows an inverse trend for Ce in comparison to silicon. To complement this study, the geometrical incorporation of the dopants in the host HfO<sub>2</sub> lattice was analyzed.



**KEYWORDS:** hafnium, thin film, silicon, doping, DFT, ferroelectricity

## 1. INTRODUCTION

In 2011, Böscke et al.<sup>1</sup> unveiled that silicon-doped HfO<sub>2</sub> thin films with a thickness of 10 nm exhibit ferroelectricity. Measurements of 2.6 f.u.% (formula unit, f.u. =  $n/3$  with  $n$  the number of atoms) silicon-doped HfO<sub>2</sub> showed a clear ferroelectric hysteresis. Starting at 4.3 f.u.%, the hysteresis starts to pinch, forming an antiferroelectric-like shape. At about 6 f.u.%, the ferroelectricity in silicon-doped HfO<sub>2</sub> transforms into paraelectricity. On the basis of grazing incidence X-ray diffraction (GIXRD) measurements, the polar and orthorhombic crystallographic phase *Pbc*2<sub>1</sub> (space group no. 29, *p-o*-phase) was proposed as the root of the ferroelectricity.<sup>1–3</sup> Aside from the *p-o*-phase, other important crystallographic phases could be identified to be present in HfO<sub>2</sub>: (a) the monoclinic *P*2<sub>1</sub>/*c* (space group no. 14, *m*-phase), (b) the tetragonal *P*4<sub>2</sub>/*nmc* (space group no. 137, *t*-phase), (c) the orthorhombic *Pbca* (space group no. 61, *o*-phase), and (d) the cubic *Fm* $\bar{3}$ *m* (space group no. 225, *c*-phase).<sup>2,4</sup> Before Böscke et al.'s finding, the effect of silicon doping on HfO<sub>2</sub> with more than 5 f.u.% was known to stabilize the *t*-phase and was applied in 50 nm HfSiON metal–insulator–semiconductor (MIS) dynamic random access memory (DRAM) trench capacitors.<sup>5</sup>

Ferroelectric silicon-doped HfO<sub>2</sub> may become of significant technological importance as can be seen in applications like the 28 nm ferroelectric field-effect transistor (FeFET) demonstrator.<sup>6</sup> Nonetheless, its material properties have not been researched satisfactorily. Recently, silicon-doped HfO<sub>2</sub> atomic

layer deposition (ALD) films for a film thickness of 36 nm were explored experimentally in a comprehensive study by Richter et al.,<sup>7</sup> varying the concentration from 2.2 to 8.3 f.u.%.<sup>8</sup> The maximum polarization was found at 4.2 f.u.%. For higher doping concentrations the hysteresis started to pinch, which was interpreted as an increasing *t*-phase fraction at zero electric field. However, higher electric fields can switch the *t*-phase back to the *p-o*-phase (field-induced ferroelectricity). In addition, Richter et al.<sup>7</sup> prepared a thickness series of 5–60 nm with 4.2 f.u.% silicon dopant concentration. They found the maximum remanent polarization at around 10 nm and a reduction with increasing thickness, vanishing at 60 nm. In all experiments, the ALD stack was sandwiched between TiN electrodes. Revolving scanning transmission electron microscopy (RevSTEM) revealed that the crystal phase close to the electrodes of grains in the *p-o*-phase is pinned to the *t*-phase. This implies the existence of a coherent interface.

Aside from silicon doping, the *p-o*-phase in HfO<sub>2</sub> has been stabilized with Al, Sr, Y, La, Gd, and Zr, but no successful stabilization with the four-valent dopants Ti, Sn, or Ge has been reported for ALD fabricated films. In physical vapor deposition (PVD) fabricated Ge-doped HfO<sub>2</sub> films, ferroelectricity could be found by Xu et al.<sup>9</sup> for a doping concentration from about 4.2

**Received:** October 31, 2017

**Accepted:** December 8, 2017

**Published:** December 8, 2017

to 18 f.u.%. Carbon is contained in ALD films on the level of a few f.u.%, and its effect as a stabilizer of the *t*-phase has been emphasized; however, the effect on the stabilization of the *p*-*o*-phase is only indirectly visible.<sup>10</sup> Other four-valent stabilizers of the *p*-*o*-phase have not been reported, although Ge- or Ti-doped ALD HfO<sub>2</sub> films have been produced finding some *t*-phase stabilization. From this it appears that silicon is the only four-valent dopant with a significant stabilization of the *p*-*o*-phase.

Computationally, the effects of the four-valent dopants C, Si, Ge, Ti, Sn, and Zr have been studied by Lee et al.<sup>11</sup> and Fischer et al.,<sup>12</sup> but only as a stabilizer of the *t*-phase, as the *p*-*o*-phase was not known at that time. Lee et al. explained the pronounced *t*-phase stabilization from silicon doping with the similarity of SiO<sub>4</sub> to the tetrahedral configuration in quartz, which seems energetically favorable. Fischer et al. correlated the energy gain from silicon doping with the ionic radius, representing the dopant size in the oxide environment. Furthermore, the absence of the *m*-phase was explained as an additional size effect.<sup>4,13</sup>

The only computational studies to explain the *p*-*o*-phase stabilization with dopants so far are Materlik et al.,<sup>14</sup> investigating Sr-doped HfO<sub>2</sub> as a single dopant in detail, and an extensive study by Batra et al.,<sup>15</sup> screening 40 dopants, but omitting small dopants like Si, Al, and C. Many of those large dopants are known from ceramic materials, where they are exploited for stabilization of a particular crystallographic phase. Because of the manufacturing process, those ceramic materials are typically larger in grain size than the nanoscaled ALD films<sup>16</sup> and are known to be ionically charge-compensated by an accompanying oxygen vacancy.<sup>17</sup> By calculating the formation energy of Sr-doped HfO<sub>2</sub>, Materlik et al.<sup>14</sup> found that the Sr defect with an associated vacancy does not stabilize the *p*-*o*-phase. On the other hand, only Sr doping without vacancies prefers the *p*-*o*-phase, which is conceivable in a nanoscale metal–insulator–metal (MIM) stack, where the Fermi level may adjust to reduce the charge occupation, and the remaining charge compensation could be provided by interface charges.<sup>18,19</sup> In accordance with experimental data, Sr was found to stabilize the *p*-*o*-phase in a concentration window below 5 f.u.% and the *t*-phase above that window. However, a destabilization mechanism for the *m*-phase had to be assumed. Batra et al.<sup>15</sup> investigated the stabilization of Ca, Sr, Ba, Y, La, and Gd paired with a vacancy in HfO<sub>2</sub> on the crystal phases for 3.125, 6.25, and 12.5 f.u.% doping concentrations, concluding that all dopants promote the stabilization of the *p*-*o*-phase, but doping alone can not stabilize the *p*-*o*-phase. Further mechanisms to favor the *p*-*o*-phase have been discussed, as there are surface and interface energy,<sup>4,13</sup> mechanical strain,<sup>4,20–22</sup> and electric field.<sup>4,21</sup>

It is evident that a model for dopant stabilization based solely on monocrystalline properties is incomplete. Care has to be taken when comparing computational results with experimental data. As monocrystalline, ferroelectric HfO<sub>2</sub> as such has not yet been found,<sup>23</sup> the properties of ALD or chemical solution-deposited (CSD) polycrystalline films with grain radii on the order of the film thickness are probably closer to a computational investigation than PVD produced film. Since the dissimilar production process for PVD fabricated films, e.g., involving higher kinetic energies than in ALD, the authors anticipate PVD films different from ALD films, containing different and more defects such as oxygen vacancies or enforced interstitial instead of substitutional incorporations. Therefore, the comprehensive investigation of PVD-prepared doped HfO<sub>2</sub>

by Xu et al.<sup>9</sup> may need additional considerations not included in this publication.

The purpose of this paper is to close the gap of computational studies on doped HfO<sub>2</sub>. First, different DFT methods, their associated energies, and volumes for substitutional silicon doping Si<sub>Hf</sub> are investigated, essentially choosing one method. Afterward, the formation energy and total energy differences with respect to the *m*-phase of a substitutional silicon Si<sub>Hf</sub>, oxygen vacancy V<sub>O</sub>, substitutional silicon paired with an oxygen vacancy Si<sub>Hf</sub>V<sub>O</sub>, and interstitial silicon Si<sub>I</sub> are calculated and analyzed. Moreover, we investigate the circumstances, stabilizing the *p*-*o*-phase of HfO<sub>2</sub> with silicon doping concentration in the known experimental concentration window. Finally, we turn to chemically similar four-valent dopants and perform energetic and structural computations to explore the capability of phase stabilization.

## 2. MATERIALS AND METHODS

DFT total energies in this publication were obtained with (i) the all-electron DFT code FHI-Aims,<sup>24–28</sup> which uses the numerical atom-centered basis function and (ii) the plane-wave-based pseudopotential code Abinit.<sup>29–31</sup> FHI-Aims results were obtained using the local density approximation (AIMS-LDA, PW<sup>32</sup> parametrization), generalized gradient approximation (AIMS-PBE, PBE<sup>33</sup> approximation), and Heyd–Scuseria–Ernzerhof<sup>34,35</sup> (AIMS-HSE06) with the mixing parameter  $\alpha = 0.25$  and  $\omega = 0.11a_0^{-1}$  for the exchange-correlation (XC) functional. In Abinit, only the local density approximation (LDA, PZ<sup>36</sup> parametrization) XC functional in combination with projected augmented wave (PAW) pseudopotentials (PP) from the PP library of ref 37 (GBRV) were used. The GBRV library contains a Hf PP for the Hf<sup>2+</sup> and Hf<sup>3+</sup> ionic configuration referred to as GBRV and GBRV\*, respectively.

A convergence study reveals that a *k*-point grid of 6 × 6 × 6 for 12 atoms, 3 × 6 × 6 for 24 atoms, 3 × 3 × 6 for 48 atoms, and 3 × 3 × 3 for 96 atoms is sufficient for all FHI-Aims and Abinit calculations with respect to energies. The electronic (ionic) force was converged until 1 × 10<sup>-3</sup> eV Å<sup>-1</sup> (1 × 10<sup>-4</sup> eV Å<sup>-1</sup>) with the tight basis set in the second tier for FHI-Aims and 5 × 10<sup>-6</sup> eV Å<sup>-1</sup> (5 × 10<sup>-5</sup> eV Å<sup>-1</sup>) for Abinit. The plane-wave and PAW cutoff for the Abinit calculations were 18 and 22 Ha, respectively. In charged supercells only ions were allowed to move, keeping the lattice vectors of the uncharged supercell. Vibrational frequency calculations for the entropy contribution to the free energy were carried out with the utility Phonopy<sup>38</sup> and Anaddb (included in Abinit) using finite displacements.

The smallest number of atoms to represent and maintain the symmetry of the *m*-, *t*-, *p*-*o*-, and *o*-phases (unit cell) is 12, 6, 12, and 24 atoms, respectively. Pure HfO<sub>2</sub> calculations for the *m*-, *t*- and *p*-*o*-phases were carried out in 12 atoms and for the *o*-phase in 24 atoms sized unit cells. For convenience only, the *t*-phase was calculated in 12 atoms. The 6.25 f.u.% (f.u. =  $n/3$  with  $n$  the number of atoms) doping was achieved by substituting one Hf with a dopant D<sub>Hf</sub> in a 48 atoms sized unit cell, which is exemplified for silicon in Figure 1. Since the 48 atoms sized unit cell can be created expanding the 12 atoms sized unit cell in the three distinct directions for the *m*-, *t*- and *p*-*o*-phases, all three choices were calculated, and the lowest energy was chosen. Consequently, in the case of the *o*-phase, the 24 atoms sized unit cell was expanded in two directions, and again, the lowest energy was chosen. In contrast for 3.125 f.u.% doping, the supercell was uniquely built with the multiplication of 2 × 2 × 2 of the 12 atoms sized cells and 2 × 2 × 1 of the 24 atoms unit cells. Doping concentrations in this publication are specified in f.u.%, which is in the case of metal substitution the same as cation % (cat.%) but differs from anion % (ani.%). As anion and cation doping are used simultaneously in graphs, f.u.% is used instead throughout the paper. Since FHI-Aims does not include symmetry considerations, all convergences were archived without symmetry constraints. To find the preferred oxygen vacancy positions in silicon-doped and pure HfO<sub>2</sub>, the energy of all symmetry-inequivalent positions was calculated. Finally, the vacancy position of the lowest

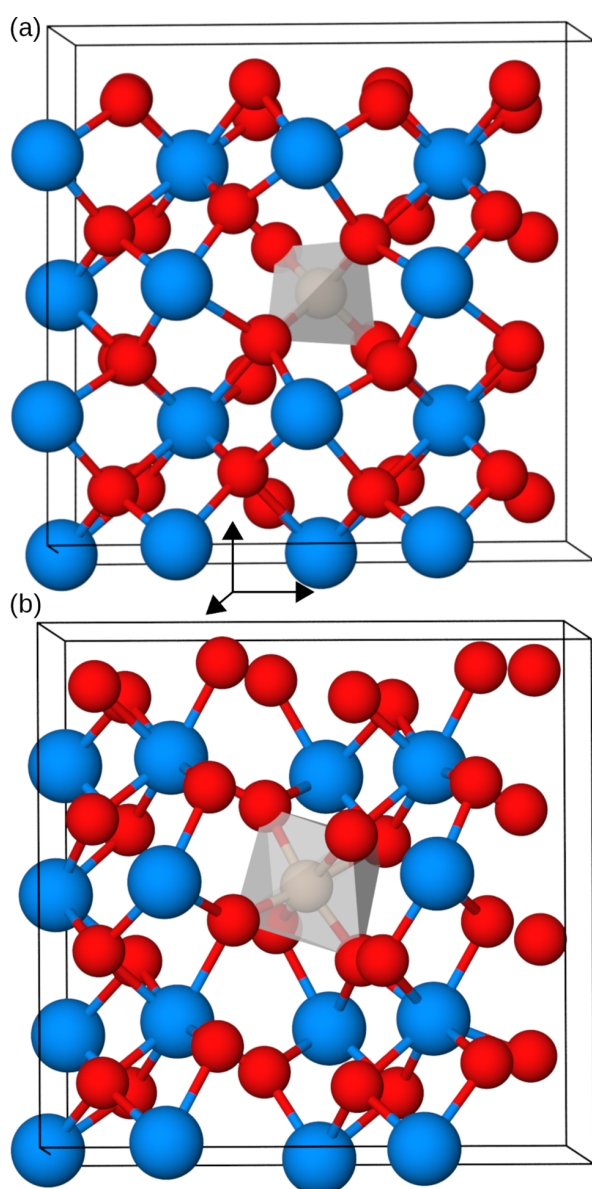


**Figure 1.** Atomic representations of the substitutional incorporations of the dopant into the host  $\text{HfO}_2$  crystal, exemplified for the (a)  $t$ -phase and (b)  $p$ - $o$ -phase. The gray polyhedron in part a illustrates the bonding tetrahedron for the  $t$ -phase and in part b the bonding octahedron for the  $p$ - $o$ -phase in silicon-doped  $\text{HfO}_2$ .

energy was chosen. The final lattice constants and band gaps are tabulated in the Supporting Information in Table S1.

The formation energy  $E_f^\zeta$  for a phase  $\zeta \in \{m, o, p-o, t\}$  is calculated according to<sup>39</sup>

$$E_f^\zeta[X^q] = E_{\text{tot}}^\zeta[X^q] - E_{\text{tot}}^\zeta[\text{pure}^0] - \sum_i n_i \mu_i + q(E_F + E_{\text{VBM}}^\zeta[\text{pure}^0] + \Delta V^\zeta[X^0]) + E_{\text{corr}}^\zeta[X^q] \quad (1)$$

with  $E_{\text{tot}}^\zeta$  the total energy of phase  $\zeta$ ,  $n_i$  the numbers of impurities,  $\mu_i$  the chemical potential of the impurity  $i$ ,  $E_F$  the Fermi level referenced to the energy of the valence band maximum  $E_{\text{VBM}}^\zeta$ ,  $\Delta V^\zeta$  the potential alignment,  $E_{\text{corr}}^\zeta$  the charge correction due to finite size of the unit cell, and  $X \in \{\text{V}_O, \text{Si}_{\text{Hf}}, \text{Si}_{\text{Hf}}\text{V}_O\}$  the defect. Calculations for charged

structures were carried out for the charges  $q = -3, \dots, +3$  for all three defects with the lattice fixed to the uncharged structure. For  $X \in \{\text{Si}_i, \text{C}_{\text{Hf}}, \text{Ge}_{\text{Hf}}, \text{Ti}_{\text{Hf}}, \text{Sn}_{\text{Hf}}, \text{Zr}_{\text{Hf}}, \text{Ce}_{\text{Hf}}\}$  only calculations for charge  $q = 0$  were carried out.

The chemical potentials of  $\text{V}_O$ ,  $\text{Si}_{\text{Hf}}$  and  $\text{Si}_{\text{Hf}}\text{V}_O$  were  $\sum_i n_i \mu_i = -\mu_O$ ,  $\sum_i n_i \mu_i = -\mu_{\text{Si}} + \mu_{\text{Hf}}$  and  $\sum_i n_i \mu_i = -\mu_{\text{Si}} + \mu_{\text{Hf}} - \mu_O$ , respectively. Ferroelectric  $\text{HfO}_2$  is frequently deposited on TiN electrodes, which was suggested to exist in a partially oxidized state.<sup>7,40,41</sup> Therefore, under oxygen-deficient conditions  $\mu_O$  is calculated from  $\text{TiO}_2$  ( $\mu_O^{\text{TiO}_2}$ ) in anatase structure, and under oxygen-rich conditions from  $\text{O}_2$  ( $\mu_O^{\text{O}_2}$ ). Aside from anatase  $\text{TiO}_2$ , the chemical potential of rutile  $\text{TiO}_2$  was calculated. However, the values of both chemical potentials are very similar and do not show visible differences in the formation energies.  $\mu_{\text{Hf}}$  was calculated using  $\alpha$ -Hf. The chemical potentials  $\mu_C$ ,  $\mu_{\text{Ge}}$ ,  $\mu_{\text{Ti}}$ ,  $\mu_{\text{Sn}}$ ,  $\mu_{\text{Zr}}$  and  $\mu_{\text{Ce}}$  were calculated from diamond C, diamond Ge, hexagonal ( $P6_3/mmc$ , no. 194) Ti,  $\beta$ -Sn, hexagonal ( $P6_3/mmc$ , no. 194) Zr, and cubic ( $Fm\bar{3}m$ , no. 225) Ce, respectively. Figures of the atomic structures in this publication are produced with Ovito.<sup>42</sup> If  $q$  is omitted in the notation, the charge is set to zero.

### 3. RESULTS

**3.1. Si Doping with Different DFT Methods.** For the choice of a consistent basis for further calculations, different DFT methods with different XC functionals were first evaluated. Figure 2 compiles the energy differences in part a, with respect to the  $m$ -phase, and the associated volume changes in part b, for the five different DFT methods. All methods consistently show the favoring of the  $p$ - $o$ - and  $t$ -phases with increasing silicon concentration. Assuming a linear interpolation between the values of the calculated doping concentrations of the different DFT methods in Figure 2, between 4.2 and 5.9 f.u.% Si doping concentration, the  $t$ -phase becomes lower in energy than the  $p$ - $o$ -phase for all DFT methods. Moreover, no method shows the  $p$ - $o$ -phase to be the lowest in energy for any concentration. Therefore, silicon doping is not a mechanism to exclude either the  $m$ - or  $o$ -phase as the thermodynamically most and second most favorable crystal structures of the monocrystalline material. Aside from doping, a high negative entropic influence on the energy differences for the  $t$ -phase and a smaller one on the  $p$ - $o$ -phase from temperature is expected. Entropy calculations are done for three DFT methods for pure  $\text{HfO}_2$ , and the energy contributions from entropy for  $T = 300$  K are listed in Table 1. Since entropy calculations for doped  $\text{HfO}_2$  are very time-consuming (doping breaks the symmetries), the calculation is only performed for substitutional Si doping. The result indicates that the Gibbs energy is not significantly affected at 6.25 f.u.% Si doping. However, the additional energy contributions from entropy do not alter the energy picture in general and particularly leave the trends unaffected. All further calculations in this publication are carried out using AIMS-LDA since the volume change seems more realistic than that of AIMS-GGA. AIMS was chosen over ABINIT since it uses a more precise all-electron approach and reveals consistent results also for other related issues from the experience of the authors.

In addition to the energy effect, silicon incorporation causes a change of the volume. The volumes for all DFT methods in Figure 2b decrease after silicon incorporation. Only the trend of the  $t$ -phase with AIMS-PBE increases. Since silicon is smaller than Hf, a decreasing volume is believed to be the more reasonable trend. Although the  $t$ -phase data point was carefully checked, no error in the calculation or the analysis could be found. Experimentally, Zhao et al.<sup>43</sup> precisely measured the volume change by silicon doping in  $\text{HfO}_2$  ceramics. Interestingly, in this study, only the  $m$ -phase was found up to a doping

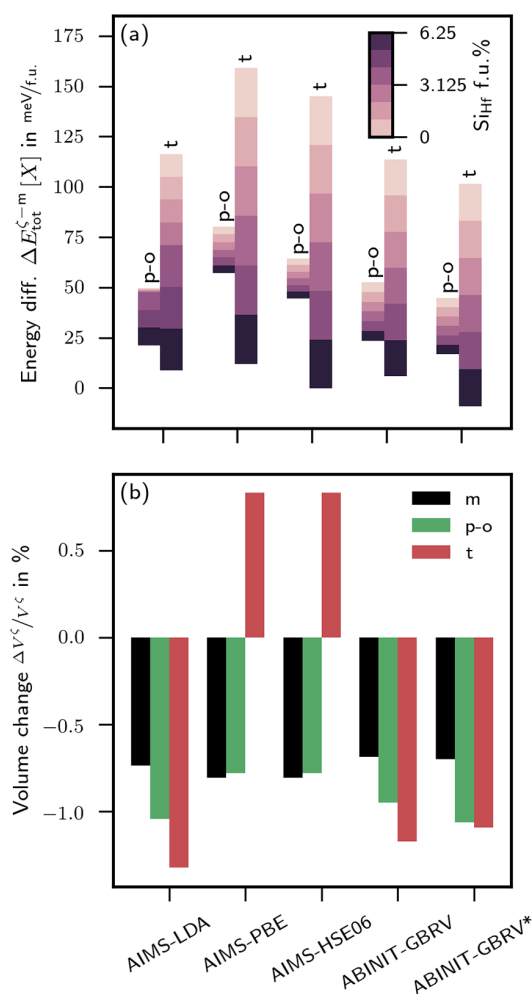


**Figure 2.** (a) Energy differences with respect to the *m*-phase for five different DFT methods up to a doping concentration of 6.25 f.u.% for silicon-doped HfO<sub>2</sub>. (b) Associated volume change with respect to undoped HfO<sub>2</sub>. Except for AIMS-LDA, the values between pure and 6.25 f.u.% doping concentration were linearly interpolated. In the case of AIMS-LDA, between 0 and 3.125 f.u.%, and 3.125 and 6.25 f.u.%, doping concentration was linearly interpolated. The coordinates and lattice parameters for HSE06 calculations were fixed to PBE.

limit of 9 f.u.% silicon, accompanied by no significant change in the unit cell volume.

Figure 2 discusses the question, how capable are currently used XC functionals in reflecting the crystallographic phase stability, which requires relative total energy values on the level of a few meV f.u.<sup>-1</sup>. For undoped HfO<sub>2</sub> and ZrO<sub>2</sub>, several comparisons between LDA and PBE XC functionals<sup>44,45</sup> (local) and also more recently hybrid XC functionals<sup>46</sup> (nonlocal) were carried out. The results show generally larger energy differences between the phases for PBE than for LDA, but maintain the energetic order and do not contradict the structural data. HSE06 hybrid functional calculations from Barabash et al.<sup>46</sup> give values energetically between PBE and LDA but closer to PBE, which is similar to our calculations. Total energy differences have been studied with HSE06 in TiO<sub>2</sub>.<sup>47</sup> Although, the structural results were superior with the local functionals, the anatase phase turned out to be lower than rutile, contradicting the experiment. Either the ground state is obscured from further effects, similar to polycrystalline HfO<sub>2</sub>, or better total energy results are not

guaranteed with the HSE06 functional. The fraction of the exact exchange in the method is optimized to match the band gap. AIMS-HSE06 in Figure 2 represents single point calculations, using the coordinates and lattice constants of AIMS-PBE.

**3.2. Formation Energy of Si-Related Defects.** The substitutional defect structure Si<sub>Hf</sub> is created most likely when silicon is incorporated in the HfO<sub>2</sub> lattice. To substantiate this statement, we have calculated the formation energy for the Si<sub>Hf</sub>, Si<sub>Hf</sub>V<sub>O</sub>, V<sub>O</sub>, and Si<sub>i</sub> defect in all the crystal phases for two oxygen partial pressures, shown in Figure 3. For oxygen-deficient (poor) conditions, the chemical potential with TiO<sub>2</sub> (solid lines) was used and for oxygen-rich conditions with O<sub>2</sub> (dashed lines). TiO<sub>2</sub> was chosen since it corresponds to a typical, oxidized electrode material in HfO<sub>2</sub> thin films. O<sub>2</sub> is a typical precursor in the ALD process for such films. In Figure 3, only the charge state *q* with the lowest formation energy is depicted. Therefore, the kinks indicate the thermodynamic charge transition levels.

A comparison of the oxygen-deficient with the oxygen-rich case for all subplots in Figure 3 shows that the formation energies of V<sub>O</sub> and Si<sub>Hf</sub>V<sub>O</sub> are shifted by a constant value of  $\mu_{\text{O}}^{\text{TiO}_2} - \mu_{\text{O}}^{\text{O}_2} = 5.6$  eV, leaving the Si<sub>Hf</sub> unaffected. In the oxygen-rich case ( $\mu_{\text{O}}^{\text{O}_2}$ ), the formations of the V<sub>O</sub> and Si<sub>Hf</sub>V<sub>O</sub> are both unfavorable for the Fermi level higher than  $\approx 0.7$  eV in comparison with Si<sub>Hf</sub> for all phases. Assuming that the  $\mu_{\text{O}}^{\text{O}_2}$  chemical potential is close to the fabrication conditions of the thin films, silicon doping preferentially creates Si<sub>Hf</sub>.

After the production process, the oxygen partial pressure is determined by  $\mu_{\text{O}}^{\text{TiO}_2}$  favoring the creation of V<sub>O</sub> and Si<sub>Hf</sub>V<sub>O</sub> defects with the necessary formation energy dependent on the Fermi level. The hafniums in HfO<sub>2</sub> are known to be stronger bonded to the surrounding atoms than the oxygens (O),<sup>48,49</sup> making the hafniums immobile in comparison to the oxygens. The newly created and mobile V<sub>O</sub> defects can recombine with the already present immobile Si<sub>Hf</sub> defects to Si<sub>Hf</sub>V<sub>O</sub>, releasing an energy of 0.5 (*m*-), 0.6 (*o*-), 0.28 (*p-o*-), and 0.27 (*t*-phase) eV for the reaction Si<sub>Hf</sub> + V<sub>O</sub> → Si<sub>Hf</sub>V<sub>O</sub> (formation energies of only *q* = 0 were considered here). In comparison, the energy release for the analogous reaction in Sr-doped HfO<sub>2</sub> is 2.4 eV for the *p-o*-phase, which is approximately an order of magnitude higher than that for silicon-doped HfO<sub>2</sub>.

Aside from the formation energies for the Si<sub>Hf</sub>, V<sub>O</sub>, and Si<sub>Hf</sub>V<sub>O</sub> defects, formation energies for silicon interstitials Si<sub>i</sub> were carried out only for the charge *q* = 0. Placing the Si<sub>i</sub> in all symmetry-inequivalent polyhedra spanned by adjacent atoms for each of the crystal phases, the lowest Si<sub>i</sub> formation energies were found to be 4.6, 5.6, 4.3, and 4.4 eV for the *m*-, *o*-, *p-o*- and *t*-phases, respectively. The formation energy if Si<sub>i</sub> is indicated by the black dots in Figure 3. Consistently, the formation energies of Si<sub>i</sub> are higher than for Si<sub>Hf</sub> making them more unlikely.

In addition, the subplots of Figure 3 evince charge transition levels at approximately the same Fermi levels for all phases. Except for Si<sub>Hf</sub> all lines have two transition levels, indicating that Si<sub>Hf</sub> introduces a transition level in a distance of approximately 4 eV from the valence band edge. It should be noted that those levels are close to the conduction band edge predicted by LDA and the remaining difference can be due to uncertainties of the chosen DFT XC functional. The same arguments hold for the V<sub>O</sub> defect, which also introduces a level very close to the level of Si<sub>Hf</sub> at about 4 eV with respect to the valence band edge. The band gaps of the calculations can be found in the Supporting Information in Table S1. Since the deep charge transition level

**Table 1.** Energy Differences<sup>a</sup> Relative to *m*-Phase and Volume Changes Relative to the Undoped Structure for Different Used DFT Methods Are Presented

<i>X</i>	Method	$\Delta E_{\text{tot}}^{\zeta-m}$			$\Delta V^{\zeta}/V^{\zeta}$			
		<i>o</i> (meV f.u. <sup>-1</sup> )	<i>p-o</i> (meV f.u. <sup>-1</sup> )	<i>t</i> (meV f.u. <sup>-1</sup> )	<i>m</i> (%)	<i>o</i> (%)	<i>p-o</i> (%)	<i>t</i> (%)
pure	AIMS-LDA	28.1 (27.7)	49.5 (48.8)	115.8 (99.4)	0	0	0	0
Si <sub>Hf</sub>	AIMS-LDA	18.5 (16.4)	21.1 (19.7)	8.7 (-0.8)	-0.74	-1.15	-1.04	-1.33
V <sub>O</sub>	AIMS-LDA	30.0	40.1	104.0	1.74	1.87	1.71	1.71
Si <sub>Hf</sub> V <sub>O</sub>	AIMS-LDA	13.5	25.5	9.1	2.80	1.61	-0.22	0.85
Si <sub>i</sub>	AIMS-LDA	12.4	109.8	93.8	2.15	-0.61	2.43	4.32
pure	AIMS-PBE	28.4	80.0 (78.9)	158.9 (135.5)	0	0	0	0
Si <sub>Hf</sub>	AIMS-PBE	22.3	57.0	0.0	-0.81	-0.96	-0.78	0.83
pure	AIMS-HSE06	64.0	145.0	0	0	0	0	0
Si <sub>Hf</sub>	AIMS-HSE06	44.4	0.0	-0.81	-0.78	0.83		
pure	GBRV	27.0	52.2 (52.2)	113.6 (93.0)	0	0	0	0
Si <sub>Hf</sub>	GBRV	23.4	6.0	-0.69	-0.95	-1.18		
pure	GBRV*	44.5	101.4	0	0	0	0	0
Si <sub>Hf</sub>	GBRV*	16.8	-9.0	-0.70	-1.06	-1.10		

<sup>a</sup>Silicon and vacancy doping are both for 6.25 f.u.%. Values in parentheses are the energies including the vibrational entropy contribution from phonon modes for  $T = 300$  K.  $\Delta E_{\text{tot}}^{\zeta-m} = E_{\text{tot}}^{\zeta}[X] - E_{\text{tot}}^m[X]$  and  $\Delta V^{\zeta}/V^{\zeta} = (V^{\zeta}[X] - V^{\zeta}[\text{pure}])/V^{\zeta}[\text{pure}]$ .

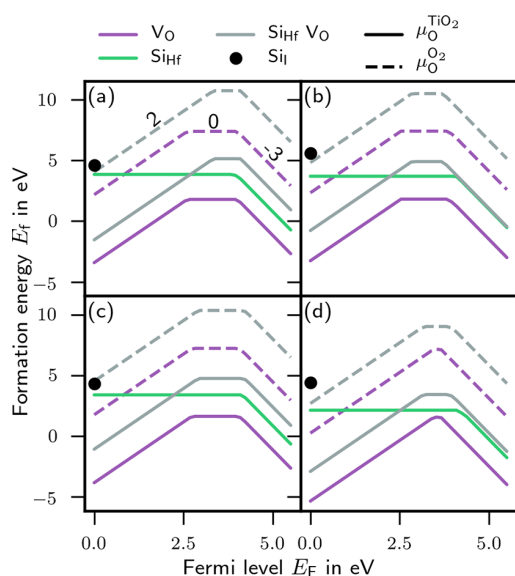


**Figure 3.** (a–d) Formation energy for V<sub>O</sub>, Si<sub>Hf</sub> and Si<sub>Hf</sub>V<sub>O</sub> against the Fermi level for the *m*-, *o*-, *p-o*-, and *t*-phases. The used energies were taken from 6.25 f.u.% doping. The small numbers indicate the charge state *q* of the defect and the black dots the formation energy of interstitial silicon Si<sub>i</sub>.

from +2 to 0 at about 2.5 eV is only present for Si<sub>Hf</sub>V<sub>O</sub> and V<sub>O</sub>, the level must be introduced by the vacancy. Corrêa et al.<sup>19</sup>

We conclude that the substitutional incorporation of silicon Si<sub>Hf</sub> is favored for all phases. Those defects are uncharged and do not introduce defect levels in the band gap. Next likely is the creation of oxygen vacancies V<sub>O</sub> under operating condition. This defect may combine with Si<sub>Hf</sub> to create Si<sub>Hf</sub>V<sub>O</sub>.

The impact of the discussed defects on the phase stability for 6.25 f.u.% is shown in Figure 4. The stabilization of the *t*- and *p-o*-phases with Si<sub>Hf</sub> is identical with the values shown in Figure 2 (a) for AIMS-LDA. The vacancy V<sub>O</sub> introduces a small stabilization effect, which can be neglected in comparison to the Si<sub>Hf</sub> defect. The energy change of the phases due to incorporation of Si<sub>Hf</sub>V<sub>O</sub> almost matches the magnitude of Si<sub>Hf</sub>. On the other hand, silicon interstitials Si<sub>i</sub> promote the

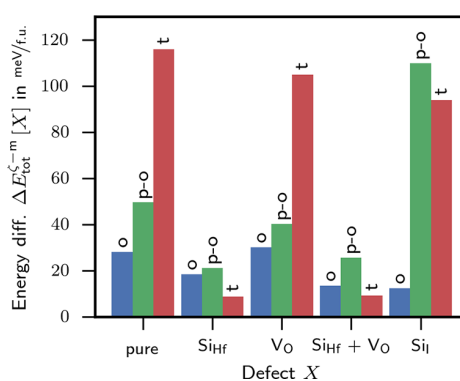


**Figure 4.** Total energy differences to the *m*-phase for no defect (pure), Si<sub>Hf</sub>, Si<sub>Hf</sub>V<sub>O</sub>, V<sub>O</sub> and Si<sub>i</sub> for a silicon or vacancy concentration of 6.25 f.u. %.

destabilization of the *p-o*-phase and a slight stabilization of the *t*-phase. Altogether, the phase stabilization is affected by silicon-related defects in HfO<sub>2</sub>, but up to 6.25 f.u.% the *p-o*-phase is not shifted to the ground state.

**3.3. Si doping concentration.** On the basis of the formation energies, it was concluded that the Si<sub>Hf</sub> defect is the most likely. We now focus on the impact of Si<sub>Hf</sub> on the phase stability depending on its concentration. Different doping concentrations were modeled by substituting one metal with one silicon for differently sized supercells. All the metal positions in our crystallographic phases are symmetry equivalent. Substitution of one atom out of 96 atoms gives 3.125 f.u.%, one out of 48 gives 6.25 f.u.%, and one out of 12 gives 12.5 f.u.%.

The supercell of 48 atoms can be created by expanding the 12 atomic unit cell by  $2 \times 2 \times 1$ ,  $2 \times 1 \times 2$ , and  $1 \times 2 \times 2$ , except for the *o*-phase (smallest unit cell has 24 atoms), in which only two meaningful directions are available. Since the energies of these structures showed a significant difference, the structures with the lowest energy for all phases were selected. The *c*-phase proved to be unstable in all doping concentrations and supercells and is therefore excluded in the discussion.

The energies for all phases for the three distinct silicon doping concentrations are displayed in Figure 5. They clearly show the *t*-phase as the ground state for a doping concentration larger



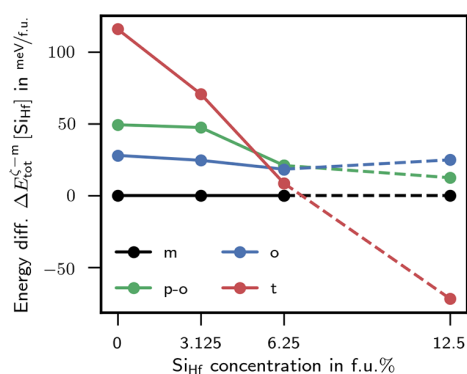


**Figure 5.** Energy difference with respect to the *m*-phase for different  $\text{Si}_{\text{Hf}}$  concentrations. The atom positions and the lattice parameters of the calculations at 12.5 f.u.% doping concentration show a significant difference to the actual symmetry of the phase (dashed line).

than 7 f.u.%. Assuming that the *m*-phase is eliminated by the size effect as discussed previously, the transition to the *t*-phase is determined from the intersection with the *p*-*o* phase at around 5.7 f.u.%. For lower concentration, the phase with the lowest energy is the high-pressure *o*-phase. In general, to achieve a stabilization in a particular concentration window of the *p*-*o* phase, either we have to assume a destabilization mechanism for the *o*-phase similar to the *m*-phase, or the phase transformations must be prevented because of a high barrier. The *o*-phase energy difference seems unaffected by silicon doping.

A further result concerns the linearity of the energy with the silicon concentration, which is obviously not fully realized, especially for the *p*-*o* phase. Because of periodic boundary conditions, the 48 atomic supercells require one crystallographic axis, where two silicon atoms are closer in one direction than the others. Another supercell to model 6.25 f.u.% doping would be substituting two atoms out of 96 atoms. Such supercells would enable the modeling of the silicon-to-silicon attraction and repulsion, and their influence on the total energy. However, the systematic investigation of the silicon–silicon (or more general dopant–dopant) interaction is computationally very time-consuming. We will report about this effect in a further publication. Regarding these nonlinear effects, the results in Figure 5 for a doping concentration of 12.5 f.u.% should be interpreted carefully.

**3.4. Other Four-Valent Dopants.** After studying the effect of the silicon-related defects and doping concentration on the crystallographic phase formation as a prototype system, we elaborated on the effects of other four-valent dopants D. C, Ge,

and Sn from the carbon group and Ti and Zr from the titanium group are selected; furthermore, Ce from the lanthanides is selected because it has a stable +4 oxidation state. On the basis of the analysis of the silicon defect, we limited our investigation to substitutional defects on the hafnium site  $\text{D}_{\text{Hf}}$ .

Figure 6 shows the evolution of the energy differences with respect to the *m*-phase from pure  $\text{HfO}_2$  to 6.25 f.u.% doping concentration. Although a favoring effect for some dopants on the *p*-*o* phase is evident, none of the investigated dopants alone shift the *p*-*o* phase to the lowest energy. For a  $\text{HfO}_2$  thin film exhibiting ferroelectricity, a destabilization mechanism for the *m*- and *o*-phases has to be assumed, promoting the *p*-*o* phase to the lowest in energy. Possible destabilization mechanisms have been discussed in the literature in refs 4,13, and 50. Upon comparison of the evolution of the *o*-phase in all seven subplots in Figure 6, it can be concluded that the *o*-phase is insensitive to doping. In addition, the *p*-*o* phase is still only a little sensitive to doping but responding, for Si and Ce. By contrast, the *t*-phase sensitivity is high, especially in the case of C, Si, Ge, and Ce.

Several attempts were made to find a simple relation between a geometrical argument due to the dopant incorporation and total or formation energies, as suggested experimentally by Starschich and Böttger<sup>51</sup> for the remanent polarization and the ionic radii, and computationally by Batra et al.<sup>15</sup> for the DFT energy differences and the ionic radii. However, none of the investigated correlations between the energy difference, volume, Shannon radius, or coordination number of the polyhedron of the dopants rise to the level of causation in the view of the authors. The corresponding correlation plots can be found in the Supporting Information in Figures S1–S3. Since a causation of the energy and a geometrical property of the dopant were not found, it can be concluded that the major effect on the energy differences is more of a chemical nature.

Table 2 collects the results of the energy difference between a phase  $\zeta$  and the *m*-phase with respect to the undoped energy difference as

$$\begin{aligned} \Delta E_{\text{tot}}^{\zeta-m}[\text{D}_{\text{Hf}} - \text{pure}] &= \Delta E_{\text{tot}}^{\zeta-m}[\text{D}_{\text{Hf}}] - \Delta E_{\text{tot}}^{\zeta-m}[\text{pure}] \\ &= (E_{\text{tot}}^{\zeta}[\text{D}_{\text{Hf}}] - E_{\text{tot}}^m[\text{D}_{\text{Hf}}]) - (E_{\text{tot}}^{\zeta}[\text{pure}] - E_{\text{tot}}^m[\text{pure}]) \end{aligned} \quad (2)$$

Negative values of  $\Delta E_{\text{tot}}^{\zeta-m}[\text{D}_{\text{Hf}} - \text{pure}]$  stabilize and positive values destabilize the corresponding crystal phase because of doping. Silicon with a value of  $-28.3 \text{ meV f.u.}^{-1}$  at 6.25 f.u.% is by far the best facilitator of the *p*-*o* phase in Figure 6, but simultaneously the *t*-phase is preferred by  $-107.3 \text{ meV f.u.}^{-1}$ ,

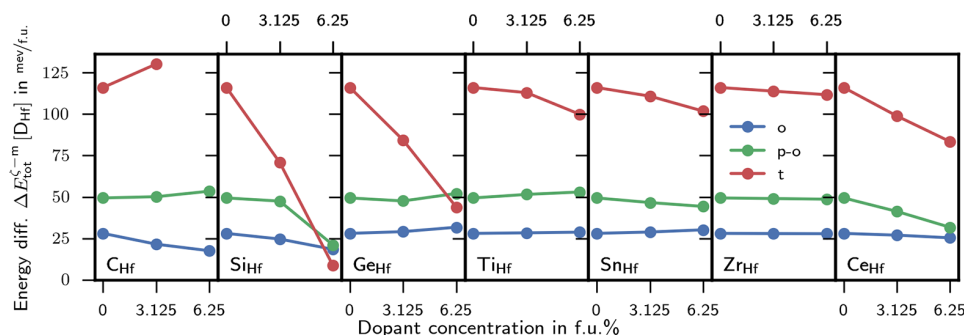


**Figure 6.** Evolution of the energy differences for different dopants with respect to the *m*-phase with increasing doping concentration.

**Table 2.** Volume Change  $\Delta V^{\zeta}/V^{\zeta}$  with Respect to the Host Crystal, and the Energy Difference  $\Delta E_{\text{tot}}^{\zeta-m}[\text{D}_{\text{Hf}} - \text{pure}]$  with Respect to the Undoped  $m$ -Phase of the Defects  $\text{D}_{\text{Hf}}$  for 3.125 f.u.% (6.25 f.u.%) Doping

D	$r_c^a$ (pm)	$\Delta V^{\zeta}/V^{\zeta}$				$\Delta E_{\text{tot}}^{\zeta-m}[\text{D}_{\text{Hf}} - \text{pure}]$		
		$m$ (%)	$o$ (%)	$p$ - $o$ (%)	$t$ (%)	$o$ (meV f.u. <sup>-1</sup> )	$p$ - $o$ (meV f.u. <sup>-1</sup> )	$t$ (meV f.u. <sup>-1</sup> )
C	29	0.3 (0.2)	0.2 (0.1)	0.2 (0.1)	-0.8 (-)	-6.5 (-10.5)	0.7 (4.1)	14.2 (-)
Si	40	-0.8 (-1.0)	-0.9 (-1.5)	-0.5 (-1.3)	-0.6 (-1.7)	-3.4 (-9.6)	-1.9 (-28.3)	-45.2 (-107.3)
Ge	53	-0.4 (-0.8)	-0.7 (-1.3)	-0.2 (-0.3)	-0.4 (-1.0)	1.1 (3.7)	-1.8 (2.7)	-31.7 (-72.2)
Ti	56	-0.6 (-1.3)	-0.7 (-1.4)	-0.6 (-1.2)	-0.3 (-0.8)	0.3 (0.8)	2.1 (3.6)	-3.1 (-16.2)
Sn	69	0.1 (0.2)	0.1 (0.1)	0.1 (0.2)	0.2 (0.3)	0.8 (2.1)	-2.8 (-5.1)	-5.2 (-14.2)
Zr	98	0.1 (0.2)	0.1 (0.2)	0.1 (0.2)	0.0 (0.1)	-0.1 (-0.2)	-0.4 (-0.7)	-2.2 (-4.3)
Ce	111	1.0 (1.9)	1.0 (2.0)	1.0 (1.9)	0.8 (1.6)	-1.1 (-2.7)	-8.1 (-17.7)	-17.2 (-32.6)

<sup>a</sup>The crystal radius  $r_c$  is taken from ref 52 for the respective dopant D and coordination number of the  $t$ -phase.

causing the narrow ferroelectric concentration window observed in experiments. Aside from silicon, Ce on the second rank, favors the  $p$ - $o$ -phase by  $-17.7 \text{ meV f.u.}^{-1}$  and the  $t$ -phase by  $-32.6 \text{ meV f.u.}^{-1}$  with a much better  $p$ - $o$ - to  $t$ -phase ratio of 0.54 in comparison to silicon with 0.26. This probably opens a wide concentration window for the  $p$ - $o$ -phase for Ce doping. Sn has a similar, but much smaller, capability to favor the  $p$ - $o$ -phase and the  $t$ -phase. The marginal support of Zr for the  $p$ - $o$ -phase is amplified by the excellent solubility in  $\text{HfO}_2$  up to pure  $\text{ZrO}_2$ . C, Ge, and Ti do not support the  $p$ - $o$ -phase but only the  $t$ -phase.

The track of the volume change of the four-valent dopants with increasing concentration is illustrated in Figure 7. First, the trend of all the crystal phases for each dopant exhibits the same volume evolution with increasing dopant concentration. This unit cell volume evolution was correlated with the Shannon radii of ref 52, but no simple relation could be found for both small and large ions. Only for large ions, the volume increases with the ion radius (see the Supporting Information, Figure S1). The  $m$ - and  $o$ -phases have almost the same absolute volume, which is about 5% bigger than the volume of the  $p$ - $o$ - and  $t$ -phases. Furthermore, the volumes are systematically smaller than experimentally measured volumes, confirming the LDA paradigm to always predict smaller volumes. Following the argumentation of Clima et al.<sup>53</sup> that the volume of the dopant is inversely proportional to the coercive field, necessary for ferroelectric switching, Ce would give rise to the lowest and silicon the highest coercive field in this set of dopants. Volume changes with respect to the undoped phase for the different dopants are provided in Table 2.

In addition, the volume change provides an estimate of the dopant stress exerted to the host crystal. The large volume change of silicon indicates a large force from silicon on the host lattice. For the smaller carbon, the binding in the host crystal is

incomplete with smaller forces and less volume change. The arrangement is chosen from left to right in increasing crystal radii according to ref 52. Apparently, a general trend in Figure 7 is that, with increasing radii, the volume switch from decreasing to increasing crosses zero between Ti and Sn, which is close to the radius of Hf with 83 pm according to ref 52. Although an energy difference to volume correlation is suggested by Figures 6 and 7, no generally valid relation could be found. However, we included the correlations in the Supporting Information in Figures S1–S3. It should be kept in mind that the deformation energy of the host crystal, calculated from the volume change and modulus of compressibility, is on the order of  $1 \text{ meV f.u.}^{-1}$ . Therefore, only a fraction of the energy is introduced into the system by the energy of formation.

The formation energies for  $q = 0$  charged and 3.125 f.u.% doped unit cells are compiled in a bar plot in Figure 8. The

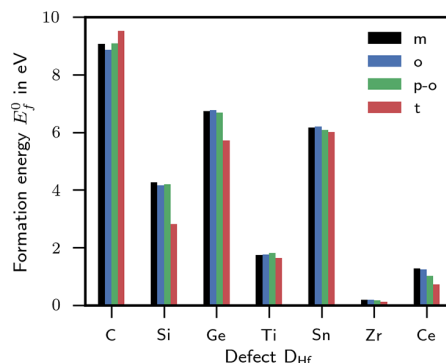


**Figure 8.** Formation energies for the incorporation of different dopants for charge  $q = 0$  for 3.125 f.u.% doping concentration.

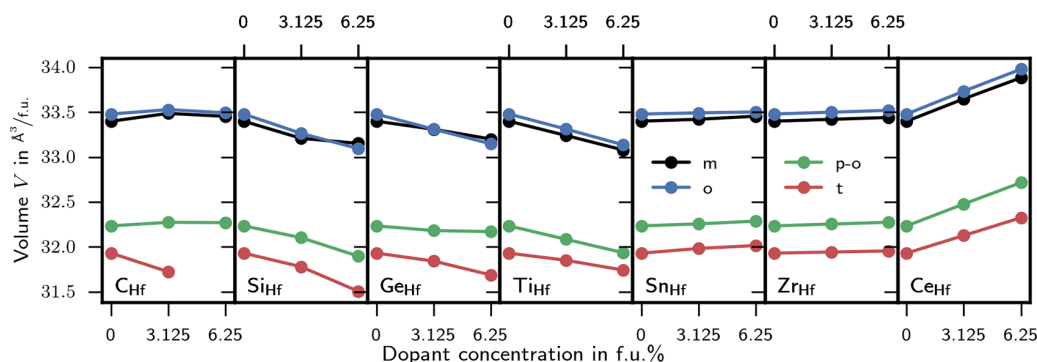


**Figure 7.** Evolution of the volumes of the different phases with increasing doping concentration for the different dopants.

energies were calculated using eq 1 and the chemical potentials from the metals for  $q = 0$ . The energies are tabulated in Table 3.

**Table 3. Formation Energy  $E_f^{\text{Hf}}[D^0]$  of the Defects  $D_{\text{Hf}}$  for 3.125 f.u.% (6.25 f.u.%)**

D	$r_c^a$ (pm)	$E_f^{\text{Hf}}[D^0]$			
		$m$ (eV)	$o$ (eV)	$p-o$ (eV)	$t$ (eV)
C	29	9.1 (9.4)	8.9 (9.2)	9.1 (9.4)	9.5 (–)
Si	40	4.3 (4.0)	4.2 (3.9)	4.2 (3.6)	2.8 (2.3)
Ge	53	6.7 (6.5)	6.8 (6.6)	6.7 (6.6)	5.7 (5.4)
Ti	56	1.7 (1.7)	1.8 (1.7)	1.8 (1.8)	1.6 (1.5)
Sn	69	6.2 (6.2)	6.2 (6.2)	6.1 (6.1)	6.0 (5.9)
Zr	98	0.2 (0.2)	0.2 (0.2)	0.2 (0.2)	0.1 (0.1)
Ce	111	1.3 (1.3)	1.2 (1.2)	1.0 (1.0)	0.7 (0.7)

<sup>a</sup>The crystal radius  $r_c$  is taken from ref 52 for the respective dopant D and coordination number of the  $t$ -phase.

The dopants are arranged in the same increasing order of crystal radii as in the previous figures and tables, which immediately demonstrates that the relation between the dopant size and defect formation energy is not linear. The formation energy of C is the highest, and that of Zr is close to zero, explaining the good solubility of Zr in HfO<sub>2</sub> until pure ZrO<sub>2</sub>. Consequently, the formation energy of Ce, which is the second lowest, may indicate a similarly good solubility in HfO<sub>2</sub>.

In this section, total energy differences of the  $o$ -,  $p-o$ -, and  $t$ -phases were presented and analyzed for the dopants C, Si, Ge, Ti, Sn, Zr, and Ce, concluding that none of the dopants alone are capable of promoting the  $p-o$ -phase to the ground state. Aside from silicon, which favors the  $p-o$ -phase but much more the  $t$ -phase, Ce is a promising candidate for doping since the  $t$ -phase is less favored than with Si. Subsequently, the volume changes due to the dopants are compared. Following the argumentation from Clima et al.<sup>53</sup> that the volume is inversely proportional to the coercive field, Ce-doped HfO<sub>2</sub> should exhibit ferroelectricity with a small coercive field. Finally, the formation energy of the dopants was investigated, revealing that Ce has the second lowest formation energy in our comparison, indicating a good solubility. In addition, all attempts to find a general relation between a geometrical quantity with doping and the energy differences or the formation energy failed. However, for an idea of the incorporation of the dopants into the host HfO<sub>2</sub> crystal, the geometric neighborhood of the dopants is analyzed in the next section.

**3.5. Geometrical Incorporation of the Dopants.** To include chemical effects in the analysis, we have evaluated the dopant-to-oxygen bond geometry. The bonding environments

can be classified with polyhedra. Figure 1 shows the incorporation of silicon into the host crystal for (a) the  $t$ -phase bonding to the four neighboring oxygens and (b) the  $p-o$ -phase bonding to the six neighboring oxygens. In general, Figure 1 exemplifies the incorporation of all the dopants into the host HfO<sub>2</sub> crystal. To discriminate between oxygen neighbors with an active or inactive bond to the dopant and thus defining the coordination numbers  $n$ , we require the distance to be within the average bond length plus 50 pm. This criterion matches very closely the average bond length as defined by Baur<sup>54</sup> in 1974. Instead of using Baur's fractional, effective coordination, we use the integer coordination from counting.

For the different phases and dopants, Table 4 collects the coordination number  $n$  from the computed structures. For Ti, Sn, and Zr the bond configuration is 7-fold and similar to undoped Hf, except for the  $t$ -phase. Zr has the same coordination as Hf itself, confirming the chemical similarity. On the other hand, C, Si, Ge, Ti, and Sn are 4-fold coordinated in the  $t$ -phase. In particular, C, as the smallest dopant in this comparison, differs in the bonding coordination significantly. In the less symmetric  $m$ -,  $o$ -, and  $p-o$ -phases, C has only three bonds to oxygen, suggesting that C left the substitutional position of Hf. Other more energetically favorable incorporations like interstitial or oxygen substitution of C in the crystal are possible but were not investigated in this study. Ge has six bonds in the three least symmetric phases. Si, being smaller, cannot build six bonds in the  $m$ - and  $o$ -phases, but only in the  $p-o$ -phase. Since the six bonds in the  $p-o$ -phase are stronger than the five bonds in the  $m$ - and  $o$ -phases, silicon may favor the  $p-o$ -phase relative to the other phases, with the exception of the  $t$ -phase. It seems that the 6-fold coordination of silicon leads to the second strongest bond, followed by the 4-fold coordination. The special facilitation of the  $p-o$ -phase with silicon doping is a result of the adoption of the favorable 6-fold coordination in comparison to the adoption of the unfavorable 5-fold coordination in the competing  $m$ - and  $o$ -phases.

Along with the coordination number in Table 4, the distortion index  $d$  is given. The distortion index describes the root-mean-square deviation of the bond length from the average bond length. Therefore, the distortion index is a measure for the symmetry of the bond configuration.<sup>54</sup> Since smaller values indicate a more symmetric incorporation, Si, Ge, Ti, and Sn have an excellent fit in the  $t$ -phase of HfO<sub>2</sub>. Surprisingly, the incorporation of C in HfO<sub>2</sub> is very symmetric for all phases, indicated by the overall small distortion indices. Different from what one might expect, no general trend between the crystal radius, the coordination number, and the distortion index could be found. Nevertheless, correlation plots for 3.125 and 6.25 f.u.%

**Table 4. Calculated Bond Coordination  $n$  and the Distortion Index  $d$  for the Four-Valent Dopants D**

D	$r_c^a$ (pm)	$m$		$o$		$p-o$		$t$	
		$n$	$d$ (pm)	$n$	$d$ (pm)	$n$	$d$ (pm)	$n$	$d$ (pm)
C	29	3	0.008	3	0.007	3	0.008	4	0.014
Si	40	5	0.017	5	0.030	6	0.036	4	0.000
Ge	53	6	0.034	6	0.033	6	0.061	4	0.000
Ti	56	7	0.055	7	0.057	7	0.046	4	0.000
Sn	69	7	0.038	7	0.031	7	0.034	4	0.000
Hf	97	7	0.026	7	0.026	7	0.021	8	0.062
Zr	98	7	0.026	7	0.027	7	0.022	8	0.059
Ce	111	7	0.028	7	0.027	7	0.028	8	0.026

<sup>a</sup>The crystal radius  $r_c$  is for the coordination number  $n$  of the  $t$ -phase according to ref 52.

doping concentrations can be found in the Supporting Information in Figures S2 and S3.

#### 4. CONCLUSIONS

We have explored the effect of silicon doping and other four-valent dopants on the crystallographic phase formation, especially of the *p*-*o*-phase, in HfO<sub>2</sub> from first-principles. In a first step, we evaluated different DFT methods—LDA, PBE, and HSE06 XC functionals, all-electron and plane-wave—for silicon doping and found all methods to predict qualitatively a strong stabilization of the *t*-phase and a weaker stabilization of the *p*-*o*-phase, such that the *p*-*o*-phase is below the *t*-phase only in a concentration window around 3–5 f.u. All methods agree that in this concentration window the *m*-phase and the *o*-phase are still lower, revealing that Si doping alone is insufficient to explain the favoring of the ferroelectric *p*-*o*-phase for monocrystalline material. Further mechanisms for removing the *m*-phase and the *o*-phase from the ground state are required as discussed in previous work.<sup>4,13,21,50</sup> An analysis of several possible defect states revealed that mainly the Si<sub>Hf</sub> defect is introduced from doping in ALD processes. With analysis of the concentration dependence, nonlinear doping effects become visible, which require a more thorough analysis of the dopant–dopant interaction effects. To find possible systematic effects of HfO<sub>2</sub> doping, we calculated the effect of the four-valent dopants C, Ge, Ti, Sn, Ce, and Zr on the phase stability. Aside from Si, only Sn and Zr show a small stabilization effect of the *p*-*o*-phase. The effect on the *t*-phase is known<sup>11,12</sup> and was reproduced. The effects of doping on crystal volumes are on the order of 1%, but the related deformation energy turns out to be much smaller than the introduced formation energy, such that the main effect of doping is more of a chemical than geometrical nature. The significant stabilization of the *p*-*o*-phase with silicon turns out to be a very specific effect. As the promotion of the *t*-phase is related to the existence of a tetrahedral bonding configuration, which is especially strong, the promotion of the *p*-*o*-phase is related to the existence of an octahedral bonding configuration. For the other four-valent dopants, this bonding configuration does not exist, or it is in a very irregular shape, like in Ge. It is expected that the explanation of *p*-*o*-phase stabilization in HfO<sub>2</sub> with other dopants like Al, Y, La, and Gd has a different root cause.

On the basis of the calculations, Ce-doped HfO<sub>2</sub> is a promising candidate to favor ferroelectricity in HfO<sub>2</sub> and for use in applications such as ferroelectric memories (FeRAMs) or energy-related applications. The stabilization of the *p*-*o*-phase relative to the stabilization of the *t*-phase is good, promising a large window of concentration. On the basis of the small formation energy, the solubility in HfO<sub>2</sub> is good, and the volume increase with doping should lower the coercive field.

#### ■ ASSOCIATED CONTENT

##### ■ Supporting Information

The Supporting Information is available free of charge on the ACS Publications website at DOI: 10.1021/acsanm.7b00124.

Tabulated lattice constants and band gaps for the different DFT programs and methods for silicon doping; volume against Shannon radius for 3.125 f.u.% doping concentration; and different correlation for 6.25 and 3.125 f.u.% doping concentrations (PDF)

#### ■ AUTHOR INFORMATION

##### Corresponding Authors

\*E-mail: kuenneth@hm.edu.

\*E-mail: akersch@hm.edu.

##### ORCID

Christopher Künneth: 0000-0002-6958-4679

##### Notes

The authors declare no competing financial interest.

#### ■ ACKNOWLEDGMENTS

The authors thank U. Schröder, T. Schenk, and M. H. Park from NaMLab/SNU and U. Böttger, S. Starschich from RWTH Aachen for discussions. The German Research Foundation (Deutsche Forschungsgemeinschaft) is acknowledged for funding this research in the frame of the project “Inferox” (Project MI 1247/11-1). The authors gratefully acknowledge the Gauss Centre for Supercomputing e.V. ([www.gauss-centre.eu](http://www.gauss-centre.eu)) for funding this project by providing computing time on the GCS Supercomputer SuperMUC at Leibniz Supercomputing Center (LRZ, [www.lrz.de](http://www.lrz.de)).

#### ■ REFERENCES

- (1) Böske, T. S.; Müller, J.; Bräuhaus, D.; Schröder, U.; Böttger, U. Ferroelectricity in Hafnium Oxide Thin Films. *Appl. Phys. Lett.* **2011**, *99*, 10–13.
- (2) Sang, X.; Grimley, E. D.; Schenk, T.; Schroeder, U.; Lebeau, J. M. On the Structural Origins of Ferroelectricity in HfO<sub>2</sub> Thin Films. *Appl. Phys. Lett.* **2015**, *106*, 162905.
- (3) Müller, J.; Böske, T. S.; Schröder, U.; Mueller, S.; Bräuhaus, D.; Böttger, U.; Frey, L.; Mikolajick, T. Ferroelectricity in Simple Binary ZrO<sub>2</sub> and HfO<sub>2</sub>. *Nano Lett.* **2012**, *12*, 4318–4323.
- (4) Materlik, R.; Künneth, C.; Kersch, A. The Origin of Ferroelectricity in Hf<sub>1-x</sub>Zr<sub>x</sub>O<sub>2</sub>: A Computational Investigation and a Surface Energy Model. *J. Appl. Phys.* **2015**, *117*, 134109.
- (5) Mueller, W.; Aichmayr, G.; Bergner, W.; Erben, E.; Hecht, T.; Kapteyn, C.; Kersch, A.; Kudelka, S.; Lau, F.; Luetzen, J.; Orth, A.; Nuetzel, J.; Schloesser, T.; Scholz, A.; Schroeder, U.; Sieck, A.; Spitzer, A.; Strasser, M.; Wang, P.-f.; Wege, S.; Weis, R. Challenges for the DRAM Cell Scaling to 40nm. *IEEE Electron Devices Meet.* **2005**, 336–339.
- (6) Mikolajick, T.; Müller, S.; Schenk, T.; Yurchuk, E.; Slesazek, S.; Flachowsky, S.; Bentum, R. V.; Kolodinski, S.; Polakowski, P. Doped Hafnium Oxide - An Enabler for Ferroelectric Field Effect Transistors. *Adv. Sci. Technol.* **2014**, *95*, 136–145.
- (7) Richter, C.; Schenk, T.; Park, M. H.; Tschamtkte, F. A.; Grimley, E. D.; Lebeau, J. M.; Zhou, C.; Fancher, C. M.; Jones, J. L.; Mikolajick, T.; Schroeder, U. Si Doped Hafnium Oxide-A “Fragile” Ferroelectric System. *Adv. Electron. Mater.* **2017**, *3*, 1700131-1–1700131-12.
- (8) In Richter’s publication, the ALD cycle ratio is given instead of a dopant concentration since the relative incorporation of Hf and silicon is not known with a high accuracy. Here, we translate the cycle ratio into f.u.% assuming equal incorporation rate, achieving a better comparison of the computed results with experiments.
- (9) Xu, L.; Nishimura, T.; Shibayama, S.; Yajima, T.; Migita, S.; Toriumi, A. Kinetic Pathway of the Ferroelectric Phase Formation in Doped HfO<sub>2</sub> Films. *J. Appl. Phys.* **2017**, *122*, 124104.
- (10) Kim, K. D.; Park, M. H.; Kim, H. J.; Kim, Y. J.; Moon, T.; Lee, Y. H.; Hyun, S. D.; Gwon, T.; Hwang, C. S. Ferroelectricity in Undoped HfO<sub>2</sub> Thin Films Induced by Deposition Temperature Control During Atomic Layer Deposition. *J. Mater. Chem. C* **2016**, *4*, 6864–6872.
- (11) Lee, C.-K.; Cho, E.; Lee, H.-S.; Hwang, C. S.; Han, S. First-Principles Study on Doping and Phase Stability of HfO<sub>2</sub>. *Phys. Rev. B: Condens. Matter Mater. Phys.* **2008**, *78*, 012102.
- (12) Fischer, D.; Kersch, A. The Effect of Dopants on the Dielectric Constant of HfO<sub>2</sub> and ZrO<sub>2</sub> from First Principles. *Appl. Phys. Lett.* **2008**, *92*, 012908.

- (13) Künneht, C.; Materlik, R.; Kersch, A. Modeling Ferroelectric Film Properties and Size Effects from Tetragonal Interlayer in Hf<sub>1-x</sub>Zr<sub>x</sub>O<sub>2</sub> Grains. *J. Appl. Phys.* **2017**, *121*, 205304.
- (14) Materlik, R.; Künneht, C.; Mikolajick, T.; Kersch, A. The Impact of Charge Compensated and Uncompensated Strontium Defects on the Stabilization of the Ferroelectric Phase in HfO<sub>2</sub>. *Appl. Phys. Lett.* **2017**, *111*, 082902.
- (15) Batra, R.; Huan, T. D.; Rossetti, G. A.; Ramprasad, R. Dopants Promoting Ferroelectricity in Hafnia: Insights from a comprehensive Chemical Space Exploration. *Chem. Mater.* **2017**, *29*, 9102–9109.
- (16) Cao, W.; Randall, C. A. Grain Size and Domain Size Relations in Bulk Ceramic Ferroelectric Materials. *J. Phys. Chem. Solids* **1996**, *57*, 1499–1505.
- (17) Li, P.; Chen, I. W.; Penner Hahn, J. E. Effect of Dopants on Zirconia Stabilization - An X-Ray Absorption Study: III, Charge-Compensating Dopants. *J. Am. Ceram. Soc.* **1994**, *77*, 1289–1295.
- (18) Genenko, Y. A.; Hirsch, O.; Erhart, P. Surface Potential at a Ferroelectric Grain due to Asymmetric Screening of Depolarization Fields. *J. Appl. Phys.* **2014**, *115*, 104102.
- (19) Corrêa, S. A.; Brizzi, S.; Schmeisser, D. Spectroscopic Investigation of the Electronic Structure of Thin Atomic Layer Deposition HfO<sub>2</sub> Films. *J. Vac. Sci. Technol., A* **2016**, *34*, 01A117.
- (20) Reyes-Lillo, S. E.; Garrity, K. F.; Rabe, K. M. Antiferroelectricity in Thin-Film ZrO<sub>2</sub> from First Principles. *Phys. Rev. B: Condens. Matter Mater. Phys.* **2014**, *90*, 140103.
- (21) Batra, R.; Huan, T. D.; Jones, J. L.; Rossetti, G.; Ramprasad, R. Factors Favoring Ferroelectricity in Hafnia: A First-Principles Computational Study. *J. Phys. Chem. C* **2017**, *121*, 4139–4145.
- (22) Park, M. H.; Kim, H. J.; Kim, Y. J.; Moon, T.; Hwang, C. S. The Effects of Crystallographic Orientation and Strain of Thin Hf<sub>0.5</sub>Zr<sub>0.5</sub>O<sub>2</sub> Film on its Ferroelectricity. *Appl. Phys. Lett.* **2014**, *104*, 072901.
- (23) Katayama et al.<sup>55</sup> have prepared epitaxial Y-doped HfO<sub>2</sub> in the *p*-*o*-phase. However, a key to the achievement was the preparation of an ITO bixbyite interlayer.
- (24) Blum, V.; Gehrke, R.; Hanke, F.; Havu, P.; Havu, V.; Ren, X.; Reuter, K.; Scheffler, M. Ab Initio Molecular Simulations with Numeric Atom-Centered Orbitals. *Comput. Phys. Commun.* **2009**, *180*, 2175–2196.
- (25) Knuth, F.; Carbogno, C.; Atalla, V.; Blum, V.; Scheffler, M. All-Electron Formalism for Total Energy Strain Derivatives and Stress Tensor Components for Numeric Atom-Centered Orbitals. *Comput. Phys. Commun.* **2015**, *190*, 33–50.
- (26) Marek, A.; Blum, V.; Johanni, R.; Havu, V.; Lang, B.; Auckenthaler, T.; Heinecke, A.; Bungartz, H.-J.; Lederer, H. The ELPA Library: Scalable Parallel Eigenvalue Solutions for Electronic Structure Theory and Computational Science. *J. Phys.: Condens. Matter* **2014**, *26*, 213201.
- (27) Auckenthaler, T.; Blum, V.; Bungartz, H. J.; Huckle, T.; Johanni, R.; Krämer, L.; Lang, B.; Lederer, H.; Willems, P. R. Parallel Solution of Partial Symmetric Eigenvalue Problems from Electronic Structure Calculations. *Parallel Comput.* **2011**, *37*, 783–794.
- (28) Havu, V.; Blum, V.; Havu, P.; Scheffler, M. Efficient O(N) Integration for All-Electron Electronic Structure Calculation Using Numeric Basis Functions. *J. Comput. Phys.* **2009**, *228*, 8367–8379.
- (29) Torrent, M.; Jollet, F.; Bottin, F.; Zerah, G.; Gonze, X. Implementation of the Projector Augmented-Wave Method in the ABINIT Code: Application to the Study of Iron Under Pressure. *Comput. Mater. Sci.* **2008**, *42*, 337–351.
- (30) Gonze, X.; Jollet, F.; Abreu Araujo, F.; Adams, D.; Amadon, B.; Applencourt, T.; Audouze, C.; Beuken, J. M.; Bieder, J.; Bokhanchuk, A.; Bousquet, E.; Bruneval, F.; Caliste, D.; Côté, M.; Dahm, F.; Da Pieve, F.; Delaveau, M.; Di Gennaro, M.; Dorado, B.; Espejo, C.; Geneste, G.; Genovese, L.; Gerossier, A.; Giantomassi, M.; Gillet, Y.; Hamann, D. R.; He, L.; Jomard, G.; Laflamme Janssen, J.; Le Roux, S.; Levitt, A.; Lherbier, A.; Liu, F.; Lukačević, I.; Martin, A.; Martins, C.; Oliveira, M. J.; Poncé, S.; Pouillon, Y.; Rangel, T.; Rignanese, G. M.; Romero, A. H.; Rousseau, B.; Rubel, O.; Shukri, A. A.; Stankovski, M.; Torrent, M.; Van Setten, M. J.; Van Troeye, B.; Verstraete, M. J.; Waroquiers, D.; Wiktorski, J.; Xu, B.; Zhou, A.; Zwanziger, J. W. Recent Developments in the ABINIT Software Package. *Comput. Phys. Commun.* **2016**, *205*, 106–131.
- (31) Gonze, X.; Amadon, B.; Anglade, P. M.; Beuken, J. M.; Bottin, F.; Boulanger, P.; Bruneval, F.; Caliste, D.; Caracas, R.; Côté, M.; Deutsch, T.; Genovese, L.; Ghosez, P.; Giantomassi, M.; Goedecker, S.; Hamann, D. R.; Hermet, P.; Jollet, F.; Jomard, G.; Leroux, S.; Mancini, M.; Mazevet, S.; Oliveira, M. J.; Onida, G.; Pouillon, Y.; Rangel, T.; Rignanese, G. M.; Sangalli, D.; Shaltaf, R.; Torrent, M.; Verstraete, M. J.; Zerah, G.; Zwanziger, J. W. ABINIT: First-Principles Approach to Material and Nanosystem Properties. *Comput. Phys. Commun.* **2009**, *180*, 2582–2615.
- (32) Perdew, J. P.; Wang, Y. Accurate and Simple Analytic Representation of the Electron-Gas Correlation Energy. *Phys. Rev. B: Condens. Matter Mater. Phys.* **1992**, *45*, 13244–13249.
- (33) Perdew, J. P.; Burke, K.; Ernzerhof, M. Generalized Gradient Approximation Made Simple. *Phys. Rev. Lett.* **1996**, *77*, 3865–3868.
- (34) Heyd, J.; Scuseria, G. E.; Ernzerhof, M. Erratum: Hybrid Functionals Based on a Screened Coulomb Potential (Journal of Chemical Physics (2003) 118(8207)). *J. Chem. Phys.* **2006**, *124*, 219906.
- (35) Ren, X.; Rinke, P.; Blum, V.; Wieferink, J.; Tkatchenko, A.; Sanfilippo, A.; Reuter, K.; Scheffler, M. Resolution-of-Identity Approach to Hartree-Fock, Hybrid Density Functionals, RPA, MP2 and GW with Numeric Atom-Centered Orbital Basis Functions. *New J. Phys.* **2012**, *14*, 053020.
- (36) Perdew, J. P.; Zunger, A. Self-Interaction Correction to Density-Functional Approximations for Many-Electron Systems. *Phys. Rev. B: Condens. Matter Mater. Phys.* **1981**, *23*, 5048–5079.
- (37) Garrity, K. F.; Bennett, J. W.; Rabe, K. M.; Vanderbilt, D. Pseudopotentials for High-Throughput DFT Calculations. *Comput. Mater. Sci.* **2014**, *81*, 446–452.
- (38) Togo, A.; Tanaka, I. First Principles Phonon Calculations in Materials Science. *Scr. Mater.* **2015**, *108*, 1–5.
- (39) Freysoldt, C.; Grabowski, B.; Hickel, T.; Neugebauer, J.; Kresse, G.; Janotti, A.; Van De Walle, C. G. First-Principles Calculations for Point Defects in Solids. *Rev. Mod. Phys.* **2014**, *86*, 253–305.
- (40) Park, M. H.; Kim, H. J.; Kim, Y. J.; Jeon, W.; Moon, T.; Hwang, C. S. Ferroelectric Properties and Switching Endurance of Hf<sub>0.5</sub>Zr<sub>0.5</sub>O<sub>2</sub> Films on TiN Bottom and TiN or RuO<sub>2</sub> Top Electrodes. *Phys. Status Solidi RRL* **2014**, *8*, 532–535.
- (41) Pešić, M.; Fengler, F. P. G.; Larcher, L.; Padovani, A.; Schenk, T.; Grimley, E. D.; Sang, X.; LeBeau, J. M.; Slesazek, S.; Schroeder, U.; Mikolajick, T. Physical Mechanisms behind the Field-Cycling Behavior of HfO<sub>2</sub>-Based Ferroelectric Capacitors. *Adv. Funct. Mater.* **2016**, *26*, 4601–4612.
- (42) Stukowski, A. Visualization and Analysis of Atomistic Simulation Data with OVITO - the Open Visualization Tool. *Modell. Simul. Mater. Sci. Eng.* **2010**, *18*, 015012.
- (43) Zhao, L.; Nelson, M.; Aldridge, H.; Iamsari, T.; Fancher, C. M.; Forrester, J. S.; Nishida, T.; Moghaddam, S.; Jones, J. L. Crystal Structure of Si-Doped HfO<sub>2</sub>. *J. Appl. Phys.* **2014**, *115*, 034104.
- (44) Lowther, J. E.; Dewhurst, J. K.; Leger, J. M.; Haines, J. Relative Stability of ZrO<sub>2</sub> HfO<sub>2</sub> Structural Phases. *Phys. Rev. B: Condens. Matter Mater. Phys.* **1999**, *60*, 14485–14488.
- (45) Fadda, G.; Zanzotto, G.; Colombo, L. First-Principles Study of the Effect of Pressure on the Five Zirconia Polymorphs. I. Structural, Vibrational, and Thermoelastic Properties. *Phys. Rev. B: Condens. Matter Mater. Phys.* **2010**, *82*, 1–13.
- (46) Barabash, S. V.; Pramanik, D.; Zhai, Y.; Magyari-Kope, B.; Nishi, Y. Ferroelectric Switching Pathways and Energetics in (Hf<sub>1-x</sub>Zr<sub>x</sub>)O<sub>2</sub>. *ECS Trans.* **2017**, *75*, 107–121.
- (47) Arroyo-de Dompablo, M. E.; Morales-García, A.; Taravillo, M. DFT + U Calculations of Crystal Lattice, Electronic Structure, and Phase Stability Under Pressure of TiO<sub>2</sub> Polymorphs. *J. Chem. Phys.* **2011**, *135*, 054503.
- (48) Lomenzo, P. D.; Takmeel, Q.; Zhou, C.; Chung, C. C.; Moghaddam, S.; Jones, J. L.; Nishida, T. Mixed Al and Si Doping in

Ferroelectric HfO<sub>2</sub> Thin Films. *Appl. Phys. Lett.* **2015**, *107*, 242903-1–242903-6.

(49) Starschich, S.; Menzel, S.; Böttger, U. Evidence for Oxygen Vacancies Movement During Wake-Up in Ferroelectric Hafnium Oxide. *Appl. Phys. Lett.* **2016**, *108*, 032903.

(50) Batra, R.; Tran, H. D.; Ramprasad, R. Stabilization of Metastable Phases in Hafnia Owing to Surface Energy Effects. *Appl. Phys. Lett.* **2016**, *108*, 172902.

(51) Starschich, S.; Boettger, U. An Extensive Study of the Influence of Dopants on the Ferroelectric Properties of HfO<sub>2</sub>. *J. Mater. Chem. C* **2017**, *5*, 333–338.

(52) Shannon, R. D. Revised Effective Ionic Radii and Systematic Studies of Interatomic Distances in Halides and Chalcogenides. *Acta Crystallogr., Sect. A: Cryst. Phys., Diffraction, Theor. Gen. Crystallogr.* **1976**, *32*, 751–767.

(53) Clima, S.; Wouters, D. J.; Adelman, C.; Schenk, T.; Schroeder, U.; Jurczak, M.; Pourtois, G. Identification of the Ferroelectric Switching Process and Dopant-Dependent Switching Properties in Orthorhombic HfO<sub>2</sub>: A First Principles Insight. *Appl. Phys. Lett.* **2014**, *104*, 092906-0–092906-4.

(54) Baur, W. H. The Geometry of Polyhedral Distortions. Predictive Relationships for the Phosphate Group. *Acta Crystallogr., Sect. B: Struct. Crystallogr. Cryst. Chem.* **1974**, *30*, 1195–1215.

(55) Katayama, K.; Shimizu, T.; Sakata, O.; Shiraishi, T.; Nakamura, S.; Kiguchi, T.; Akama, A.; Konno, T. J.; Uchida, H.; Funakubo, H. Growth of (111)-Oriented Epi-taxial and Textured Ferroelectric Y-Doped HfO<sub>2</sub> Films for Downscaled Devices. *Appl. Phys. Lett.* **2016**, *109*, 112901.

# **Ferroelectric Phase Transitions in Nanoscale HfO<sub>2</sub> Films Enable Giant Pyroelectric Energy Conversion and Highly Efficient Supercapacitors**

Michael Hoffmann, Uwe Schroeder, Christopher Künneth, Alfred Kersch,  
Sergej Starschich, Ulrich Böttger, and Thomas Mikolajick  
Nano Energy, vol. 18, pp. 154–164, 2015.  
DOI: [10.1016/j.nanoen.2015.10.005](https://doi.org/10.1016/j.nanoen.2015.10.005)

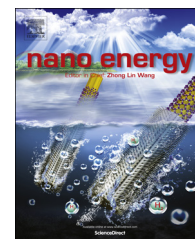
Reprinted (adapted) with permission from Elsevier Nano Energy. Copyright 2018 Elsevier.



Available online at [www.sciencedirect.com](http://www.sciencedirect.com)

ScienceDirect

journal homepage: [www.elsevier.com/locate/nanoenergy](http://www.elsevier.com/locate/nanoenergy)



RAPID COMMUNICATION

# Ferroelectric phase transitions in nanoscale HfO<sub>2</sub> films enable giant pyroelectric energy conversion and highly efficient supercapacitors



Michael Hoffmann<sup>a</sup>, Uwe Schroeder<sup>a,\*</sup>, Christopher Künneth<sup>b</sup>, Alfred Kersch<sup>b</sup>, Sergej Starschich<sup>c</sup>, Ulrich Böttger<sup>c</sup>, Thomas Mikolajick<sup>a,d</sup>

<sup>a</sup>NaMLab gGmbH, Noethnitzer Str. 64, D-01187 Dresden, Germany

<sup>b</sup>Munich University of Applied Sciences, Loth Str. 34, D-80335 Munich, Germany

<sup>c</sup>Institut für Werkstoffe der Elektrotechnik, RWTH Aachen University, Sommerfeldstr. 24, D-52074 Aachen, Germany

<sup>d</sup>Chair of Nanoelectronic Materials, TU Dresden, D-01062 Dresden, Germany

Received 16 July 2015; received in revised form 23 September 2015; accepted 8 October 2015

Available online 20 October 2015

## KEYWORDS

Pyroelectric;  
Ferroelectric;  
Hafnium oxide;  
Supercapacitor;  
Electrocaloric effect;  
Energy harvesting

## Abstract

Temperature- and field-induced phase transitions in ferroelectric nanoscale TiN/Si:HfO<sub>2</sub>/TiN capacitors with 3.8 to 5.6 mol% Si content are investigated for energy conversion and storage applications. Films with 5.6 mol% Si concentration exhibit an energy storage density of  $\sim 40$  J/cm<sup>3</sup> with a very high efficiency of  $\sim 80\%$  over a wide temperature range useful for supercapacitors. Furthermore, giant pyroelectric coefficients of up to  $-1300$   $\mu\text{C}/(\text{m}^2 \text{K})$  are observed due to temperature dependent ferroelectric to paraelectric phase transitions. The broad transition region is related to the grain size distribution and adjustable by the Si content. This strong pyroelectricity yields electrothermal coupling factors  $k^2$  of up to 0.591 which are more than one order of magnitude higher than the best values ever reported. This enables pyroelectric energy harvesting with the highest harvestable energy density ever reported of 20.27 J/cm<sup>3</sup> per Olsen cycle. Possible applications in infrared sensing are discussed. Inversely, through the electrocaloric effect an adiabatic temperature change of up to 9.5 K and the highest refrigerant capacity ever reported of 19.6 J/cm<sup>3</sup> per cycle is achievable. This might

\*Corresponding author.

E-mail addresses: [michael.hoffmann@namlab.com](mailto:michael.hoffmann@namlab.com) (M. Hoffmann), [uwe.schroeder@namlab.com](mailto:uwe.schroeder@namlab.com) (U. Schroeder), [kueneth@hm.edu](mailto:kueneth@hm.edu) (C. Künneth), [akersch@hm.edu](mailto:akersch@hm.edu) (A. Kersch), [starschich@iwe.rwth-aachen.de](mailto:starschich@iwe.rwth-aachen.de) (S. Starschich), [boettger@iwe.rwth-aachen.de](mailto:boettger@iwe.rwth-aachen.de) (U. Böttger), [thomas.mikolajick@namlab.com](mailto:thomas.mikolajick@namlab.com) (T. Mikolajick).

<http://dx.doi.org/10.1016/j.nanoen.2015.10.005>

2211-2855/© 2015 Elsevier Ltd. All rights reserved.



enable energy efficient on-chip electrocaloric cooling devices. Additionally, low cost fabrication of these films is feasible by existing semiconductor process technology.

© 2015 Elsevier Ltd. All rights reserved.

## Introduction

The ever increasing energy consumption and accompanying rise of greenhouse gases poses a serious challenge for the search of new material systems for efficient energy conversion and storage. Nanostructured materials can exhibit vastly enhanced properties for these applications compared to their bulk counterparts. Especially, thin film pyroelectrics can be used for efficient conversion of thermal into electrical energy and vice versa [1]. These materials with a temperature dependent spontaneous polarization  $P_S$  can already be found in widespread applications particularly in infrared sensing [2,3]. However, a lot of recent research focuses on pyroelectric energy harvesting (PEH) [4] and the inverse effect of electrocaloric cooling [5,6]. Both phenomena are closely related and have already been studied for half a century [4,7]. While PEH is a promising method to convert the abundance of low-grade waste heat into electric energy [8], the electrocaloric effect (ECE) might be used in solid state cooling devices with high energy efficiency [9].

Achievable figures of merit (FOMs) for both applications as well as infrared sensing strongly depend on the intrinsic properties of the applied pyroelectric materials [2,4,5,10]. Especially ferroelectrics were shown to exhibit very strong pyroelectricity [2] near phase transitions to paraelectric [11,12] or antiferroelectric (AFE) phases [13]. Many of the materials investigated so far were bulk crystals or ceramics based on classical perovskite ferroelectrics [11,14–17]. Thin films were shown to exhibit remarkable properties as seen in the giant ECE for example in lead zirconate titanate (PZT) [7] and Pb<sub>0.8</sub>Ba<sub>0.2</sub>ZrO<sub>3</sub> [12] or PEH using poly(vinylidene fluoride-trifluoroethylene) (P(VDF-TrFE)) [18]. This is mainly owed to the higher breakdown field strength compared to ceramics or bulk crystals [7]. AFE materials were also shown to have very favorable properties for electrostatic energy storage in supercapacitor applications [19,20]. Unfortunately, many of these complex thin films either contain lead which is toxic or deteriorate already at fairly low temperatures like polymers. Additionally, incompatibility with standard semiconductor process technology makes on-chip fabrication very complicated and therefore expensive.

Recently, ferroelectricity was first shown to occur in doped HfO<sub>2</sub> [21,22] and Hf<sub>x</sub>Zr<sub>1-x</sub>O<sub>2</sub> [23] thin films. While the ferroelectric phase has been identified as the non-centrosymmetric orthorhombic Pca2<sub>1</sub> phase [24], observed electric field-induced ferroelectric behavior seems to originate from the tetragonal P4<sub>2</sub>/nmc phase through a transition to the aforementioned Pca2<sub>1</sub> phase [25]. These lead-free simple binary oxide films are temperature stable [26], highly compatible with silicon technology [27] and can be deposited on 3D nanostructures using atomic layer deposition (ALD) [28]. So far, most research on these material

systems was focused on ferroelectric (FE) capacitors [29] and field-effect transistors [27,30] for non-volatile memories and low power computing applications. Beyond that, first studies showed the great potential of Hf<sub>x</sub>Zr<sub>1-x</sub>O<sub>2</sub> films exhibiting field-induced ferroelectricity for energy storage supercapacitors [31] and electrocaloric cooling as well as PEH [32]. However, an in depth study of pyroelectricity and energy storage in doped HfO<sub>2</sub> is still missing. Therefore, in this work we investigate the pyroelectric properties of Si:HfO<sub>2</sub> thin films and assess their applicability for infrared detectors, PEH, electrocaloric cooling devices and electrostatic supercapacitors.

## Material and methods

Si:HfO<sub>2</sub> films with a physical thickness of 9 nm were deposited by a metal organic ALD process based on Tetrakis(ethylmethylamino)-hafnium (TEMAHf), Tetrakis-dimethylamino-silane (4DMAS) precursors and ozone. The Si content was defined by varying the cycle ratio of the precursors and monitored by secondary ion mass spectrometry and elastic recoil detection analysis on samples without thermal treatment. TiN bottom and top electrodes were deposited by a pulsed CVD process based on TiCl<sub>4</sub> and NH<sub>3</sub>. Crystallization of the Si:HfO<sub>2</sub> thin films (3.8 to 5.6 mol% Si) was induced by a 1000 °C/20 s anneal in nitrogen after TiN top electrode deposition. While all electrical measurements were performed on metal-insulator-metal (MIM) capacitors with an electrode area of 31,000 μm<sup>2</sup>, blanket wafers were used for physical characterization. To investigate the influence of the sample temperature with respect to polarization changes the samples were heated and cooled in a range between 80 K and 480 K. The polarization versus electric field dependencies were derived from integrating the displacement current for an applied triangular AC voltage signal using a virtual ground amplifier (AixACCT TF Analyzer 2000) at a frequency of 1 kHz. Capacitance-voltage measurements were carried out on a HP 4284 A Precision LCR Meter for extraction of the permittivity and loss factors of the films using frequencies from 20 Hz to 10 kHz and a small-signal amplitude of 50 mV. Pyroelectric currents were measured with a Keithley 6430 Sub-Femtoamp Remote Source-Meter at 0 V while increasing the sample temperature. Scanning electron microscopy (SEM) images were acquired on a Zeiss LEO 1560 microscope with an acceleration voltage of 0.8 kV. X-ray reflectivity (XRR) measurements were carried out on a Bruker D8 Discover (Cu-Kα radiation, λ=0.154 nm) to determine the thickness of the samples.

## Theory

The following experimental results reported in this article give cause for a theoretical investigation. Especially the represented well known behavior of ferroelectrics to change

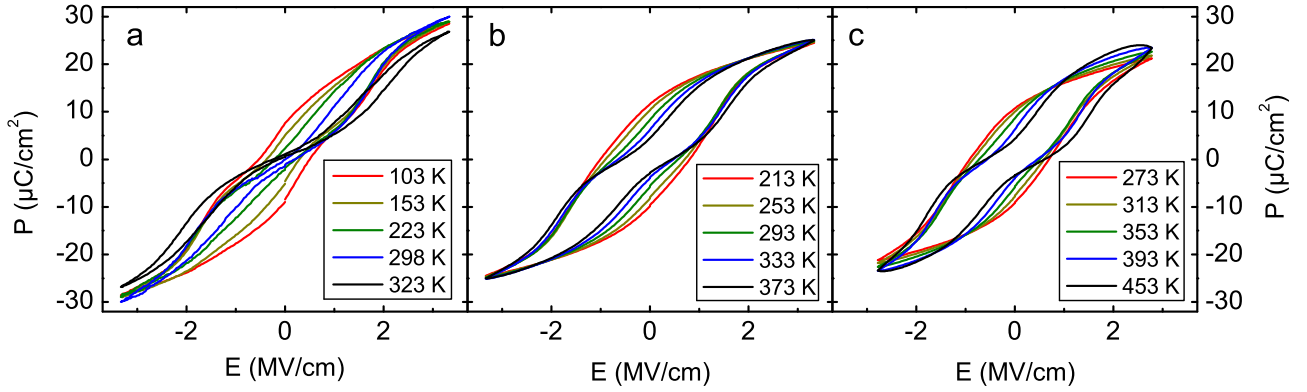


**Figure 1** Temperature dependent polarization hysteresis measurements for MIM capacitor with a 9 nm Si:HfO<sub>2</sub> layer containing (a) 5.6 mol%, (b) 4.3 mol% and (c) 3.8 mol% of Si.

their structural phase by an electric field and temperature [7] should be further investigated and compared to the recent theoretical description. In addition, the effect of phase transitions on the pyroelectric properties should be discussed. Grindlay [33] describes the proper pyroelectric coefficient  $\Pi$  as a temperature  $T$  induced change of the electric displacement field  $D = \epsilon_0 E + P$  under the conditions of constant electric field  $E$  and stress  $\sigma$ , which yields in our case

$$\Pi = \left( \frac{\partial D}{\partial T} \right)_{E, \sigma} = \left( \frac{\partial P}{\partial T} \right)_{\sigma} + \left( \frac{\partial P}{\partial \sigma} \right)_{T} \left( \frac{\partial \sigma}{\partial T} \right)_{\sigma} = \Pi_1 + \Pi_2, \quad (1)$$

where  $P$  is the electrical polarization of the ferroelectric material and  $\epsilon_0$  the vacuum permittivity.  $\Pi_1$  and  $\Pi_2$  are distinguishable quanta of the proper pyroelectric effect, whereby  $\Pi_1$  refers to a clamped and  $\Pi_2$  to an unclamped sample, respectively [3,34].

To estimate  $\Pi$  we use the linear thermal coefficient of monoclinic ZrO<sub>2</sub> ( $1.3 \cdot 10^{-5} \text{ K}^{-1}$  [35]) which is chemically very similar to HfO<sub>2</sub>. We have calculated the relaxed atom positions and Born effective charges from first principles, using the thermal expansion for the displacements, and obtained  $\Pi \sim 23 \mu\text{C}/(\text{m}^2 \text{ K})$ , which is rather small compared to our experimental results (see Section 4.2). Therefore, the giant pyroelectricity we observed cannot only originate from the proper pyroelectric behavior but rather from a phase transition, which is consistent with the literature for other materials near the Curie temperature [7,12,13]. If the change of dielectric displacement is caused by a phase transition, we obtain a morphotropic contribution  $\Pi_M$  related to the change of concentration  $c_f(T)$  of the ferroelectric phase depending on  $T$ . This gives cause to extend Eq. (1) resulting in a giant pyroelectric coefficient as

$$\Pi_G = \left( \frac{\partial}{\partial T} [c_f D] \right)_{E=0, \sigma} = (\Pi_1 + \Pi_2) c_f + \frac{\partial c_f}{\partial T} P = \Pi c_f + \Pi_M. \quad (2)$$

$c_f$  is 1 if the sample exhibits only ferroelectric behavior and 0 for completely paraelectric behavior ( $0 < c_f < 1$ ). For polycrystalline ferroelectric materials like Si:HfO<sub>2</sub> thin films investigated here, phase transitions do not always result in a macroscopic change of  $P$ , since a poling procedure might be necessary [36]. Considering an unpoled sample with randomly oriented grains, polarization of individual domains might compensate each other, leading to small  $\Pi_G$ .

Transitions of a poled ferroelectric to another crystallographic phase on the other hand can result in a very high  $\Pi_G$ , because of the much greater change of  $P$  with  $T$ . This has to be considered when comparing  $\Pi_G$  determined by different measurement methods, for example with and without an applied electric field. Additionally,  $\Pi_G$  can depend strongly on the grain size distribution in such films due to different phase transition temperatures for different grain sizes, where smaller grains have a lower Curie temperature [37,38]. Different grain size distributions can therefore result in a broadened phase transition over a wider temperature range [39].

## Results and discussion

### Phase transitions and energy storage

Figure 1 shows the temperature dependent hysteresis loops measured on Si:HfO<sub>2</sub> MIM capacitors with different Si content. For higher doping concentrations, a lower temperature is necessary to observe a change from a pure FE to a field-induced FE behavior as can be seen from the distinct pinched hysteresis loops at higher temperatures for all concentrations. This strong change of the hysteresis shape with temperature promises large capabilities of the material for pyroelectric energy harvesting as well as electrocaloric applications. The corresponding phase transitions of the samples with 3.8 and 4.3 mol% Si content have already been investigated by grazing-incidence X-ray diffraction (GIXRD) in Ref. [40]. These measurements revealed a more orthorhombic GIXRD pattern for 3.8 mol% Si and a more tetragonal one for 4.3 mol% Si at room temperature. Additional temperature dependent GIXRD patterns on the 3.8 mol% Si sample showed the same trend of a higher tetragonal phase fraction at higher temperatures [40]. For this sample, which is shown in Figure 1(c), a significant leakage current increase at a temperature of 453 K can be seen from the convex curvature of the hysteresis at high positive fields around 2 MV/cm which limits the operation voltage range for PEH and electrocaloric cooling cycles at elevated temperatures. The highest Si concentration of 5.6 mol% in Figure 1(a) exhibits the strongest constriction of the hysteresis loop at room temperature as well as the highest saturation polarization for the investigated

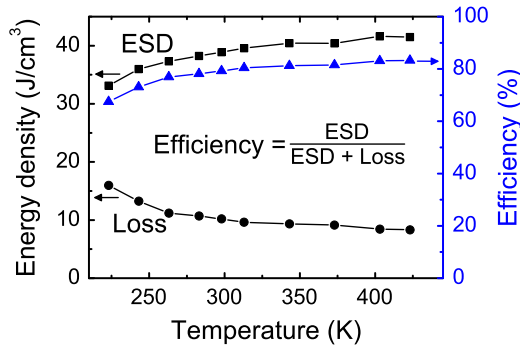


**Figure 2** Temperature dependent energy storage density (ESD) and loss of 5.6 mol% Si:HfO<sub>2</sub> thin films showing field-induced ferroelectricity for electrostatic supercapacitors.

temperature range. These characteristics are very favorable for energy storage applications like electrostatic supercapacitors [31].

An important figure of merit for this electrostatic storage is the energy storage density (ESD), which is given by the area bounded by the upper loop of the hysteresis curve and a horizontal line corresponding to the maximum polarization from zero to the highest positive applied field [31]. The efficiency describes how much of the stored energy is lost to heat during cycling of the hysteresis loop. This loss is equivalent to the area inside the  $P$ - $E$  loop for either positive or negative fields. Figure 2 shows the calculated ESD, loss and efficiency values of the 5.6 mol% Si sample as a function of temperature. For temperatures above 300 K both ESD and efficiency are rather stable and even increase for higher temperatures. Compared to the already very good properties of Hf<sub>0.3</sub>Zr<sub>0.7</sub>O<sub>2</sub> capacitors showing field-induced ferroelectricity reported in [31], our thin films exhibit about 30% higher ESD as well as 30% better efficiency at comparable electric fields over the same temperature range. Simultaneously, Si:HfO<sub>2</sub> possesses all the advantages of Hf<sub>x</sub>Zr<sub>1-x</sub>O<sub>2</sub>, like non-toxicity, high breakdown field strength and good 3D-integrability. By creating a dense array of deep trench capacitors within a Si substrate or stacked capacitors with a high aspect ratio above the transistor level, it should be possible to increase the ESD per projected area by more than one order of magnitude [28,41]. Additionally, easy integration into already existing semiconductor manufacturing processes enables a cost effective way to produce capacitors with very high ESD directly on a Si chip [32]. Other potential material systems for supercapacitors like Pb<sub>0.92</sub>La<sub>0.08</sub>Zr<sub>0.95</sub>Ti<sub>0.05</sub>O<sub>3</sub> (PLZT) [19] and P(VDF-TrFE) [20] on the other hand do not share these benefits and have much lower efficiency and ESD, respectively. While PLZT has a reported ESD as high as 53 J/cm<sup>3</sup> at room temperature this value drops to 37 J/cm<sup>3</sup> at 150 °C [19]. The efficiency is not calculated in ref. 19, however it is apparent from the hysteresis curves that it is much lower than 80%. P(VDF-TrFE) on the other hand shows good efficiency in the range of 70%, whereas the ESD is only about 14 J/cm<sup>3</sup> [20]. The large ESD of ~40 J/cm<sup>3</sup> as well as very high efficiency of ~80% and temperature stability of Si:HfO<sub>2</sub> makes it a very attractive alternative to these perovskite and polymer based materials for supercapacitors.

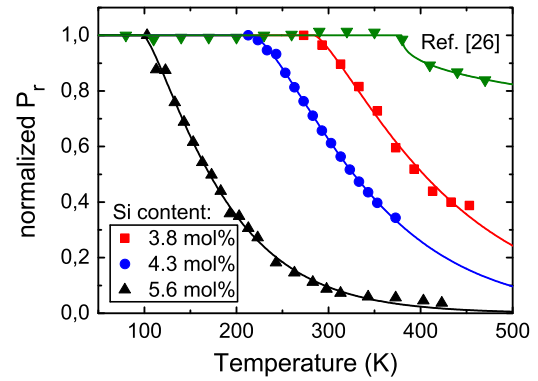


**Figure 3** Normalized remanent polarization  $P_r(T)$  values as a function of sample temperature for MIM capacitors with a 9 nm Si:HfO<sub>2</sub> layer having a Si content of ~3.4 to 5.6 mol%.

### Pyroelectric properties

Remanent polarization values  $P_r$  were extracted from the dynamic hysteresis measurements in Figure 1 at zero external field and are summarized in Figure 3 as a function of temperature. The lines in Figure 3 show incomplete gamma functions which were fitted to the measured data points. A good agreement ( $\chi^2 < 0.006$ ) was achieved for all fitted curves. One reference for even lower Si content [26] was added to display the wide phase transformation range. Remanent polarization values were normalized for easier comparison with the referenced lower Si concentration sample [26]. A clear transition from a pure FE behavior at liquid nitrogen temperature via a field-induced FE behavior to a paraelectric behavior with increasing temperature is visible for higher Si concentrations from Figure 3. For the lowest Si content the polarization is very stable over a wide temperature range up to 380 K. For the highest content of 5.6 mol% on the other hand the layer just reaches a maximum FE polarization at around 80 K. It seems possible to tune the phase transition temperature over this wide temperature range by carefully adjusting the Si concentration in the HfO<sub>2</sub> films which has already been proposed [40]. Here, we show that it is in fact possible to shift the phase transition temperature by more than 200 K through a change of the Si content.

The incomplete gamma function  $\gamma(s, R) = \frac{1}{\Gamma(s)} \cdot \int_0^R e^{-t} t^{s-1} dt$  was fitted to the raw data in Figure 3, where  $s$  is the shape parameter,  $R$  is the grain radius and  $\Gamma(s)$  is the gamma function. This was motivated by a grain size distribution analysis from SEM measurements after top electrode removal, which is shown in Figure 4 for a 5.6 mol% Si sample. It was found that the probability density function  $f(R)$  of the grain radii fits well to a Poisson distribution, whereby its cumulative density function is the incomplete gamma function. As already mentioned in the Section 3, such a grain size distribution could be the explanation for a broadened phase transition region, because of the grain size dependence of the Curie temperature  $T_c$  [37]. The smallest grains undergo this transition at lower temperature and since the change of  $P_r$  with higher  $T$  gets smaller, the contribution of the larger grains to  $P_r$  has to be smaller overall. This also corresponds to a reduction of the pyrocoefficient  $\Pi_G$  with increasing temperature.

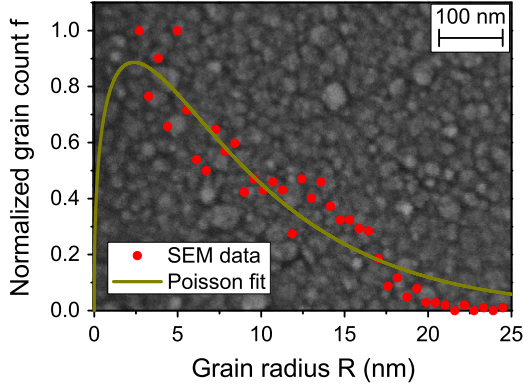


**Figure 4** Frequency distribution of grain radii (red dots) extracted from SEM measurement (background). The Poisson fit of the data  $f(R)$  (yellow line) possesses the shape parameter  $s=1.377 \pm 0.234$  for the corresponding incomplete gamma function.

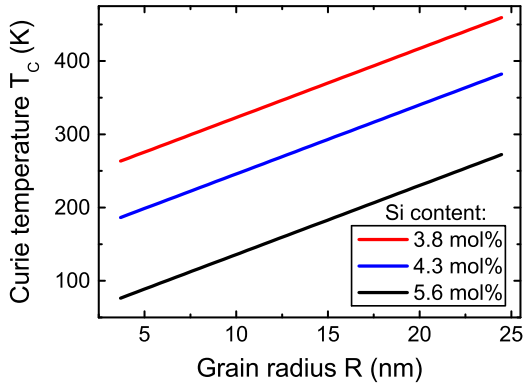


**Figure 5** Grain size dependent Curie temperature for Si:HfO<sub>2</sub> thin films with different Si concentrations under the assumption of the grain size distribution in Figure 4.

We now assume that the spread of the phase transition over temperature in Figure 3 originates from the distribution of grain radii [37,39]. We can then calculate the grain size dependent Curie temperature  $T_C$  by transforming the distribution of Curie temperatures  $\Pi_G(T)$  with the distribution of grain radii  $f(R)$  by

$$dR = \frac{\Pi_G(T)}{f(R)} \cdot dT_C. \quad (3)$$

The result is depicted in Figure 5 and shows that the Curie temperature increases linearly for small grain radii up to 25 nm, whereby the radii are independent of the Si concentration. However, we cannot completely rule out possible effects of the Si doping on the unit cell volume and grain size distribution within the statistical uncertainties of our analysis, where  $s$  was  $1.373 \pm 0.333$ ,  $1.652 \pm 0.114$  and  $1.408 \pm 0.141$  for 3.8, 4.3 and 5.6 mol% Si:HfO<sub>2</sub> samples, respectively (see Figure 3). The trend of increasing  $T_C$  with grain size is in accordance with results published for BaTiO<sub>3</sub> by Glinchuk and Bykov [37].

For the Si concentrations ranging from 3.8 to 5.6 mol%, that showed a clear phase transition within the measured temperature range, the according pyroelectric coefficients

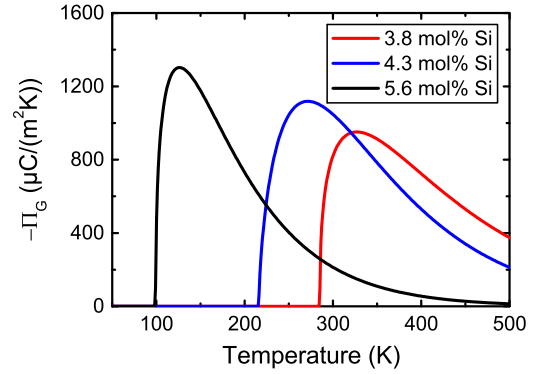


**Figure 6** Pyroelectric coefficients as a function of sample temperature as calculated from  $P_r$  values in Figure 3 for MIM capacitors with a 9 nm Si:HfO<sub>2</sub> layer having a Si content of 3.8 to 5.6 mol%.

$\Pi_G$  were derived from Eq. (2) with the values from Figure 3 and are depicted in Figure 6. Since an incomplete gamma function was fitted in Figure 3, the derivative with respect to  $T$  again yields a Poisson distribution. Very high maximum pyroelectric coefficients of  $-950$ ,  $-1100$  and  $-1300 \mu\text{C}/(\text{m}^2 \text{K})$  can be extracted for 3.8, 4.3 and 5.6 mol% of Si, respectively. In accordance with Figure 3, the temperature at which maximum  $\Pi_G$  occurs depends strongly on the Si concentration and is lower for higher mol% of Si. These maximum values are considerably high [4,6] and stem mostly from the orthorhombic to tetragonal phase transition ( $\Pi_G \approx \Pi_M$ ) rather than from the primary and secondary pyroelectric coefficients  $\Pi_1$  and  $\Pi_2$  [3], which coincides with our rather small estimate of  $23 \mu\text{C}/(\text{m}^2 \text{K})$  from section 3 and from Figure 3 where the slope of the curves for temperatures below the smallest phase transition temperatures is almost zero. For this reason, the normalized  $P_r(T)$  is the same as  $c_f(T)$  in our case and the maximum value of  $\Pi_G$  is only determined by the maximum of  $P_r$ , as can be seen in Eq. (2).

To further elucidate the magnitude of the phase transition contribution to  $\Pi_G$ , pyroelectric current measurements were carried out for 5.6 mol% Si:HfO<sub>2</sub> without an applied electric field. The sample was first cooled down to 173 K and then heated up again to 333 K in two steps. For a temperature change from 173 to 273 K and consecutively from 273 to 333 K, respective absolute values for the pyroelectric coefficients of 32 and 52  $\mu\text{C}/(\text{m}^2 \text{K})$  can be extracted by integration of the pyroelectric currents shown in Figure 7. Since the sample showed only a field-induced ferroelectric hysteresis (i. e. more tetragonal for  $E=0$ ) at room temperature and was getting more orthorhombic during cool-down, but was not poled in this FE state, the measured  $\Pi_G$  during heating is rather small. This might be due to a compensation of the polarization of randomly oriented domains without poling [36]. This strong influence of the poling procedure becomes especially apparent when comparing the rather small values from Figure 7 to the pyroelectric coefficients in Figure 6 between 173 to 333 K, since the absolute coefficients from Figure 6 are in a range between 150 and 1000  $\mu\text{C}/(\text{m}^2 \text{K})$ . The small but non-zero  $\Pi_G$  values obtained from pyroelectric currents in Figure 7 might be explained by only partial residual poling of the layer from the initial hysteresis measurements at room

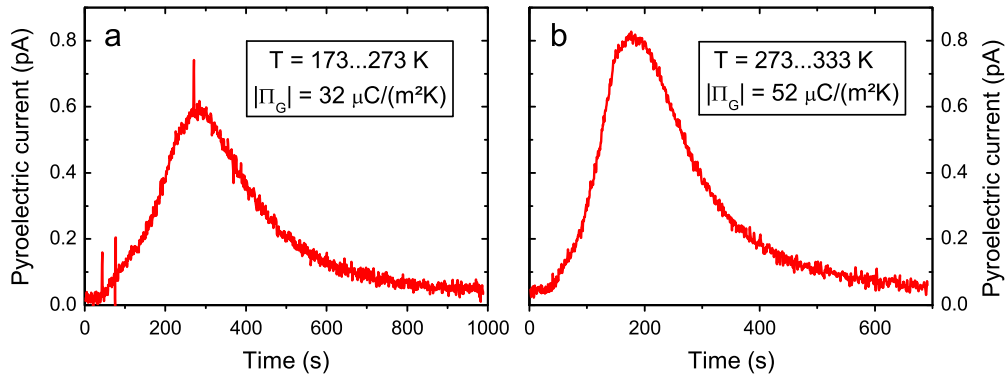


**Figure 7** Pyroelectric coefficients extracted through integration of the current resulting from a temperature change without applied electric field in Si:HfO<sub>2</sub> with 5.6 mol% Si.

**Table 1** Comparison of pyroelectric figures of merit for various materials.

Material	$\Pi_G$ [ $\mu\text{C}/(\text{m}^2 \text{K})$ ]	$T$ [K]	$\epsilon_r$	$F_V$ [ $\text{V m}^2/\text{J}$ ]	$F_I$ [ $10^{-10} \text{ m/V}$ ]	$F_D$ [ $10^{-5} \text{ m}^{3/2} \text{ J}^{-1/2}$ ]	$k^2$	Ref.
3.8 mol% Si:HfO <sub>2</sub>	−950 <sup>a</sup>	325	24	−	−	−	0.522	This work
4.3 mol% Si:HfO <sub>2</sub>	−1100 <sup>a</sup>	273	26	−	−	−	0.591	This work
5.6 mol% Si:HfO <sub>2</sub>	−1300 <sup>a</sup>	125	34	−	−	−	0.504	This work
Hf <sub>0.2</sub> Zr <sub>0.8</sub> O <sub>2</sub>	−52	300	38	0.06	0.20	0.7	0.001	[32]
PZT	−380	300	290	0.06	1.50	5.8	0.007	[10]
PVDF	−25	300	9	0.14	0.11	0.7	0.001	[10]
TGS	−280	300	38	0.36	1.21	6.6	0.030	[10]
PMN-0.25PT	−1790	300	2100	0.04	7.16	−	0.021	[4]

<sup>a</sup>Calculated from polarization hysteresis measurements.

temperature. This indicates that a poling procedure might be necessary to use these films in highly sensitive pyroelectric detectors. However, in contrast to Hf<sub>x</sub>Zr<sub>1−x</sub>O<sub>2</sub> films [32], no constant applied field is mandatory to observe pyroelectricity in Si:HfO<sub>2</sub>. This enables feasible infrared detection with these new pyroelectric materials for the first time, because leakage currents would superimpose the small pyroelectric currents in Hf<sub>x</sub>Zr<sub>1−x</sub>O<sub>2</sub> when a constant field is applied.

### Pyroelectric energy harvesting and infrared detection

Several FOMs for pyroelectric devices like infrared detectors and PEH have been established over the years [2,4,10,18], most of which can be calculated from basic material properties like the pyroelectric coefficient  $\Pi_G$ , the volume specific heat  $C_E$ , the dielectric permittivity  $\epsilon$  and the maximum working temperature  $T_{hot}$ . Commonly used FOMs for infrared sensing include the voltage responsivity  $F_V = \frac{\Pi_G}{(C_E \epsilon)}$ , the current responsivity  $F_I = \frac{\Pi_G}{C_E}$  and the signal-to-noise FOM  $F_D = \frac{\Pi_G}{(C_E \sqrt{\epsilon_0 \epsilon_r \tan \delta})}$ . Here,  $\Pi_G$  from Figure 7 has to be used, since highly hysteretic phase transitions as seen

in the  $P$ - $E$  curves in Figure 1 are not suitable to build infrared sensors. For PEH on the other hand, the high values for  $\Pi_G$  shown in Figure 6 are applicable, since electric field-cycling of the films is necessary in this case. For such PEH applications, the electrothermal coupling factor  $k^2 = \frac{\Pi_G^2 T_{hot}}{(C_E \epsilon)}$  is of importance. Table 1 shows the calculated values for the different Si:HfO<sub>2</sub> samples investigated here in comparison to other pyroelectric materials reported in literature. Relative permittivity values  $\epsilon_r$  and loss factors  $\tan \delta$  were extracted from temperature and frequency dependent capacitance-voltage measurements. For all samples a  $\tan \delta \approx 0.025$  was observed over a wide temperature range and even far below 100 Hz, which is the operating regime for many pyroelectric devices. The permittivity increased with increasing temperature and Si concentration, which is in accordance with reports on the electrical characteristics of 3.8 mol% Si:HfO<sub>2</sub> [43].  $C_E$  values were taken from Ref. [44] and are 2.69, 2.44 and 1.39 MJ/(m<sup>3</sup> K) for 325, 273 and 125 K, respectively. Additionally, for the 5.6 mol% sample the FOMs were calculated with the pyro-coefficient from Figure 7(b) at 300 K to compare them fairly with other materials for infrared detection.

The very high pyroelectric coefficients of the Si:HfO<sub>2</sub> films from hysteresis measurements are unique for lead-

**Table 2** Comparison of achievable harvestable energy densities for different pyroelectric materials.

Material	$N_D$ [J cm <sup>-3</sup> ]	Thickness	$\Delta E$ [MV/cm]	$\Delta T_{HL}$ [K]	Method	Ref.
5.6 mol% Si:HfO <sub>2</sub>	20.27 <sup>a</sup>	9 nm	3.33	320 <sup>a</sup>	indirect	This work
	7.52			125		
4.3 mol% Si:HfO <sub>2</sub>	5.74 <sup>a</sup>	9 nm	1.89	160 <sup>a</sup>	indirect	This work
	3.61			80		
3.8 mol% Si:HfO <sub>2</sub>	3.26	9 nm	0.89	160	indirect	This work
Hf <sub>0.2</sub> Zr <sub>0.8</sub> O <sub>2</sub>	11.55	9.2 nm	3.26	150	indirect	[32]
P(VDF-TrFE)	0.52	50 $\mu$ m	0.30	85	direct	[18]
YbFO	7.57	60 nm	4.00	285	indirect	[46]

<sup>a</sup>Calculated for the whole temperature range, with  $T_L$  below room temperature.

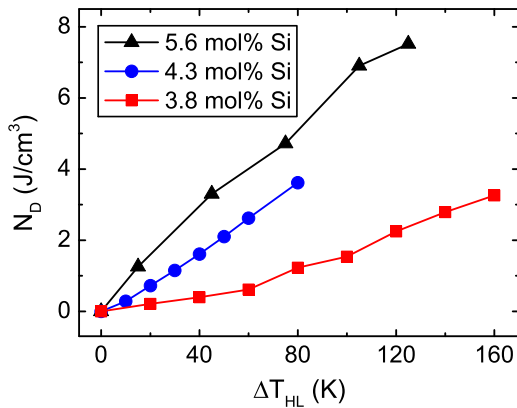


**Figure 8** Harvestable energy density per Olsen cycle  $N_D$  as a function of  $\Delta T_{HL}$  with  $T_L=298$  K for different Si concentrations with different applied fields (see Table 2).

free, non-perovskite materials with a relatively low permittivity. This leads to exceptionally good  $k^2$  values compared to other material systems. It should be noted, that the similar Hf<sub>0.2</sub>Zr<sub>0.8</sub>O<sub>2</sub> films reported in [32] showed practically no pyroelectricity without an applied field, making them undesirable for pyroelectric sensor applications in the investigated temperature range. Additionally, they calculated  $F_V$  and  $F_I$  values with  $\Pi_G$  from  $P$ - $E$  measurements, which is not reasonable for infrared sensor applications. Therefore, these values were not included in Table 1. Our Si:HfO<sub>2</sub> films on the other hand show for the first time pyroelectricity in HfO<sub>2</sub> without an applied electric field only from a change in temperature.

$F_V$  is comparable to the values reported PZT [10] and single crystals of 0.75Pb(Mg<sub>1/3</sub>Nb<sub>2/3</sub>)O-0.25PbTiO<sub>3</sub> (PMN-0.25PT) [4]. While  $F_I$  is lower than most materials in Table 1 it is almost twice as high compared to PVDF [10]. Additionally, the signal-to-noise FOM  $F_D$  is also comparable to PVDF [10]. The electrothermal coupling factors  $k^2$  for Si:HfO<sub>2</sub> calculated here are more than one order of magnitude higher compared to the best values reported so far and even two and a half orders of magnitude higher than for example PVDF and many other materials [4,10]. These characteristics show, that Si:HfO<sub>2</sub> can in principle be applied in infrared detectors. Especially, an integration into arrays on a chip for

thermal imaging with high resolution might be interesting, since the Si:HfO<sub>2</sub> films are predestined for deposition and patterning on a semiconductor substrate.

The application of PEH on the other hand seems ideally suited for this material system. For PEH using the Olsen cycle (which is a modified Ericsson heat engine cycle [15]), the pyroelectric film between two electrodes is subjected alternately to a cold and a hot source at temperatures  $T_L$  and  $T_H$ , respectively, while applying either a low or a high electric field [18]. The first step in the Olsen cycle corresponds to isothermal increase of the electric field from  $E_1$  to  $E_2$  at  $T_L$ . Subsequently, the material is heated to  $T_H$  in an isoelectric process. This is followed by a reduction of  $E_2$  back to  $E_1$  at  $T_H$  and finally the cycle is closed by reducing the temperature to  $T_L$  again at constant field  $E_1$  [45]. It was shown that these types of Olsen cycles can be 100 times more efficient compared to other harvesting cycles [15]. The harvestable energy density per Olsen cycle  $N_D$  for a given temperature change  $\Delta T_{HL}=T_H - T_L$  and applied electric fields can then be calculated as

$$N_D = \int_{E_1}^{E_2} [P(T_L) - P(T_H)] dE. \quad (4)$$

Figure 8 shows  $N_D$  as a function of  $\Delta T_{HL}$  with  $T_L=298$  K, which is the most important operating condition for PEH of low grade waste heat.  $N_D$  increases for larger  $\Delta T_{HL}$  and for the 5.6 mol% sample, almost 8 J/cm<sup>3</sup> can be achieved for  $\Delta T_{HL}=120$  K. It should be noted, that  $N_D$  was calculated with different  $\Delta E=E_2-E_1$  for the different samples, which is the main reason for the different slopes in Figure 8. In other applications, for example PEH in space, also temperature ranges far below 300 K are of interest. Therefore, we also calculated  $N_D$  over the whole temperature range that was available from our measurement data.

Table 2 shows the  $N_D$  values of our films compared to other publications together with the respective film thickness, the difference in the electric field  $\Delta E$  and the temperature change  $\Delta T_{HL}$ . As can be seen, Si:HfO<sub>2</sub> thin films enable high harvestable energy densities compared to other materials like P(VDF-TrFE). For room temperature applications, our samples are not as good as Hf<sub>0.2</sub>Zr<sub>0.8</sub>O<sub>2</sub>, which show the highest  $N_D$ , but also at higher  $\Delta T_{HL}$ . Samples with reduced Si content have a lower  $N_D$ , but  $\Delta E$  was much smaller in these cases. For the highest concentration of Si

we show here the largest  $N_D$  value ever reported for  $\Delta T_{HL}=320$  K, which is almost twice as big compared to Hf<sub>0.2</sub>Zr<sub>0.8</sub>O<sub>2</sub> [32]. This would be very favorable for PEH in very low temperature environments such as space. It should be noted however, that these values were extracted by an indirect method from the  $P$ - $E$  hysteresis curves, since direct measurements are much more difficult to perform. Nevertheless, these results show the vast potential of Si:HfO<sub>2</sub> thin films for PEH applications. In a similar argument as in Section 4.1 for the electrostatic energy storage, 3D integration of these films might be used to enhance their harvesting capabilities per projected area even further [32]. Direct integration on a chip seems like an attractive option to generate electric energy in monolithic autonomous sensor applications.

### Electrocaloric cooling

Since the ECE is the inverse of the pyroelectric effect, a look at the electrocaloric properties of these Si:HfO<sub>2</sub> films is also of interest. Based on the Maxwell relation  $(\frac{\partial P}{\partial T})_E = (\frac{\partial S}{\partial E})_T$ , a reversible adiabatic temperature change  $\Delta T$  can be calculated from measured  $P(T)$  vs.  $E$  curves, the density  $\rho$  and the specific heat capacity  $C_p$  [7]:

$$\Delta T = -\frac{1}{\rho C_p} \int_{E_1}^{E_2} T \left( \frac{\partial P}{\partial T} \right)_E dE. \quad (5)$$

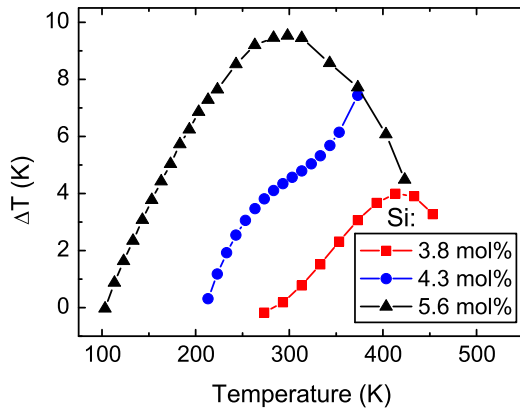


**Figure 9** Temperature change achievable through the giant electrocaloric effect in Si:HfO<sub>2</sub> thin films as a function of temperature and Si content.

This adiabatic temperature change stems from an isothermal entropy change  $\Delta S$ , which is caused by poling of a ferroelectric layer with an external electric field  $E$ :

$$\Delta S = \int_{E_1}^{E_2} \left( \frac{\partial P}{\partial T} \right)_E dE. \quad (6)$$

For calculation of  $\Delta T$ , temperature dependent specific heat capacity values were taken from ref. [44] and a density of 9.6 g/cm<sup>3</sup> was determined by X-ray reflectivity measurements. By using an inverse Olsen cycle on a MIM capacitor, this entropy change can be used in an electrocaloric cooling device. The calculated  $\Delta T$  values for different temperatures and Si concentrations are shown in Figure 9. For higher Si content, the achievable  $\Delta T$  is also higher and reaches a maximum of about 9.5 K for 5.6 mol% Si at room temperature. Lower Si content leads to a shift of the maximum  $\Delta T$  to higher temperatures corresponding to a higher phase transition temperature of the grains, which is in agreement with Figure 3. Table 3 gives an overview of the electrocaloric properties reported here in comparison to some of the best values reported in literature.

While the maximum  $\Delta T$  is not as high compared to for example PbZr<sub>0.95</sub>Ti<sub>0.05</sub>O<sub>3</sub> [7] or Pb<sub>0.8</sub>Ba<sub>0.2</sub>ZrO<sub>3</sub> [12], our films are compatible with semiconductor fabrication technology, which is important for prospective applications like on-chip cooling. Nevertheless,  $\Delta T$  values are superior to many monocrystals and bulk ceramics [5]. Examining  $\Delta T$  divided

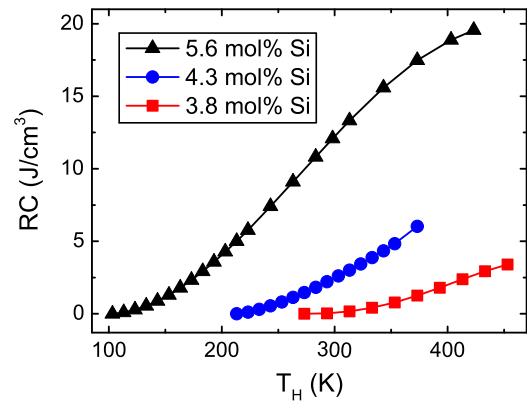


**Figure 10** Refrigerant capacity RC as a function of  $T_H$  calculated for different Si concentrations.  $T_L$  is 103, 213 and 273 K for 5.6, 4.3 and 3.8 mol% of Si, respectively.

**Table 3** Comparison of electrocaloric material properties for various thin films.

Material	$\Delta T_{max}$ [K]	at $T$ [K]	Thickness [nm]	$\Delta E$ [MV/cm]	$\Delta S_{max}$ [mJ/(K cm <sup>3</sup> )]	$\Delta T_{max}/\Delta E$ [K cm/kV]	Ref.
3.8 mol% Si:HfO <sub>2</sub>	4	413	9	1.00	29.2	0.004	This work
4.3 mol% Si:HfO <sub>2</sub>	7.4	373	9	2.33	59.3	0.003	This work
5.6 mol% Si:HfO <sub>2</sub>	9.5	298	9	3.33	85.5	0.003	This work
Hf <sub>0.2</sub> Zr <sub>0.8</sub> O <sub>2</sub>	13.4	298	9.2	3.26	96	0.004	[32]
Hf <sub>0.3</sub> Zr <sub>0.7</sub> O <sub>2</sub>	8.9	448	9.2	3.26	49	0.003	[32]
PbZr <sub>0.95</sub> Ti <sub>0.05</sub> O <sub>3</sub>	12	495	350	0.71	66	0.017	[7]
Pb <sub>0.8</sub> Ba <sub>0.2</sub> ZrO <sub>3</sub>	45.3	290	320	0.59	361	0.076	[12]

by the field difference  $\Delta E$  as a FOM, Si:HfO<sub>2</sub> shows values comparable to Hf<sub>x</sub>Zr<sub>1-x</sub>O<sub>2</sub> [32]. Another interesting FOM describing the amount of heat that can be extracted during one ideal cooling cycle is the refrigerant capacity RC [47]:

$$RC = \int_{T_L}^{T_H} \Delta S dT. \quad (7)$$

The highest RC values calculated for 3.8, 4.3 and 5.6 mol% Si:HfO<sub>2</sub> were 3.4 (at 0.9 V for  $\Delta T_{HL}=160$  K), 6.0 (at 2.1 V for  $\Delta T_{HL}=160$  K) and 19.6 J/cm<sup>3</sup> (at 3 V for  $\Delta T_{HL}=320$  K), respectively. These values are shown in Figure 10 and are considerably higher than values reported for magnetocaloric materials [47] and electrocaloric Hf<sub>x</sub>Zr<sub>1-x</sub>O<sub>2</sub> [32] which are all below 7 J/cm<sup>3</sup> and 14 J/cm<sup>3</sup>, respectively. However, it should be noted that in these studies, only smaller temperature ranges were considered. The corresponding RC values for other temperature ranges can be easily calculated as the difference of two RC values in Figure 10 at the corresponding  $T_H$  and  $T_L$ . Above room temperature, the highest value for 5.6 mol% of Si is about 8 J/cm<sup>3</sup> for  $\Delta T_{HL}=120$  K. In fact, by shifting the curves in Figure 10 in such a way that  $T_L=298$  K, one would get a very similar picture as seen in Figure 8. This shows the great potential of Si:HfO<sub>2</sub> thin films also for solid state cooling applications especially for integration on a chip, which might be used as an effective way to directly extract heat from highly integrated circuits. This could relax constraints put on circuit design because of very high areal power densities.

While the very small thickness of our films allows the use of low voltages, for an application in real devices it is necessary to scale up the film thickness without degradation of the material properties [32]. There are several different strategies that have been reported so far. The use of other dopants like Gd or Sm might be a viable option [48,49]. Gd:HfO<sub>2</sub> samples prepared by ALD showed no reduction of  $P_r$  up to thicknesses of about 30 nm [48]. Other fabrication techniques like pulsed laser deposition [49] or chemical solution deposition [50] have been shown to yield film thicknesses of up to 60 nm and 70 nm, respectively and even thicker films should be easily achievable. Therefore, choosing the right dopant and deposition method will be critical for actual applications using HfO<sub>2</sub> based ferroelectrics. Additionally, the use of thin interlayers of Al<sub>2</sub>O<sub>3</sub> was shown to enable thicker ALD films by keeping the grain size of Hf<sub>x</sub>Zr<sub>1-x</sub>O<sub>2</sub> small enough to stabilize the ferroelectric phase [51]. As already pointed out before, a smaller thickness of ferroelectric HfO<sub>2</sub> films might also be compensated by using 3D integration and thus increasing of the effective area and volume of the films per projected substrate area.

## Conclusions

The only recently discovered ferroelectric nanoscale Si:HfO<sub>2</sub> films are reported to exhibit remarkable pyroelectric and energy storage properties for a Si content between 3.8 and 5.6 mol%. We have shown that this stems from

temperature- and field-induced phase transformations between the ferroelectric orthorhombic and the paraelectric tetragonal phase. The corresponding transition temperatures can be adjusted by different Si doping concentrations over a wide temperature range. Si:HfO<sub>2</sub> also has many advantages over other prospective materials for these applications: It is a lead-free, simple binary oxide that is highly compatible with standard semiconductor manufacturing and can be easily integrated into 3D-capacitor structures to significantly enhance its properties per projected chip area.

Large ESD values of about 40 J/cm<sup>3</sup> were shown for 5.6 mol% Si:HfO<sub>2</sub> films with a very high efficiency of 80% over a wide temperature range. This might enable highly efficient on-chip supercapacitors with a small footprint. Furthermore, giant pyroelectric coefficients of up to  $-1300 \mu\text{C}/(\text{m}^2 \text{K})$  were extracted from hysteresis measurements which stem mainly from the aforementioned phase transition. The wide transition temperature range was related to the grain size distribution in the polycrystalline films, since smaller grains have a lower Curie temperature. The high pyro-coefficients combined with a relatively low permittivity lead to exceptionally high FOMs for PEH devices. Here, we calculated the to our knowledge highest value ever reported for  $k^2=0.591$ . This electrothermal coupling factor is one to two orders of magnitude higher than the best values reported so far. In contrast to recently reported Hf<sub>x</sub>Zr<sub>1-x</sub>O<sub>2</sub> films [32], giant pyroelectricity was observed at zero external fields. Additionally, harvestable energy densities  $N_D$  of up to 20.27 J/cm<sup>3</sup> per Olsen cycle surpass the best results found in literature by a factor of two. The applicability of this material in infrared detectors was shown here for the first time in principle. Electrocaloric cooling applications also benefit from these giant pyroelectric properties of Si:HfO<sub>2</sub> thin films. A maximum adiabatic temperature change  $\Delta T=9.5$  K was found for 5.6 mol% of Si at room temperature. Lower concentrations showed even better values of  $\Delta T$  normalized to the applied field with up to 0.004 K cm/V. The refrigerant capacity was calculated to be higher than the best reported values with 19.6 J/cm<sup>3</sup> per inverse Olsen cycle.

In conclusion, Si:HfO<sub>2</sub> is a unique material system for highly efficient supercapacitors, infrared detectors, giant pyroelectric energy harvesting and electrocaloric cooling. Its extraordinary properties stem from ferroelectric to paraelectric phase transitions that can be tailored to the desired application by adjusting the Si content. Furthermore, manufacturing of these films is ideally suited for monolithic on-chip integration in 3D structures with existing semiconductor process technology.

## Acknowledgments

The authors like to thank T. Boescke and G. Jaschke for capacitor processing as well as S. Piontek for SEM, D. Pohl for TEM, J. Gärtner for AFM measurements and the German Research Foundation (DFG) for funding within the Inferox project (Project no. MI 1247/11-1).



## Appendix A. Supplementary material

Supplementary data associated with this article can be found in the online version at <http://dx.doi.org/10.1016/j.nanoen.2015.10.005>.

## References

- [1] G. Sebald, E. Lefevre, D. Guyomar, *IEEE Trans. Ultrason. Ferroelectr. Freq. Control* 55 (2008) 538-551.
- [2] R.W. Whatmore, *Rep. Prog. Phys.* 49 (1986) 1335-1386.
- [3] S.B. Lang, *Phys. Today* 58 (2005) 31-36.
- [4] C.R. Bowen, J. Taylor, E. LeBoulbar, D. Zabek, A. Chauhan, R. Vaish, *Energy Environ. Sci.* 7 (2014) 3836.
- [5] M. Ožbolt, A. Kitanovski, J. Tušek, A. Poredoš, *Int. J. Refrig.* 40 (2014) 174-188.
- [6] S.P. Alpay, J. Mantese, S. Trolier-McKinstry, Q. Zhang, R. W. Whatmore, *MRS Bull.* 39 (2014) 1099-1111.
- [7] A.S. Mischenko, Q. Zhang, J.F. Scott, R.W. Whatmore, N. D. Mathur, *Science* 311 (2006) 1270-1271.
- [8] S.R. Hunter, N.V. Lavrik, S. Mostafa, S. Rajic, P.G. Datskos, *Proc. SPIE* 8377 (2012) 83770D-83771D.
- [9] M. Valant, *Prog. Mater. Sci.* 57 (2012) 980-1009.
- [10] B. Ploss, S. Bauer, *Sens. Actuators A* 25-27 (1991) 407-411.
- [11] G. Sebald, L. Seveyrat, D. Guyomar, L. Lebrun, B. Guiffard, S. Pruvost, *J. Appl. Phys.* 100 (2006) 124112.
- [12] B. Peng, H. Fan, Q. Zhang, *Adv. Funct. Mater.* 23 (2013) 2987-2992.
- [13] X. Hao, J. Zhai, *Appl. Phys. Lett.* 104 (2014) 022902.
- [14] F. Guo, B. Yang, S. Zhang, F. Wu, D. Liu, P. Hu, Y. Sun, D. Wang, W. Cao, *Appl. Phys. Lett.* 103 (2013) 182906.
- [15] G. Sebald, S. Pruvost, D. Guyomar, *Smart Mater. Struct.* 17 (2008) 015012.
- [16] Y. Tongqing, L. Peng, X. Zhuo, Z. Liangying, Y. Xi, *Ferroelectrics* 230 (1999) 181-186.
- [17] P.D. Thacher, *J. Appl. Phys.* 39 (1968) 1996-2002.
- [18] A. Navid, L. Pilon, *Smart Mater. Struct.* 20 (2011) 025012.
- [19] B. Ma, D.-K. Kwon, M. Narayanan, U. Balachandran, *J. Mater. Res.* 24 (2009) 2993-2996.
- [20] J. Li, S. Tan, S. Ding, H. Li, L. Yang, Z. Zhang, *J. Mater. Chem.* 22 (2012) 23468.
- [21] T.S. Börscke, J. Müller, D. Bräuhäus, U. Schröder, U. Böttger, *Appl. Phys. Lett.* 99 (2011) 102903.
- [22] U. Schroeder, E. Yurchuk, J. Müller, D. Martin, T. Schenk, P. Polakowski, C. Adelman, M.I. Popovici, S.V. Kalinin, T. Mikolajick, *Jpn. J. Appl. Phys.* 53 (2014) 08LE02.
- [23] J. Müller, T.S. Börscke, U. Schröder, S. Mueller, D. Bräuhäus, U. Böttger, L. Frey, T. Mikolajick, *Nano Lett.* 12 (2012) 4318-4323.
- [24] X. Sang, E.D. Grimley, T. Schenk, U. Schroeder, J.M. LeBeau, *Appl. Phys. Lett.* 106 (2015) 162905.
- [25] S.E. Reyes-Lillo, K.F. Garrity, K.M. Rabe, *Phys. Rev. B* 90 (2014) 140103.
- [26] S. Mueller, J. Müller, U. Schroeder, T. Mikolajick, *IEEE Trans. Device Mater. Reliab.* 13 (2013) 93-97.
- [27] J. Müller, E. Yurchuk, T. Schlösser, J. Paul, R. Hoffmann, S. Müller, D. Martin, S. Slesazek, P. Polakowski, J. Sundqvist, M. Czernohorsky, K. Seidel, P. Kücher, R. Boschke, M. Trentzsch, K. Gebauer, U. Schröder, T. Mikolajick, *Symposium on VLSI Technology*, June 2012, 25-26.
- [28] P. Polakowski, S. Riedel, W. Weinreich, M. Rudolf, J. Sundqvist, K. Seidel, J. Müller, *IEEE 6th International Memory Workshop*, May 2014, 1-4.
- [29] S. Mueller, S.R. Summerfelt, J. Müller, U. Schroeder, T. Mikolajick, *IEEE Electron Device Lett.* 33 (2012) 1300-1302.
- [30] M.H. Lee, Y.-T. Wei, K.-Y. Chu, J.-J. Huang, C.-W. Chen, C.-C. Cheng, M.-J. Chen, H.-Y. Lee, Y.-S. Chen, L.-H. Lee, M.-J. Tsai, *IEEE Electron Device Lett.* 36 (2015) 294-296.
- [31] M.H. Park, H.J. Kim, Y.J. Kim, T. Moon, K.D. Kim, C.S. Hwang, *Adv. Energy Mater.* (2014) 1400610.
- [32] M.H. Park, H.J. Kim, Y.J. Kim, T. Moon, K.D. Kim, C.S. Hwang, *Nano Energy* 12 (2015) 131-140.
- [33] J. Grindlay, *An Introduction to the Phenomenological Theory of Ferroelectricity*, Pergamon Press Ltd, Oxford, 1970.
- [34] A.S. Bhalla, R.E. Newnham, *Phys. Status Solidi A* 58 (1980) K19-K24.
- [35] R.N. Patil, E.C. Subbarao, *J. Appl. Cryst.* 2 (1969) 281-288.
- [36] J.Y. Li, *Mech. Mater.* 36 (2004) 949-958.
- [37] M.D. Glinchuk, P.I. Bykov, arXiv:cond-mat/0406032 [cond-mat.mtrl-sci], 2004.
- [38] R. Materlik, C. Künneth, A. Kersch, *J. Appl. Phys.* 117 (2015) 134109.
- [39] K. Keizer, A.J. Burggraaf, *Phys. Status Solidi A* 26 (1974) 561-569.
- [40] T.S. Börscke, St Teichert, D. Bräuhäus, J. Müller, U. Schröder, U. Böttger, T. Mikolajick, *Appl. Phys. Lett.* 99 (2011) 112904.
- [41] P. Banerjee, I. Perez, L. Henn-Lecordier, S.B. Lee, G. W. Rubloff, *Nat. Nanotechnol.* 4 (2009) 292-296.
- [42] D. Zhou, J. Müller, J. Xu, S. Knebel, D. Bräuhäus, U. Schröder, *Appl. Phys. Lett.* 100 (2012) 082905.
- [43] W. Zhou, Q. Shi, B.F. Woodfield, A. Navrotsky, *J. Chem. Thermodynamics* 43 (2011) 970-973.
- [44] I.M. McKinley, L. Pilon, *Appl. Phys. Lett.* 102 (2013) 023906.
- [45] G. Vats, H.S. Kushwaha, R. Vaish, *Mater Res, Express* 1 (2014) 015503.
- [46] K.A. Gschneider Jr, V.K. Pecharsky, A.O. Tsokol, *Rep. Prog. Phys.* 68 (2005) 1479-1539.
- [47] M. Hoffmann, U. Schroeder, T. Schenk, T. Shimizu, H. Funakubo, O. Sakata, D. Pohl, M. Drescher, C. Adelman, R. Materlik, A. Kersch, T. Mikolajick, *J. Appl. Phys.* 118 (2015) 072006.
- [48] Y. Sharma, D. Barrionuevo, R. Agarwal, S.P. Pavunny, R. S. Katiyar, *ECS Solid State Lett.* 4 (2015) N13-N16.
- [49] S. Starschich, D. Griesche, T. Schneller, R. Waser, U. Böttger, *Appl. Phys. Lett.* 104 (2014) 202903.
- [50] H.J. Kim, M.H. Park, Y.J. Kim, Y.H. Lee, W. Jeon, T. Gwon, T. Moon, K.D. Kim, C.S. Hwang, *Appl. Phys. Lett.* 105 (2014) 192903.



**Michael Hoffmann** received his B.Sc. degree in Electrical Engineering and Information Technology from the Otto-von-Guericke-University Magdeburg in 2013. He is currently pursuing a M.Sc. degree in Microelectronics at Technische Universität Dresden in collaboration with NaMLab gGmbH. His current research interests include ferroelectric HfO<sub>2</sub> and ZrO<sub>2</sub> based thin films for low power computing, sensors and energy applications as well as the reliability of high-k dielectrics in advanced nanoelectronic devices.



**Uwe Schroeder** received his doctoral degree at University of Bonn, Germany including a research visit at UC Berkeley and worked at University of Chicago as a post-doctoral researcher. He joined Infineon formerly Siemens Semiconductor in 1997 for capacitor development in the DRAM Development Alliance with IBM, before transferring to Infineon's Memory Development Center in Dresden, Germany in 2000. There,

he continued the research on high-k dielectrics and their integration into DRAM capacitors. During this time the ferroelectric properties of HfO<sub>2</sub> based dielectrics were found. In 2009 he moved to NaMLab and pursued his work on high-k dielectrics and ferroelectric HfO<sub>2</sub>-layers.



**Christopher Künneth** is a doctoral candidate at the Technical University of Munich and Munich University of Applied Sciences. He received his M.Sc. in Micro- and Nanotechnology from the Munich University of Applied Sciences in 2014. His current research includes the ferroelectric and pyroelectric behavior of  $\text{HfO}_2$  and  $\text{ZrO}_2$  based thin films for memory devices, electric sensors, energy harvesting and cooling applications.



**Alfred Kersch** received the Ph.D. degree in theoretical physics from the University of Mainz, Mainz, Germany, in 1990. He then joined the Corporate Research of Siemens AG, the Memory Product Division of Infineon AG in 1999, and the Product Division of Qimonda AG in 2006. Since 2009, he has been with the Munich University of Applied Sciences, Munich, Germany. His research interests involve modeling and simulation

of microstructures and nanostructures, the methods of fabrication, and the ab initio calculation of high- $\kappa$  dielectric properties.



**Sergej Starschich** received the M.Sc. degree in electrical engineering from Rheinisch-Westfälische Technische Hochschule Aachen University, Aachen, Germany, in 2012. He is currently working on his Ph.D. at the RWTH Aachen University, investigating the properties of hafnium oxide based ferroelectrics.



**Ulrich Böttger** received his diploma degree in physics in 1988 and the Dr.-Ing. degree in 1994, both from the Rheinisch-Westfälische Hochschule (RWTH) Aachen. After 4 years as project manager of SMEs he joined RWTH Aachen again working in the field of "ferroelectric and dielectric thin films and devices" at the Institute of Electroceramic Materials (IWE 2). He is author and co-author of more than 100 scientific papers.



**Thomas Mikolajick** received the Diploma and his Ph.D. in electrical engineering from the University Erlangen-Nuremberg in 1990 and 1996. From 1996 till 2006 he was in various positions in the semiconductor industry. In late 2006 he moved to the University of Technology Freiberg. In October 2009 he started at Technische Universität Dresden where he holds a professorship for nanoelectronic materials together with

the position of scientific director at NaMLab gGmbH. Prof. Mikolajick's research interest is in materials for semiconductor devices. He is author or co-author of about 230 scientific publications and inventor or co-inventor of about 50 patents.